UNIVERSITEIT VAN PRETORIA
UNIVERSITY OF PRETORIA
YUNIBESITHI YA PRETORIA

Partial Roasting of a PGM Concentrate

by

RI Rambiyana

A dissertation submitted in partial fulfilment
of the requirements for the degree of
MEng Metallurgy

SCHOOL OF ENGINEERING

Department of Materials Science and Metallurgical Engineering

University of Pretoria

2014

Abstract

PGM concentrates contain more than just the platinum group minerals. They also concentrate three minerals—pyrrhotite ($Fe_{1-x}S$), pentlandite ($[Fe,Ni]_9S_8$) and chalcopyrite ($CuFeS_2$). In a sample of Merensky concentrate tested in this study, these minerals account for half the concentrate. During smelting and converting these sulphides collect the PGMs in matte. Smelting produces a matte, the composition of which converting adjusts by oxidizing sulphur to SO_2 and iron to Fe_2SiO_4 (fayalite). The objective of roasting a PGM concentrate would be to alter the composition of a concentrate, at lower temperatures in a kiln *before* smelting, so that the matte formed contains less iron and sulphur, but, still, collects all of the PGMs, copper and nickel.

Roasting tests were conducted in a bench-scale rotary kiln on a sample of Merensky concentrate supplied by Lonmin. The kiln was purged with air to maintain high oxygen partial pressures (~0.21 atm O_2). Test temperatures from 350 °C to 700 °C and residence times from 2 to 30 minutes were explored. The roasted products were smelted in argon at 1500 °C to assess the effect of roasting on matte fall and the deportment of base metals.

Roasting for 20 minutes at 550 and 650 °C reduced the sulphur content in the concentrate by 60 and 70 %, respectively—from 17.4% to ~5% sulphur. Iron was oxidized to an iron oxide. Fe_3O_4 (magnetite) predominated at lower temperatures (<500 °C); Fe_2O_3 (hematite) predominates at higher temperatures. Oxidation in each of these minerals occurred through a number of reactions. Some rates were faster than others. Under the conditions tested *all* of the iron in pyrrhotite oxidized to iron oxides, and *most* of the iron in chalcopyrite and pentlandite were oxidized. Copper and nickel remained as sulphides. The smelting of roasted products produced a lower matte fall, the iron in matte was less than 3 %, and matte collected all of the copper, but not all of the nickel. Nickel also partitioned to the slag, where it reported to the spinel phases. The matte formed (from concentrate roasted at 550 °C) in a number of discrete prills (rather than collecting in a single "button"), which might have been a consequence of high slag viscosities. For concentrate roasted at 650 °C discrete alloy prills and not matte prills were formed.

Contents

List of tables

List of figures

Acknowledgment

I owe a debt of gratitude to a number of individuals. Without their help this work would have been a heavier burden. First, my supervisor, Professor Andrie Garbers-Craig, Head of the Center for Pyrometallurgy in the Department of Materials Science and Metallurgical Engineering. I thank her for the invaluable discussions we had, for directions she gave the project, and for her diligent and careful comments on drafts of this dissertation. I should like also to thank other members of staff in the department: Professor Johan de Villiers, Dr Robert Cromarty, Dr Johan Zietsman and Markus Erwee for numerous discussions over the months. Professor De Villiers in particular helped me interpret complex patterns in X-ray diffractometry. Fellow students at the Centre for Pyrometallurgy gave moral support, which saw me through difficult times.

A good part of this work was undertaken at Anglo American's research laboratories—now Technical Solutions, Research—at Crown Mines. I am indebted to a number of colleagues there:

- To Paul den Hoed for the many hours spent in discussion probing the problem, constructing arguments, and developing clear lines of thinking.
- To Sakkie Vlok, he took me through my paces, teaching me to be innovative in the laboratory, to work with care and develop skills in the art of experimentation.
- To three mineralogists— Vulani Mafada, Byron Bezuidenhout and Darren Tiddy—for their help with SEM-EDS.
- To Dr Robert Schouwstra, Head of Mineral & Process Research, for letting me use the facilities at Technical Solutions, Research.
- I gratefully acknowledge the support of Dr Lloyd Nelson and Rodney Hundermark (Anglo American Platinum) and Rian Bezuidenhout (formerly at Lonmin).

Finally my thanks go to: my family, for their unconditional support throughout this work; to my fiancée, Bernice, for the love, support, encouragement and patience she extended throughout this work; and to my heavenly father, for provision and the grace of life.

Chapter 1
Context and Aims

1.1 Background

The Bushveld Complex, a large layered igneous intrusion, underlies an area of about 66,000 km^2 on the Highveld of South Africa (Cawthorn and Webb, 2001). It contains over 80 % of the world's platinum group metals (PGMs), the largest reserves of platinum in the world[1]. PGMs are currently exploited in three tapered strata known as the Merensky Reef, Upper Ground 2 (or UG2) and the Platreef.

These strata are mined. The ore is beneficiated (by milling and flotation) to produce concentrates. The precious metals in these concentrates are predominately associated with base metal and iron sulphides (Cabri, 1989). The predominant base metal sulphides are pentlandite ($[Fe,Ni]_9S_8$) and chalcopyrite ($CuFeS_2$); the iron sulphides are pyrite (FeS_2) and pyrrhotite (FeS). The latter is the most abundant sulphide in Merensky concentrates; the former is the least abundant (Brynard *et al*, 1976). If one includes iron sulphides in the category of base metal sulphides (abbreviated as BMS), then the Merensky reef contains typically up to 3% base metal sulphides comprising 45% pyrrhotite, 32% pentlandite, 16% chalcopyrite and 2–4% pyrite (Jones, 1999). In a Merensky ore the majority of PGMs are associated with pentlandite (Jones, 1999). PGMs are also associated with other base metal sulphides or occur in other minerals such as cooperite (PtS), laurite ($[Ru,Os,Ir]S_2$), braggite ([Pt,Pd,Ni]S), or, in some cases, ferroplatinum (Pt_xFe_{1-x}). Such associations occur, however, to a lesser degree (Jones, 1999 and Liddell *et al*. 1986). Pyroxene such as bronzite ($[Mg,Fe,Ca]SiO_3$) and diopside ($CaMgSi_2O_6$), feldspar, plagioclase ($[Na,Ca]Al_{1\text{-}2}Si_{3\text{-}2}O_8$) and biotite ($K[Mg,Fe]_3[AlSi_3O_{10}][OH]_2$) constitute the major gangue minerals in Merensky ores (Jones, 1999).

---

[1] Unless indicated otherwise, PGM refers to platinum group metals, although some mineralogists reserve the term for platinum group minerals, using the abbreviation PGE (platinum group elements) to refer to the metals in their elemental state.

The main constituents of ore from the UG2 seam are chromite ($FeCr_2O_4$), orthopyroxene ($[Mg,Fe,Ca][Mg,Fe,Al][Si,Al]_2O_6$), plagioclase($[Na,Ca][Al,Si]_4O_8$), talc ($[Mg_3Si_4O_{10}[OH]_2$) in small amounts, chlorite ($[Mg_3,Fe_2]Al[AlSi_3]O_{10}[OH]_8$) and phlogopite ($K_2[Mg,Fe]_6[Si_6Al_2O_2][OH,F]$), iron and base metal sulphides and platinum-group minerals. The chromitite content of the ore is between 60% and 90%. Pentlandite, chalcopyrite, pyrrhotite, pyrite and, to a lesser extent, millerite (NiS) are the predominant base metal sulphides (Jones, 1999 and Liddell *et al*. 1986).

Other differences set UG2 ore apart from Merensky ore. The former contains much less nickel and copper. It has high levels of Cr_2O_3 (about 30% compared with 0.1%) and is therefore more refractory (Nell, 2004). The sulphide particles in UG2 ore are usually finer than those in Merensky ore (Jones, 1999).

Platreef concentrates are similar to Merensky concentrates in chemical and mineral composition (Nell, 2004). It is slightly enriched in palladium, however.

The four main producers of PGMs in South Africa are Anglo American Platinum (formerly Anglo Platinum or Amplats), Impala Platinum, Lonmin Platinum and Northam Platinum ((Jones, 1999). Beneficiation involves comminution, gravity separation, and flotation to produce a concentrate enriched in sufides and PGMs.

The processing of PGM concentrates takes the form of conventional direct smelting, converting and refining. Dried concentrate from beneficiation is the feed to the smelter (Figure 1). Rectangular six-in-line, submerged-arc furnaces or circular three-electrode furnaces are typical in the industry. The furnace typically operates at 1350°C for Merensky concentrate and as high as 1650°C for UG2 concentrate (Jones 1999). The objective of smelting is to separate gangue minerals (the oxides and silicates) from the sulphide minerals, which comprise the base and precious metals. In the smelter two liquid phases of distinct relative densities form as the concentrate melts: a lighter fayalitic-fosteritic ($[Mg,Fe]_2SiO_4$) slag and a denser matte rich in nickel copper sulphides, which contains other base metals and the precious metals (Liddell *et al*. 1986).

Matte from the smelter is transferred to a converter vessel. The Peirce-Smith converter is the most commonly used vessel. Anglo American Platinum developed the Anglo Converting Process (ACP), a flash smelting process that is based on Ausmelt technology. Silica (SiO_2) is added to the converter to flux the iron oxide formed by the oxidation of iron during the blowing process (Hundermark *et al.* 2011). The slag is fayalitic (Fe_2SiO_4) in composition. The blowing process reduces the level of iron in the matte to 3% or less.

The converter matte is treated in the base metal refinery (BMR) to recover nickel, copper and cobalt. The leach liquor from the BMR is processed at the precious metal refinery (PMR) to recover the platinum group elements.

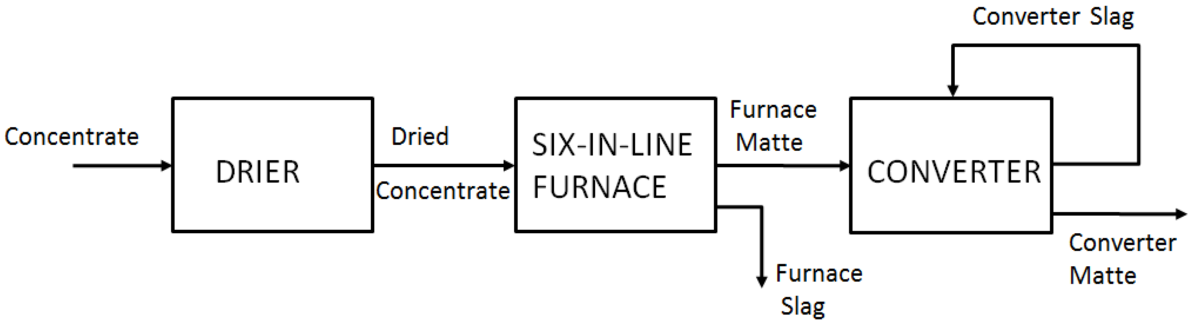

Figure 1. Schematic flow sheet of a typical platinum smelter-converter plant (Jones, 1999).

Associated with the treatment of base metal sulphides in these concentrates are two adverse consequences. First, free sulphur and SO_2 produced in smelting are implicated in the corrosion of the copper coolers. Thethwayo (2010), in studies on the sulfidation of copper coolers in PGM smelters, observed that gaseous sulphur attacks copper and forms CuS (covellite). Secondly, smelting and converting inevitably emit, to a greater or lesser degree, fugitive SO_2, which if not captured is released into the environment.

In an attempt to mitigate these inherent liabilities of conventional smelting, several new flow sheets have been proposed and tested. Each of them are discussed in turn.

1.1.1 ConRoast

The ConRoast process was developed by Mintek to treat nickel-copper and PGM concentrates (Figure 2) (Jones, 2002). In the conventional matte-smelting process there is a strict limit on the chromium content in the feed, because of the deleterious build-up of stable crystalline chromium-rich spinels in the furnace (Jones and Geldenhuys, 2011). The ConRoast process eliminates potential problems associated with high levels of chromium in smelting, and thus offers the possibility of smelting ores with higher chromium content (Jones, 2002; Eccleson and White, 2009). In this process concentrate is dead-roasted to remove most of the sulphur in the concentrate. The dead-roasted concentrate is then smelted in a DC-arc (direct current) furnace (Jones and Geldenhuys, 2011). An iron-based alloy acts as a collector for nickel, copper and PGMs (Jones, 2002). The sulphur removed during roasting is of suitable quality for the production of sulphuric acid in an acid plant (Jones and Geldenhuys, 2011).

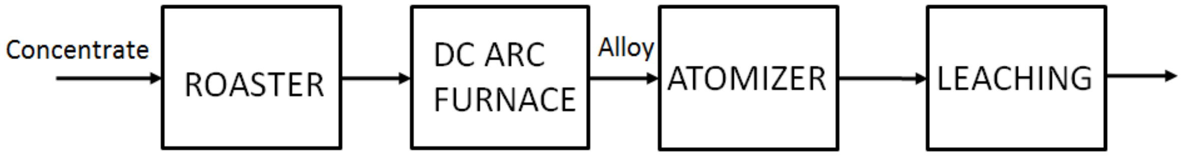

Figure 2: Schematic flow sheet for the ConRoast process (Jones and Geldenhuys, 2011).

1.1.2 Reduction-roast-smelting

In reduction-roast-smelting partially roasted concentrate or a blend of dead-roasted and green concentrate is fed into a reduction smelter (Diaz *et al*. 1994a). The aim is to have a feed to the furnace containing enough sulphur to trap most of the base metals as sulphides and leave the iron in a metallic form (Diaz *et al*. 1994b). Thus smelting and converting are done with minimal sulphur evolution.

The advantages of roast reduction smelting are that (1) sulphur is discharged as a continuous stream of SO_2 strong enough to produce sulphuric acid in an acid plant, (2) sulphur emissions in the smelter is substantially lower, and (3) produces furnace matte grades that are higher than those in reverberatory smelting and conventional electro-smelting, this means less molten material is transferred in ladles across the converter aisle (Diaz *et al*. 1994a).

ConRoast and roast reduction smelting are two attempts at addressing liabilities in conventional smelting. This current study looks at the possibility of yet another modification to the current smelting flow sheets, the addition of a partial roasting stage prior to smelting.

1.1.3 Partial roasting

Two companies currently partially roast nickel concentrates before smelting. Vale Inco runs a smelter at Thompson, Manitoba, and Xstrata Nickel has a smelter in Sudbury, Ontario (Pandher, 2010). About 40 % of sulphur is removed from the concentrate at Thompson, and as much as 70 % of sulphur is removed at Sudbury (*ibid*.). Both plants run fluidized-bed roasters.

1.2 Context and aims of this study

This study focused on the possibility of partially roasting PGM concentrates prior to smelting. The objectives of the partial roast were to desulphurize the concentrate through sulphur oxidation and to oxidise the iron associated with the base metal sulphides. This will lower the sulphur content of melting furnace feed, which will result in lower emissions of sulphur and SO_2 during smelting and may reduce corrosion of the copper coolers. The oxidation of iron is expected to result in lower matte falls during smelting and, as a consequence of the lower matte falls, there should be a reduction in the level of blowing required to lower the iron content during converting. A roasting stage also serves to dry and heat up the concentrate, an addition that will lower the energy requirements of smelting.

Although its name refers to *platinum group* minerals or elements, a PGM concentrate is a collection of sulphides of iron and two base metals, copper and nickel (Chapter 2). This study investigated the roasting of these sulphides. The minerals that define them fall into two systems, Cu-Fe-S-O and Ni-Cu-S-O. Iron sulphides fall within both systems. The chemical thermodynamics of these systems—the subject of Chapter 3—identify the stable phases in each system and the conditions that make them stable. The chemical thermodynamics are described with the aid of predominance (or Kellogg) diagrams and phase diagrams. Studies into the chemical kinetics of roasting, noting similarities and differences between phases that occur at equilibrium (chemical thermodynamics) and phases observed in bench-scale tests are reviewed in Chapter 4. In roasting, a high oxygen partial pressure that drives the oxidation of iron and base metal sulphides is imposed. Reactor configurations and experimental procedures are described in Chapter 5. Two aspects of reaction kinetics—mechanisms of roasting, and extents of reaction are covered in Chapter 6 and Chapter 7 respectfully. Chapter 7 also describes smelting tests conducted on roasted concentrates. These tests help quantify the success of roasting.

Chapter 2
Samples and sub-samples

The sample used in this study was a Merensky concentrate—a product of flotation—derived from a mine exploiting the Merensky reef in Limpopo Province, South Africa. It is the feed to the furnaces for smelting. This chapter describes the physical characteristics and chemical and mineral compositions of the sample. The physical characteristics have a bearing on sampling and rate of reactions, whereas the mineral composition has important consequences for our understanding of how the concentrate behaves during roasting.

2.1 Physical properties

Particle size

The particle-size distribution (PSD) of the concentrate was measured by laser diffraction (in a Malvern Mastersizer 2000) and image analysis (in a Mineral Liberation Analyser, or MLA, which measures the dimensions of particles exposed in section). The concentrate from flotation contained agglomerated particles. The PSDs by laser diffraction of the unscreened concentrate (the sample of the concentrate as supplied) and the screened concentrate (the product of screening at 106 µm), along with the PSD of the screened concentrate by image analysis, are recorded in Figure 3**Error! Reference source not found.**. The reason for screening was to remove agglomerates. In the process of removing agglomerates, fines were also generated—indicated by a higher fines fraction in the screened material (Figure 3**Error! eference source not found.**). The particles are fine: for the screened material the d_{50} is 19 µm, the d_{90} is 82 µm (Table 1). The PSD of the screened sample is comparatively broad: $d_{10\text{-}90}$ is 79 µm, being four times the d_{50}. Image analysis tends to underestimate the fraction of particles finer than 10 µm (the beam simply does not detect very fine particles). Thus the PSDs by the two techniques differ at finer particles sizes, but overlap at coarser sizes (>30 µm).

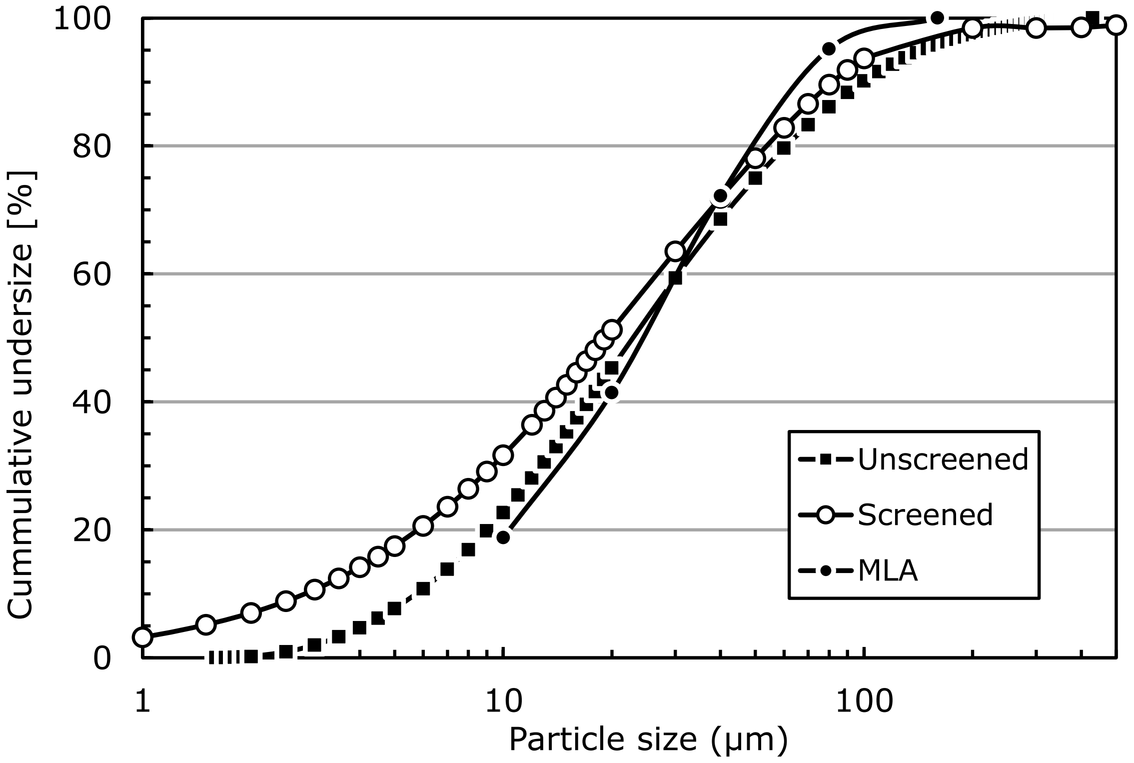

Figure 3: Particle-size distribution of the unscreened and screened (Malvern Mastersizer 2000), and screened MLA samples.

Table 1: Sample properties

	Laser diffraction		Image Analysis
Property	Unscreened	Screened	Screened
	Particle size [µm]		
d_{10}	6	3	–
d_{50}	23	19	26
d_{90}	99	82	71
$d_{10\text{-}90}$	93	79	66
Sauter mean diameter	14	6	16
	Density [g/cm^3]		
Bulk	0.97	1.54	
Absolute	3.6	3.6	3.6
Void fraction, Φ [–]	0.73	0.56	–
Surface area [m^2/g]	0.43	0.97	–

Formulae for the void fraction calculation:

$\phi = 1 - \frac{\rho_{\text{bulk}}}{\rho_{\text{absolute}}}$. Surface area measured by laser diffraction

Associated with fine particle sizes is a high void fraction of the bed (Table 1). Even with tapping, the void fraction does not decrease significantly. The reason for the high void fraction is the greater influence of the inter-particle (Van der Waals) forces between particles compared with gravitational forces acting on particles (Knowlton 2002). Inter-particle forces cause finer particles to cluster rather than fill the voids between coarser particles. The irregular shape of the particles, along with low sphericity (shape factor), could exacerbate the effect (Figure 4 andFigure 5). The significance of the high void fraction—an extensive network of pores— becomes apparent in a subsequent chapter.

2.2 Mineral composition

The concentrate comprises a number of minerals that fall into two groups (Table 2). The first group contains the sulphide minerals. These include two base metals sulphides, pentlandite ($[Ni,Fe]_9S_8$) and chalcopyrite ($CuFeS_2$), and two iron sulphides, pyrrhotite ($Fe_{1-x}S$) and pyrite (FeS_2). The other group contains minerals that are classified as gangue minerals which do not contain sulphur and are unlikely to take part in roasting. X-ray diffractometry (XRD) and scanning electron microscopy using energy dispersive spectroscopy (SEM-EDS) confirmed the presence of these mineral phases (Table A1 Appendix A, Figure 4 and Figure 5). Pyrrhotite (22.9%) is the most abundant, comprising almost a quarter of the sample. Pentlandite and chalcopyrite, between them, make up over a quarter of the sample. Taken together, these sulphides account for half the mass of the sample. All metal sulphides have similar particle size distributions (measured by MLA image analysis—2 dimensional section through the sample.)—and are above 85% cumulative to undersize at 80 µm (Figure 6). The base metal sulphides in the concentrate are at least 80 % liberated (Table A2 Appendix A). Therefore oxygen access to these particles is unlikely to be hampered. In an event where particles have preferred oxidation directions, these directions too are exposed to oxygen.

Table 2: Mineralogical analyses of Merensky concentrate as determined by MLA (bulk modal analysis).

Mineral	Weight %
BMS	
Pyrrhotite ($Fe_{1-x}S$)	22.9
Pentlandite ($[Ni,Fe]_9S_8$)	16.0
Chalcopyrite ($CuFeS_2$)	11.2
Pyrite (FeS_2)	2.0
Other Sulphides	0.2
Bornite (Cu_5FeS_4)	0.1
Gangue	
Enstatite ($Mg_2Si_2O_6$)	30.6
Other	16.9

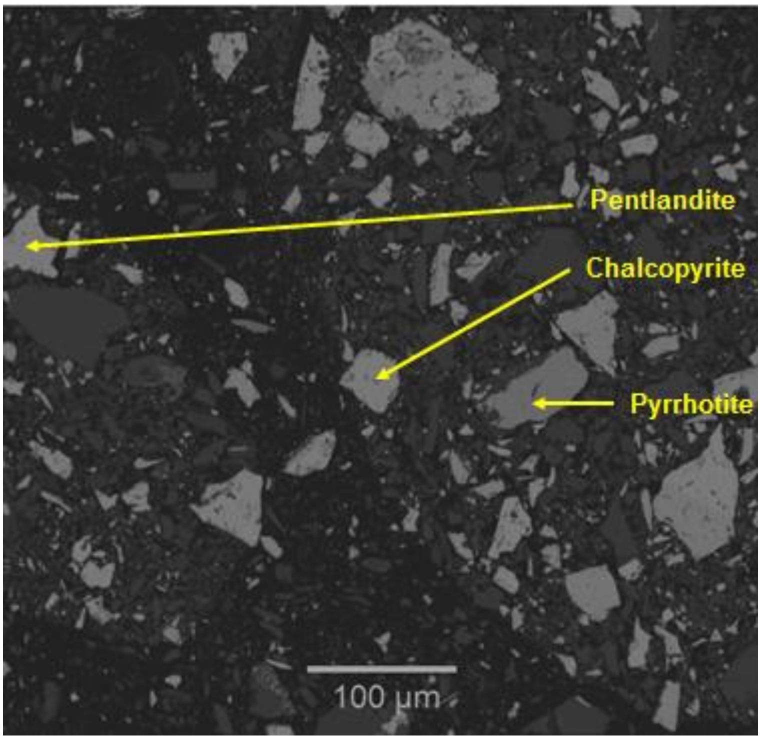

Figure 4: Backscattered electron image of a section through the sample: BMS.

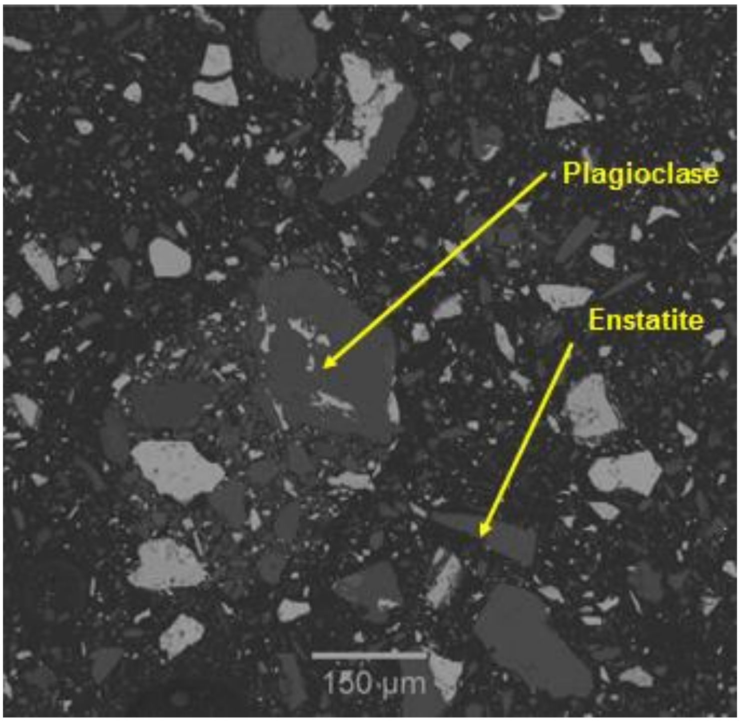

Figure 5: Backscattered electron image of a section through the sample: gangue.

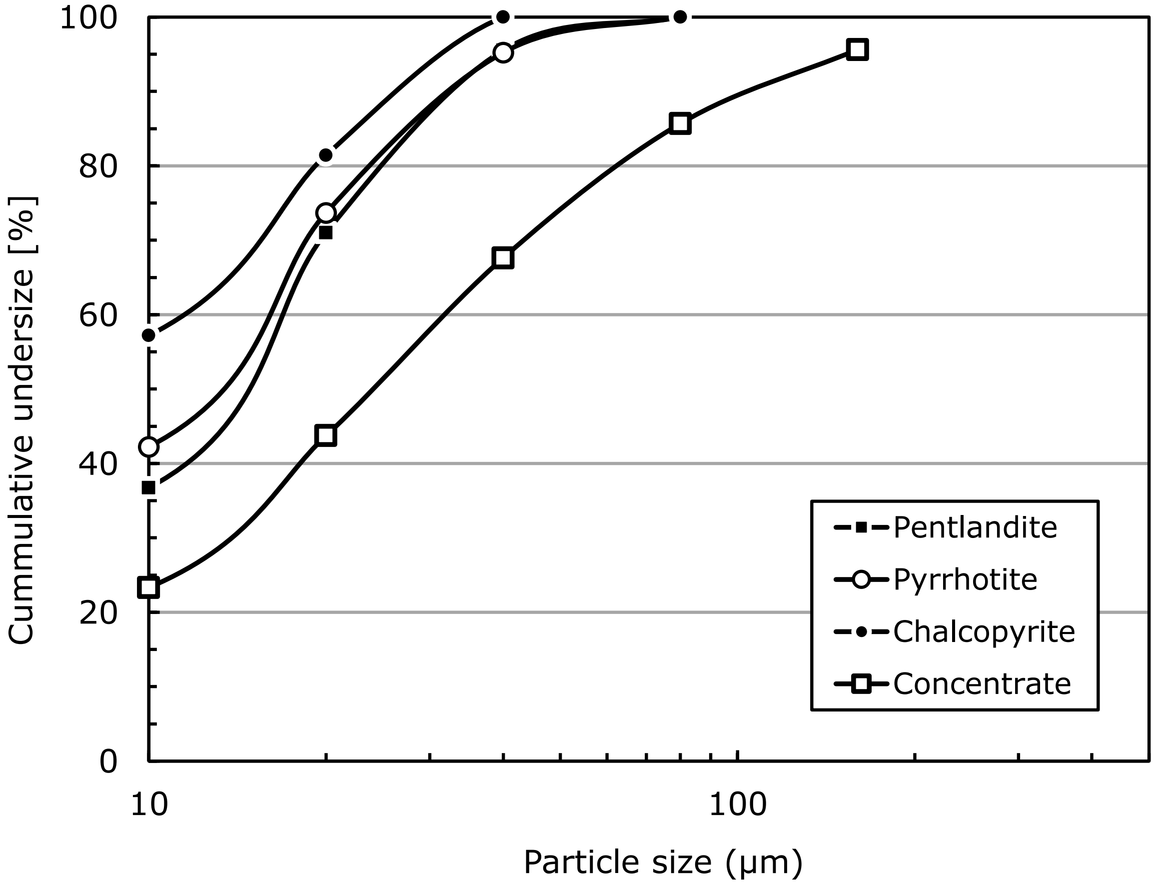

Figure 6: Particle size distributions of iron and base metal sulphides and concentrate

2.3 Consequences for the study

The physical properties of the concentrate have consequences that relate to sampling, reactor configuration and kinetics. First, sampling: Since the particles are fine, the sample is well mixed and unlikely to un-mix during sampling. The uncertainty in the representativeness of a grab sample will be acceptably low (< 5 %) for the very fine particles in the Merensky concentrate tested (Allen, 1990).

Secondly, the consequence for reactor configuration: Static particles occupy a bed. The void fraction of a bed of the concentrate is high (Table 1). The voids form a network of torturous pores that connect the inner voids to the free surface of the bed. Oxygen has to diffuse from the free board through these pores to the surface of sulphide minerals in the inner voids. Similarly SO_2 produced in roasting has to diffuse through these pores to the free surface. The large void fraction provides a gaseous volume that permits reaction, but one that is not so large as to allow the reaction to proceed to completion. Furthermore, the diffusion paths are long—a fixed bed can be several centimetres deep—which will hinder the rapid exchange of gases between the gaseous freeboard and inner voids of the bed. The diffusion of the gaseous species (O_2 and SO_2) through these torturous pores is likely to be rate limiting. A fixed bed, therefore, is an unsuitable reactor configuration for roasting

A fluidized bed is also an unsuitable configuration for roasting PGM concentrates. A bed of concentrate particles, according to Geldart's classification, fall into group C (Figure 7).[2] Particles in this group are cohesive in that the inter-particle forces are greater than the gravitational forces acting on particles. As a consequence particles are attracted to each other and clump together (Knowlton, 2002). The bed of particles does not fluidize well. Thus, although normally providing good solid-gas contact (for particles in group A and B), a fluidized bed does not provide the desirable conditions (good mixing) needed for roasting fine particles in PGM concentrates. A fluidized bed was discounted from the experimental programme. This leaves either a rotary kiln or an angular reciprocating reactor for tests in which particles are exposed to fresh oxygen and free from an inhibiting build-up of SO_2.

---

[2] The screened sample is finer than 106 µm. For purposes of comparison, an ilmenite concentrate and beach sand, both typically found on the north-east coast of KwaZulu-Natal Province, have been plotted. The iron ore fines were collected from Sishen Mine (Kumba Iron Ore—Den Hoed, pers. comm.)

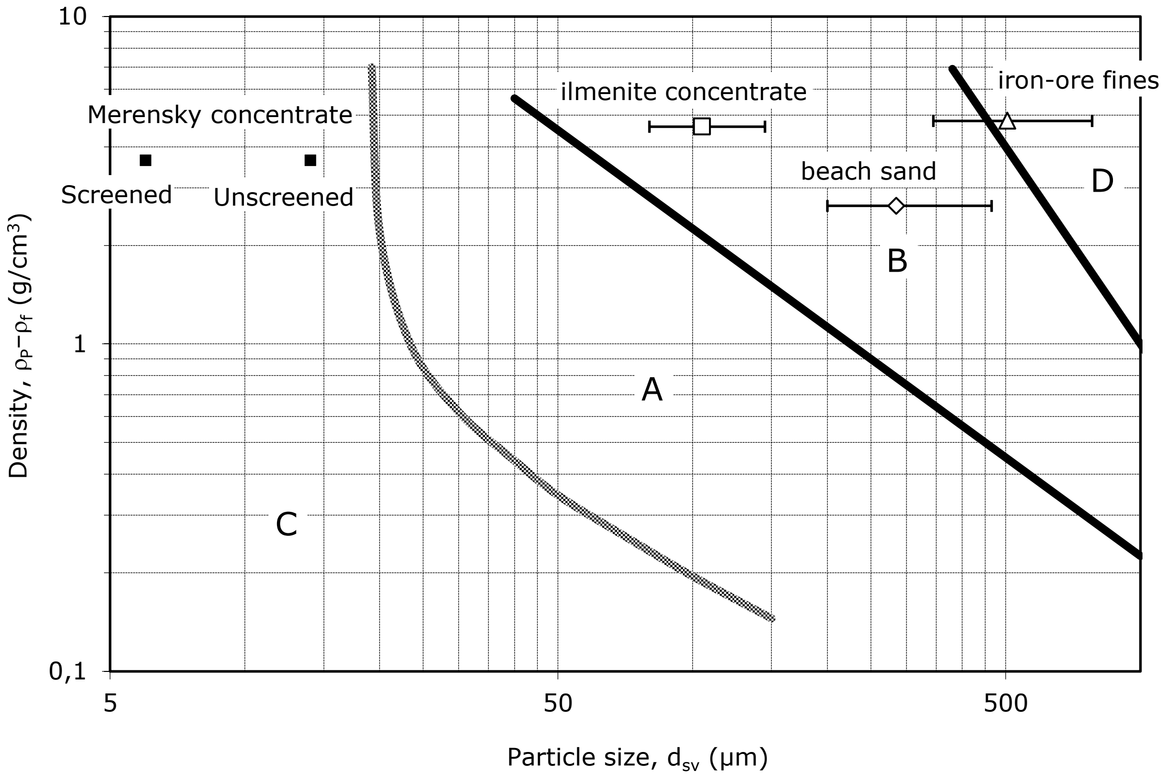

Figure 7: The sample (a bed of Merensky concentrate) plotted in Geldart's classification (d_{sv} = surface-volume, or Sauter mean, diameter).

A third consequence of particle size relates to reaction kinetics: Finer particles expose a larger surface area; therefore reaction rates are faster and solid-state diffusion distances are shorter. This may have consequences for the types of phases that are formed.

The mineral composition, incidentally, structures the way this study was conducted. It does so in the following manner; sulphur in the concentrate is associated with base metal sulphides. These minerals, therefore, are the ones of interest in sulphur removal. Furthermore, nickel resides in a mineral distinct from the one that contains copper. Iron, on the other hand, is associated with all three sulfide minerals, namely pyrrhotite ($Fe_{1-x}S$), chalcopyrite ($CuFeS_2$) and pentlandite ($[Ni,Fe]_9S_8$). Thus, although this is a PGM concentrate the problem of roasting is really one of the behaviour of specifically the iron-containing base metal sulphides during oxidation.

Chapter 3

Chemical thermodynamics – A review of the literature

The previous chapter concluded that PGM concentrates mainly contain three sulphur-bearing minerals, namely, pyrrhotite, pentlandite and chalcopyrite. These minerals are implicated in roasting. The minerals and their oxidation products can be represented in a three- or four-component system (pyrrhotite—Fe-S-O, pentlandite—Ni-Fe-S-O and chalcopyrite—Cu-Fe-S-O). These systems are depicted in predominance or Kellogg diagrams and in phase diagrams. Both types of diagrams provide a frame of reference in understanding reactions in the oxidation of iron and base metal sulphides. In as much as they can be used to describe reactions, they do so under conditions that are infinitesimally removed from equilibrium. Predominance diagrams show phase relations as a function of oxygen partial pressure (pO_2) and sulphur partial pressure (pS_2), which are generally calculated from thermo-chemical data[3]. Phase diagrams are compositional in character. Which are generally constructed from empirical equilibration tests. Predominance diagrams for the relevant systems are discussed first.

3.1 Predominance diagrams

The plots of the equilibrium stability fields as a function of the oxygen partial pressure and sulphur partial pressure are depicted in predominance diagrams (Kellogg diagrams). Diagrams are plotted for three systems Fe-S-O, Cu-Fe-S-O and Ni-Fe-S-O at 400 and 600°C. Superimposed on the phase fields in these diagrams are equilibrium lines for the reaction $S + O_2 \rightarrow SO_2$. The equilibrium lines are plotted for SO_2 concentrations of 1% and 100%. Many sulphide oxidation processes operate in regions between these two SO_2 concentrations (some processes can operate at atmospheres significantly below 1 atm).

Roasting imposes a high oxygen partial pressure, and the reaction between oxygen and sulphur produces SO_2. This reaction is represented by a shift to higher pO_2 in the predominance diagram. The 100% SO_2 equilibrium line imposes a constraint; that is, the SO_2 concentration cannot exceed 1 atmosphere, unless operating under pressurized conditions.

---

[3] Thermochemical data obtained from FactSage version 6.3. FSpure database were used to obtain the invariant points in the diagrams.

When the oxygen partial pressure is constrained by the SO_2 partial pressure, further reaction is indicated by a shift to lower S_2 partial pressure and higher O_2 partial pressures along the condition of constraint—in other words, within the shaded field, towards the top left corner of the predominance diagram. This movement occurs in all three systems—Fe-S-O, Ni-Fe-S-O and Cu-Fe-S-O.

Fe-S-O. Pyrrhotite falls in the Fe-S-O system (Figure 8 Figure 9). It is stable at log pO_2 less than –26 (at 400°C) or –17 (at 600°C) over a range of sulphur partial pressures. Under high pO_2 (approximately that of air) at 400ºC the stable phase in the Fe-S-O system is $FeSO_4$ (ferrous sulphate—Figure 8). Under this condition at 600ºC the stable phase in the system is Fe_2O_3 (Figure 9). Between the pyrrhotite (FeS) stability phase field and the stable phase field at high pO_2 (that of air) lies the Fe_3O_4 (magnetite) phase field. At 400°C the Fe_2O_3 (hematite) phase field lies alongside that of Fe_3O_4 (magnetite).

To reach these final equilibrium states, roasting may follow a sequence of reactions. This sequence may involve passing through stability fields that lie between that of FeS (pyrrhotite) and ferrous sulphate. This sequence however cannot be determined from predominance diagrams as the diagrams define states at equilibrium, whereas reactions follow paths under driving forces. If we were to be infinitesimally removed from equilibrium in this process and move in a direction towards high pO_2 and low pS_2 (to left corner) of the predominance diagram, then we would stabilize, in turn, magnetite, hematite and ferrous sulphate. Whether they are indeed formed in that sequence or not has to be demonstrated empirically.

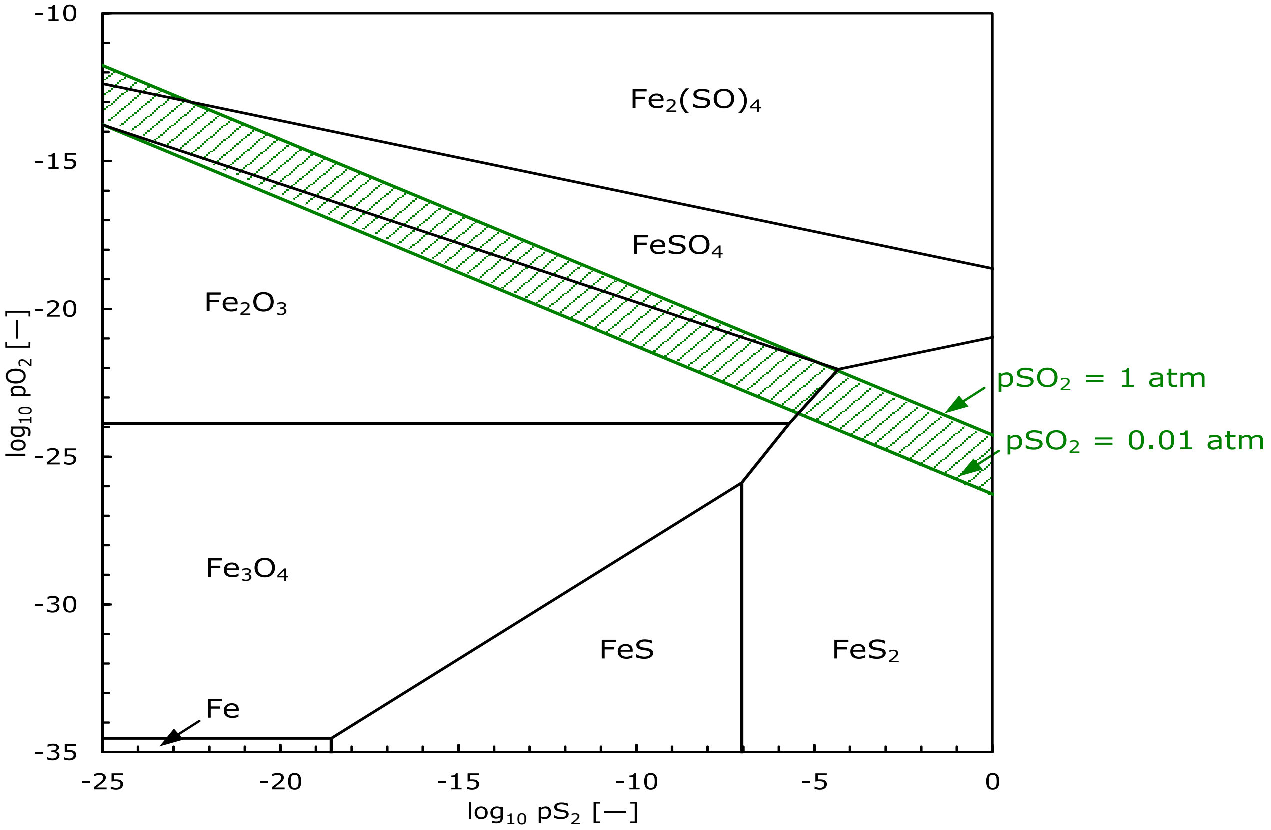

Figure 8: Predominance diagram for Fe-S-O system at 400 °C. (The units of the axes are dimensionless [−])

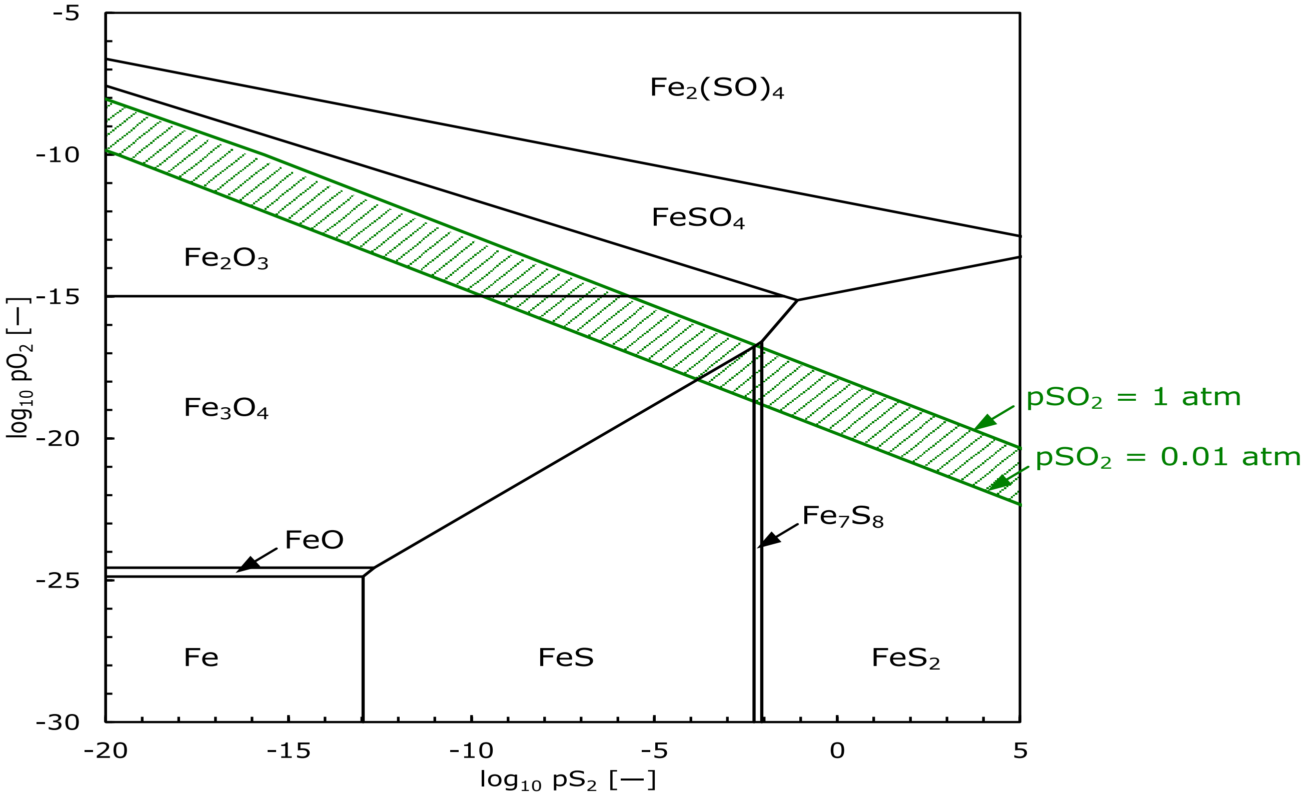

Figure 9: Predominance diagram for Fe-S-O system at 600 °C

Ni-Fe-S-O. Pentlandite falls in the Ni-Fe-S-O system. The predominance diagrams (Figure 10 and Figure 11) do not have a single phased stability filed for pentlandite. Starting with the composition of pentlandite however, the drive is still towards phase fields that are stable under high pO_2 and low pS_2. At 400 °C the final phase assemblage is $NiSO_4$ and Fe_2O_3 (hematite). At 600 °C the final phase assemblage at equilibrium is NiO and $(NiO)(Fe_2O_3)$. Although the drive is towards equilibrium during roasting, equilibrium is not reached. It is unlikely, therefore, that these phases (*viz.*, NiO + $[NiO][Fe_2O_3]$) will form in the system.

Cu-Fe-S-O. Chalcopyrite falls in the Cu-Fe-S-O system. Its phase fields are labelled 3 and 4; it is associated in these fields with pyrrhotite and pyrite respectively (Figure 12 Figure 13). At high pO_2 and low pS_2 the stable phase assemblages are $CuSO_4$ and $FeSO_4$ at 400 °C and $Cu_2O \cdot Fe_2O_3$ and Fe_2O_3 at 600 °C (Figure 12 and Figure 13). At the higher temperature the reaction path crosses phase fields in which copper and iron occur in separate phases. One of the final phases at high pO_2 and low pS_2—namely, $Cu_2O \cdot Fe_2O_3$— however, has copper and iron occuring together. During roasting phases would need to re-equilibrate in order to form this copper iron oxide, a reaction that is likely to be too slow to be noticeable.

In summary, therefore, for the system Ni-Cu-Fe-S-O, between the starting mineral and the final equilibrium assemblage there exist phase fields of nickel sulphide, iron sulphide and copper sulphide. The products of roasting are likely to correlate with phases in these phase fields.

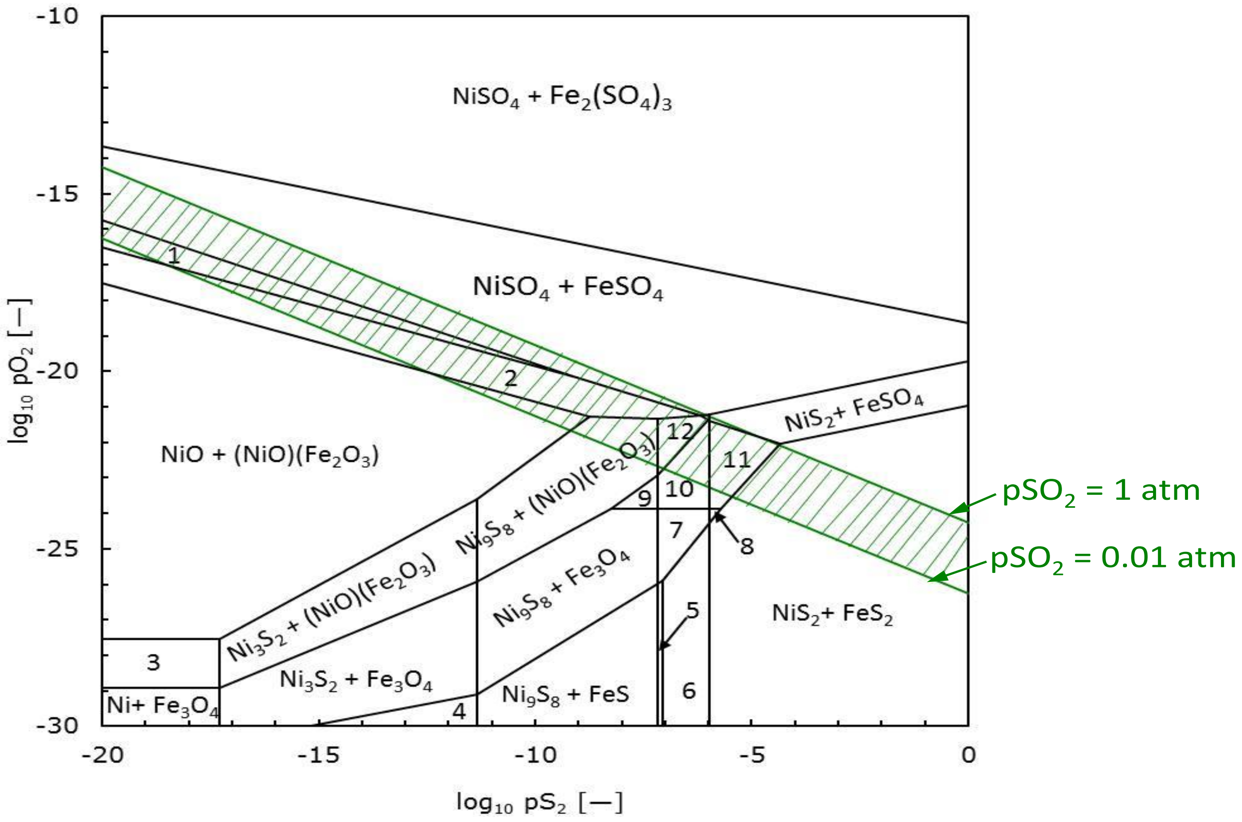

Figure 10: Predominance diagram for Ni-Fe-S-O system at 400 °C

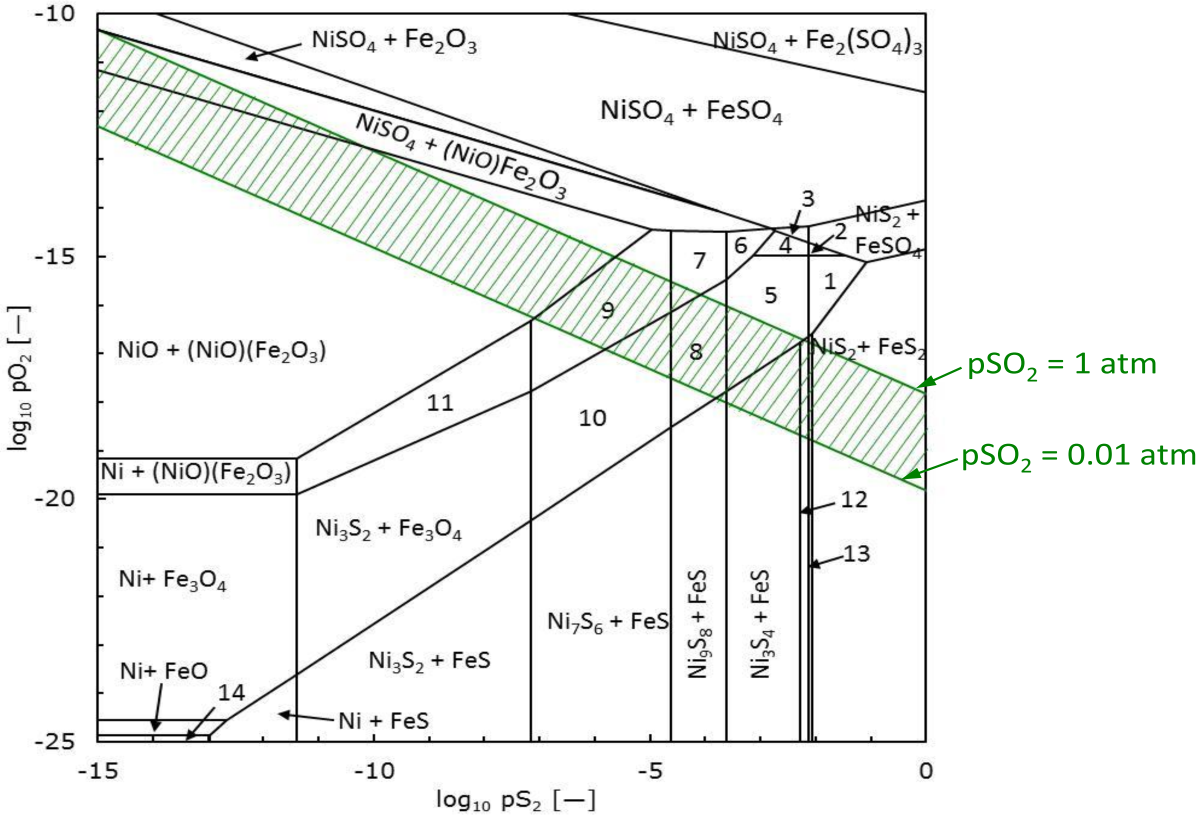

Figure 11: Predominance diagram for Ni-Fe-S-O system at 600 °C

Table 3: Stability phase fields assemblages in Figure 10 and Figure 11: assemblages at 400 °C and 600 °C

Field Label	Stability Field
400 ° C	
1	$NiSO_4 + Fe_2O_3$
2	$NiSO_4$ + (NiO)Fe_2O_3
3	Ni + (NiO)(Fe_2O_3)
4	Ni_3S_2 + FeS
5	Ni_3S_4+ FeS
6	Ni_3S_4+ FeS_2
7	Ni_3S_4+ Fe_3O_4
8	$NiS_2 + Fe_3O_4$
9	$Ni_9S_8 + Fe_2O_3$
10	$Ni_3S_4 + Fe_2O_3$
11	$NiS_2 + Fe_2O_3$
12	Ni_3S_4 + (NiO)(Fe_2O_3)
600 °C	
1	$NiSO_4 + Fe_3O_4$
2	$NiS_2 + Fe_2O_3$
3	Ni_3S_4+ $FeSO_4$
4	Ni_3S_4+ Fe_2O_3
5	Ni_3S_4+ Fe_3O_4
6	Ni_3S_4 + (NiO)(Fe_2O_3)
7	Ni_9S_8 + (NiO)(Fe_2O_3)
8	$Ni_9S_8 + Fe_3O_4$
9	Ni_7S_6 + (NiO)(Fe_2O_3)
10	$Ni_7S_6 + Fe_3O_4$
11	Ni_3S_2 + (NiO)(Fe_2O_3)
12	$Ni_3S_4 + Fe_7S_8$
13	$NiS_2 + Fe_7S_8$
14	Ni + Fe

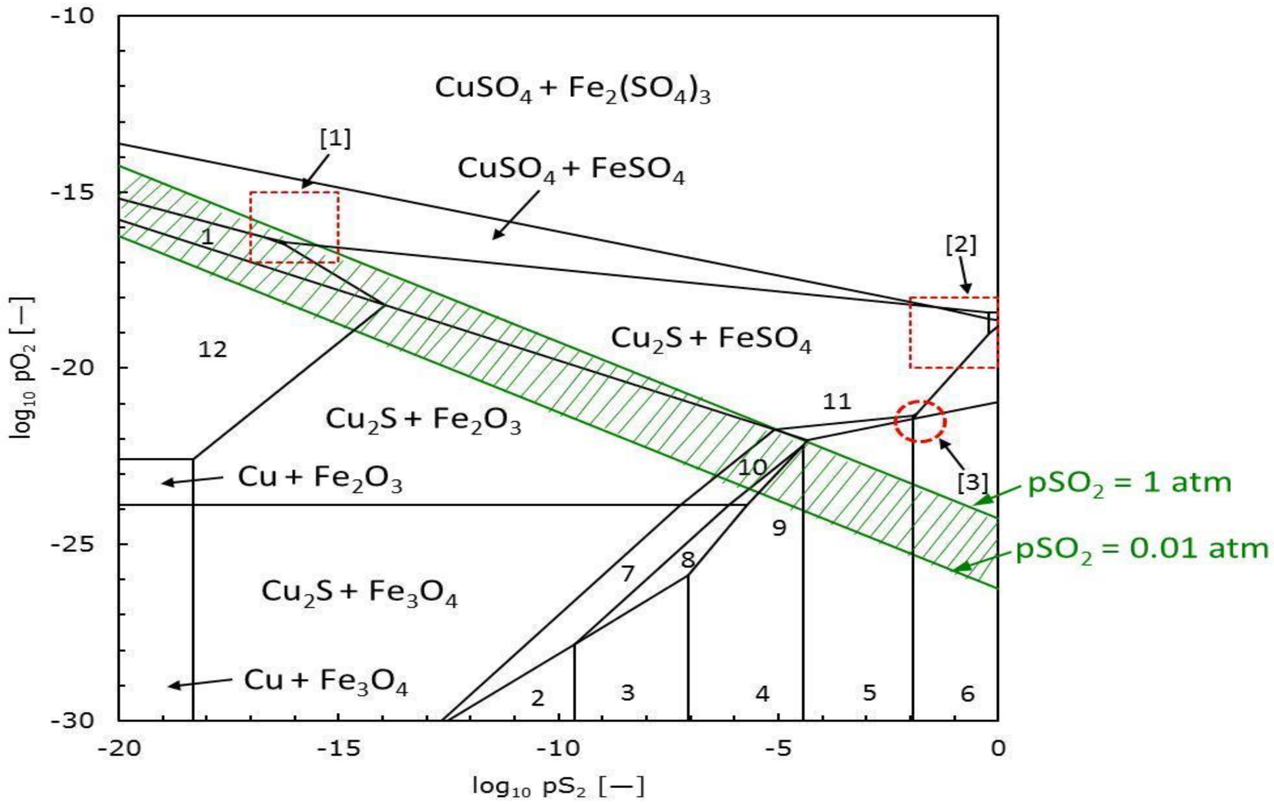

Figure 12: Predominance diagram for Cu-Fe-S-O system at 400 °C
(Diagrams of area [1], [2] and [3] are enlarged in Figures C1 to C3 Appendix B).

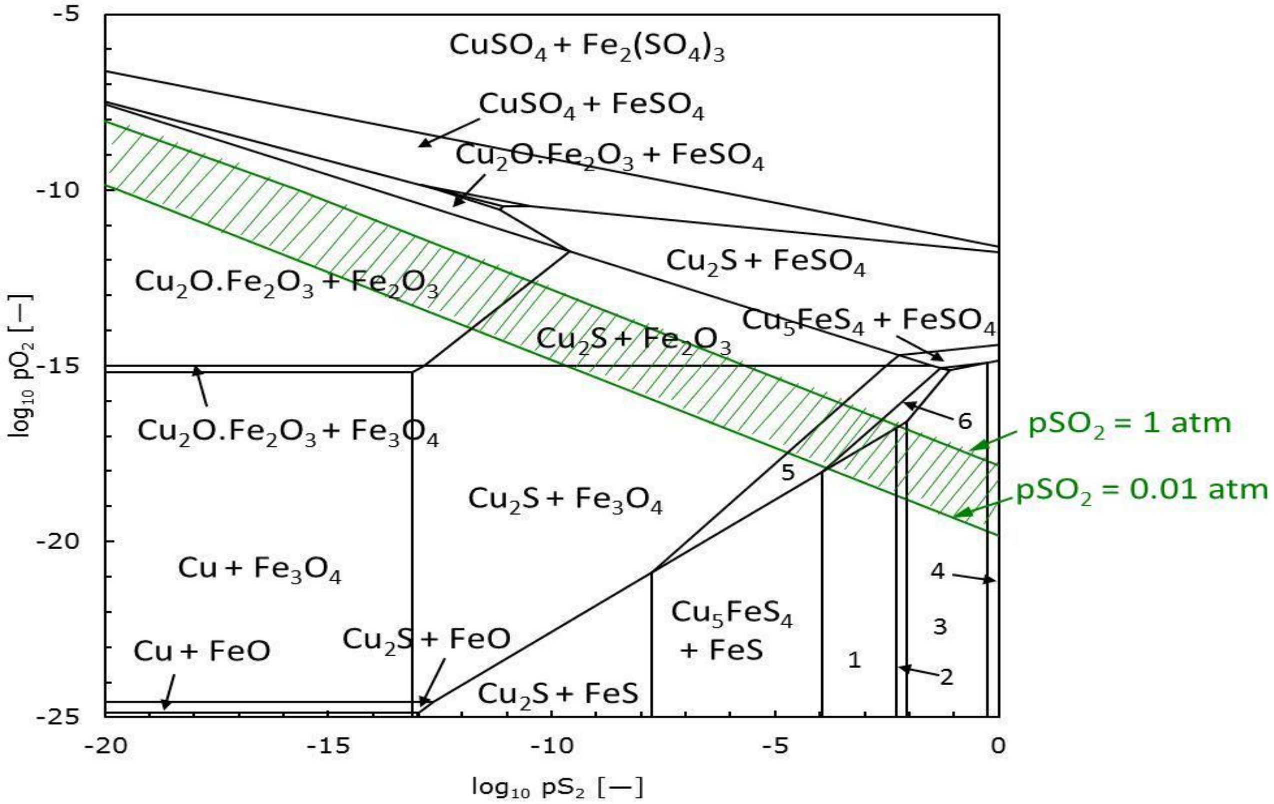

Figure 13: Predominance diagram for Cu-Fe-S-O system at 600 °C

Table 4: Stability phase fields assemblages Figure 12 and Figure 13: assemblages at 400 °C and 600 °C

Field Label	Stability Field
400	
1	$Cu_2O \cdot Fe_2O_3 + FeSO_4$
2	$Cu_5FeS_4 + FeS$
3	$CuFeS_2 + FeS$
4	$CuFeS_2 + FeS_2$
5	$Cu_5FeS_4 + FeS_2$
6	$CuFeS_8 + FeS_2$
7	$Cu_5FeS_4 + Fe_3O_4$
8	$CuFeS_2 + Fe_3O_4$
9	$CuFeS_2 + Fe_2O_3$
10	$Cu_5FeS_4 + Fe_2O_3$
11	$Cu_5FeS_4 + FeSO_4$
12	$Cu_2O \cdot Fe_2O_3 + Fe_2O_3$
600	
1	$CuFeS_2$
2	$CuFeS_2 + Fe_9S_8$
3	$CuFeS_2 + FeS_2$
4	$Cu_5FeS_4 + FeS_2$
5	$Cu_5FeS_4 + Fe_3O_4$
6	$CuFeS_2 + Fe_3O_4$

3.2 Phase diagrams

A four-component system can be presented by a tetrahedron (Figure 14). Pyrrhotite (FeS) lies on the Fe-S binary; pentlandite ($[Ni,Fe]_9S_8$) and chalcopyrite ($CuFeS_2$), on the *M*-Fe-S facet.

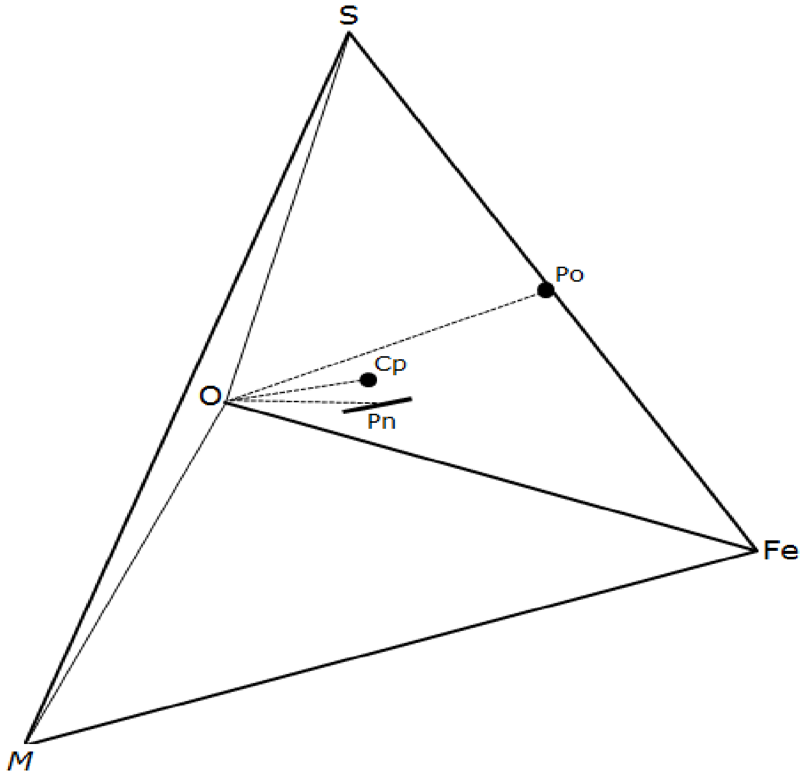

Figure 14: Compositional diagram (molar proportions) for a four component system, *M*-Fe-S-O.
Dashed lines represent oxygen reaction lines, which passes from the starting mineral to the oxygen apex. Abbreviations are listed in Table 5. *M*=Cu/Ni; Po—pyrrhotite, Cp—chalcopyrite, Pn—pentlandite.

Oxidation is represented by an oxygen reaction line, which extends from the starting mineral to the oxygen apex. As a mineral is oxidized, so the bulk composition moves along the oxygen reaction line towards the oxygen apex. The predominance diagrams for BMS under relatively high pO_2 predict phases on the *M*-Fe-S facet and iron oxides—phases on the Fe-O binary. At very low pO_2, alloy phases are stabilised—phases on the *M*-Fe binary. At high pO_2 and pS_2, sulphate phases are stabilised. They are located on two facets of the quaternary system. Tie lines emanating from a point on the oxygen reaction line connect phases in equilibrium—BMS on the *M*-Fe-S facet, iron oxides on the Fe-O binary, and SO_2 on the S-O binary.

Table 5: Minerals abbreviations.

Name	Nominal comp.	abbreviation	System
pyrite	FeS_2	py	Fe-S
pyrrhotite	$Fe_{1-x}S$	po	Fe-S
troilite	FeS	tr	Fe-S
chalcocite	Cu_2S	cc	Cu-S
covellite	CuS	cv	Cu-S
digenite	$Cu_{9-x}S_5$	dg	Cu-S
idaite	Cu_3FeS_4	id	Fe-Cu-S
chalcopyrite	$CuFeS_2$	cp	Fe-Cu-S
pentlandite	$Ni_9Fe_9S_8$	pn	Fe-Ni-S

Binary phase diagrams

This section describes equilibrium phase relations in parts of the system that relate to the roasting of PGMs. Three binary systems—Fe-S, Ni-S and Cu-S are discussed first.

Fe-S binary

The phase assemblages above 300 °C in this system are well-established (Figure C1 Appendix C). Below 300 °C the assemblages are somewhat uncertain (Vaughan and Craig, 1978). The system has a pyrrhotite solid solution above 300 °C, which persists to 1200 °C. At low sulphur partial pressures ($\log pS_2 < -12$ atm) metallic iron is stable, and at high sulphur partial pressures ($\log pS_2 > -2$ atm) FeS_2 (pyrite) and sulphur are stable (Table 6).

Table 6: Phase assemblages in Fe-S binary system at 400 and 600°C.

Assemblage	Phase composition	log pS_2 [atm]
	400°C	
Iron + pyrrhotite	$Fe^0 + FeS$	
Pyrrhotite(ss)	$Fe_{1-x}S$ $(0 \leq x \leq 0.05)$	
Pyrrhotite(ss) + pyrite	$Fe_{1-x}S + FeS_2$	–7.3
pyrite + sulphur	$FeS_2 + S$	–2.2
	600°C	
Iron + pyrrhotite	$Fe^0 + FeS$	–12.5
Pyrrhotite(ss)	$Fe_{1-x}S$ $(0 \leq x \leq 0.08)$	
Pyrrhotite(ss) + pyrite	$Fe_{1-x}S + FeS_2$	–2.0
pyrite + sulphur	$FeS_2 + S$	–0.2

Based on the binary diagram in Vaughan and Craig (1978)

Ni-S binary

The Ni-S binary system (Figure C2 Appendix C) comprises five phases, namely, Ni_3S_2 (heazlewoodite), Ni_7S_6 (godlevskite), NiS (millerite), NiS_2 (vaestite) and Ni_3S_4 (polydimite). Vaestite and polydimite can accommodate significant amounts of iron and cobalt besides nickel in their crystal structures (Vaughan and Craig 1978). The phase assemblages at 400 and 650°C are shown in Table 7. Three solid-solution series are present in this system, namely, godlevskite(ss) ($Ni_{7\pm x}S_2$), millerite(ss) ($\alpha Ni_{1-x}S$) and heazlewoodite(ss) ($Ni_{3\pm x}S_2$). The heazlewoodite(ss) is not present at 400 °C, whereas the godlevskite(ss) is not present at 650 °C. The godlevskite(ss) has a compositional range $Ni_{7.06-6.93}S_6$ and a pS_2 range of $-11.6 \leq \log pS_2 \leq -10.6$ (Table 7). The heazlewoodite(ss) has a compositional range $Ni_{3.56-2.49}S_2$ and a pS_2 range $-10.3 \leq \log pS_2 \leq -5.6$ (Table 7). The millerite(ss) compositional range does not change; it is stable at $\log pS_2 \approx -6$ (Table 7). At 635°C and higher temperatures a liquid phase is present. This phase will be present during the roasting of pentlandite at temperatures greater than 650 °C.

Table 7: Phase assemblages in Ni-S binary system at 400 and 650°C.

Assemblage	Phase composition	Log pS_2 [atm]
	400°C	
nickel + heazlewoodite	$Ni^0 + Ni_3S_2$	-17.2
heazlewoodite+ godlevskite(ss)	$Ni_3S_2 + Ni_{7.06}S_6$	-11.6
godlevskite(ss)	$Ni_{7\pm x}S_2$ (0< x < 0.43)	
godlevskite + millerite	$Ni_{6.93}S_6 + \alpha Ni_{1.00}S$	-10.6
millerite(ss)	$\alpha Ni_{1-x}S$ (0 < x < 0.08)	
millerite + vaesite	$Ni_{0.92}S + NiS_2$	-6.1
	650°C	
nickel + liquid	Ni + L(66.6 at. % Ni)	-10.7
liquid	L (66.6 - 66.1 at. % Ni)	
liquid + heazlewoodite	L (66.1 at. % Ni) + $Ni_{3.56}S_2$	-10.3
heazlewoodite(ss)	$Ni_{3\pm x}S_2$ (0 < x < 1.1)	
heazlewoodite +millerite	$Ni_{2.49}S_2 + NiS$	-5.6
millerite(ss)	Ni_xS (0 < x < 0.08)	
millerite + vaesite	$Ni_{0.92}S + NiS_2$	-1.6

Based on the binary diagram by Kullerud and Yund 1962

Cu-S binary

The phase relations in this system are well documented in literature (Roseboom 1966, Barton 1973). High-temperature (above 200°C) phase assemblages in this system were identified by Roseboom (1966). They were adopted by Vaughan and Craig (1978). A good part of the binary system (Figure C3 Appendix C) at high temperatures (below 507 °C) is covered by CuS (covellite). It has a small solid solution range. Covellite melts into high digenite and liquid sulphur above 507 °C (Fleet 2006). At the Cu-rich end of the system a solid solution of $Cu_{2-x}S$ (digenite) is dominant above 76°C. This solid solution is also referred to as high digenite solid solution (Vaughan and Craig 1978). At 435°C digenite solid solution reaches the chalcocite composition, which makes digenite(ss) equivalent to hexagonal chalcocite (Barton 1973). Phase assemblages at 400 and 600 °C are summarised in Table 8. The digenite(ss) is present both at 400 and 600 °C, but has different compositional ranges (Table 8).

Table 8: Phase assemblages in the Cu-S binary system at 400 and 600°C.

Assemblage	Phase composition	Log P_{S2}
	400°C	
sulphur + covellite	S + CuS	-2.13
covellite + digenite(ss)	CuS + $Cu_{8.78}S_5$	–2.76
digenite(ss)	$Cu_{2-x}S$ ($0 < x < 0.22$)	
Chalcocite(ss) + hex. Chalcocite	$Cu_{1.98}S$ + Cu_2S	–11.62
hex. chalcocite + copper	Cu2S + Cu	–17.29
	600°C	
Sulphur + digenite(ss)	Liquid S + $Cu_{8.74}S_5$	–0.242
digenite(ss)	$Cu_{2-x}S$ (ss) ($0 < x < 0.25$)	
chalcocite ss + copper	Cu_2S + Cu	–12.46

Based on the binary diagram by Barton 1973

Ternary phase diagrams

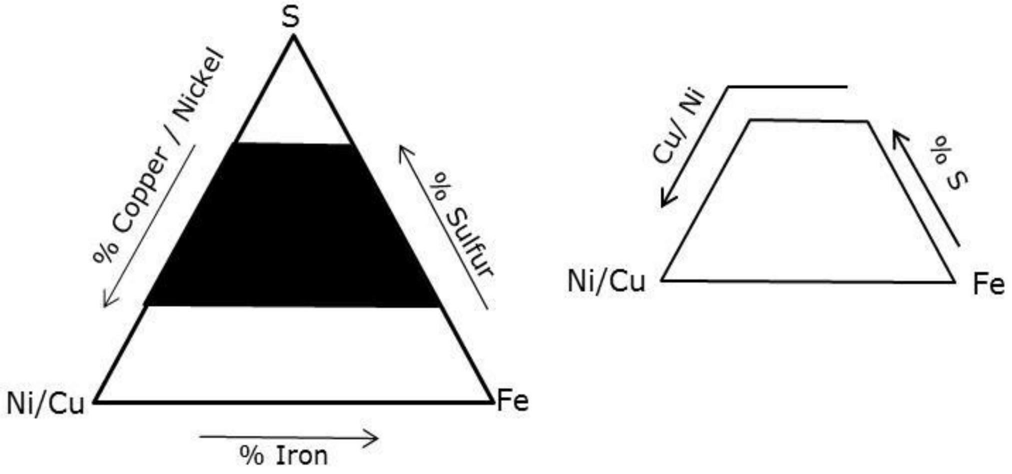

Figure 15: Illustrates the portions of interest (shaded) in the ternary diagrams, and axis labels for subsequent ternary diagrams.

Ni-Fe-S. In this system higher temperature phase relations are dominated by the monosulfide solid solution $(Fe,Ni)_{1-x}S$. However there are two other solid solutions at 400 °C and three at 650 °C (Figure 16 and Figure 17), the $(Ni,Fe)S_2$ and $(Fe,Ni)S_2$ solid solutions. They are the shaded areas at the top extremities of the figures. The monosulfide solid solution (abbreviated to *mss*) has a broad compositional range that extends across the Fe-Ni-S diagram. At 400 and 650 °C the solid solution is complete between $Fe_{1-x}S$ on the Fe-S join and the $Ni_{1-x}S$ on the Ni-S join (the two end members of the solid solution). The pentlandite composition is located below the *mss* phase field. At 650 °C the $(Ni,Fe)S_2$ and $(Fe,Ni)S_2$ solid solutions are broader—that is, their compositional range is wider. The $(Ni,Fe)_{3\pm x}S_2$ solid solution is present at 650 and not at 400° C. It is a nickel rich solid solution.

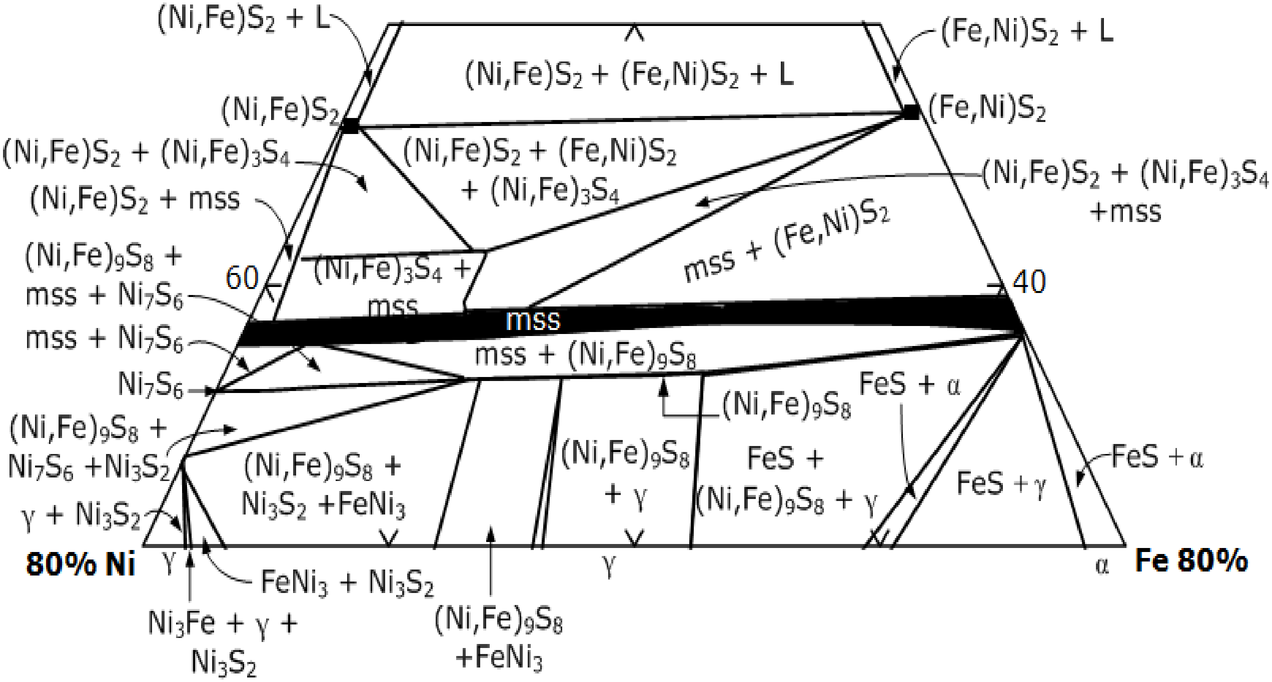

Figure 16: Phase relations in the central portion of the Ni-Fe-S system at 400 °C.
After diagrams by Craig, Naldrett & Kullerud, 1968. Axes in mole per cent.

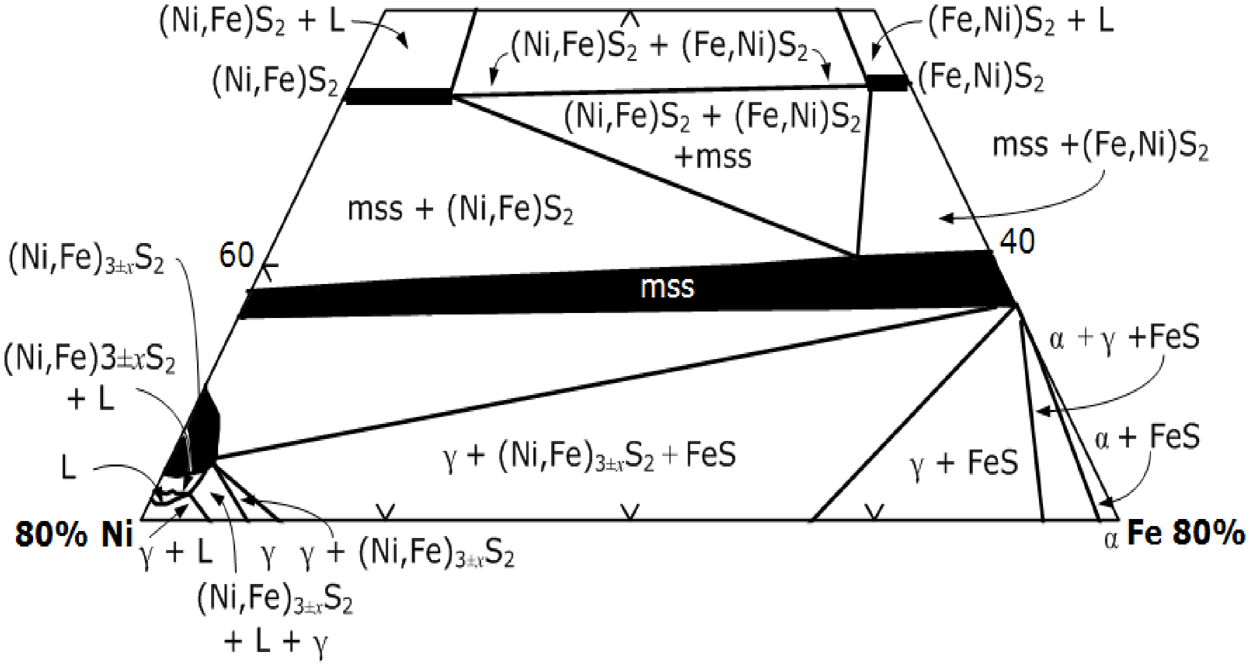

Figure 17: Phase relations in the central portion of the Ni-Fe-S system at 650 °C.
After phase diagrams by Kullerud, Yund and Moh 1969 (in Vaughan and Craig, 1978). Axes in mole percent.

Cu-Fe-S. Most three-component sulphides occur in the Cu-Fe-S system (Vaughan and Craig 1978; Yund and kullerud 1966; Mervin and Lombard 1937). It is mainly because it is found in nearly all geological environment and rock type (Vaughan and Craig 1978). The system is not straight forward. It has a number of phases; it contains extensive solid solution and non-quenchable phases (phases and compositions change during cooling, even at high rates). This makes many of the phase relations, particularly those occurring at low temperature, riddled (*ibid.*).

The phase equilibria at 400°C and above are dominated by the presence of three extensive solid solutions: the chalcocite—digenite—bornite (Cu_5FeS_4) solid solution, the intermediate solid solution (*iss*) and the pyrrhotite solid solution (Figure 18 and Figure 19) (*ibid.*).

The chalcocite—digenite—bornite solid solution is an extension of the digenite solid solution observed in the Cu-S binary system (Table 8). Its compositions extend to those more rich in iron and sulphur than stoichiometric bornite (*ibid.*). The intermediate solid solution in the central portion of Figure 18 and Figure 19 covers compositions of several minerals. It is sulphur deficient relative to chalcopyrite. The pyrrhotite solid solution has compositions that are far more iron rich relative to the *iss*. At 600 °C all three solid solutions phase fields are broader in compositional range relative to the compositional range at 400 °C.

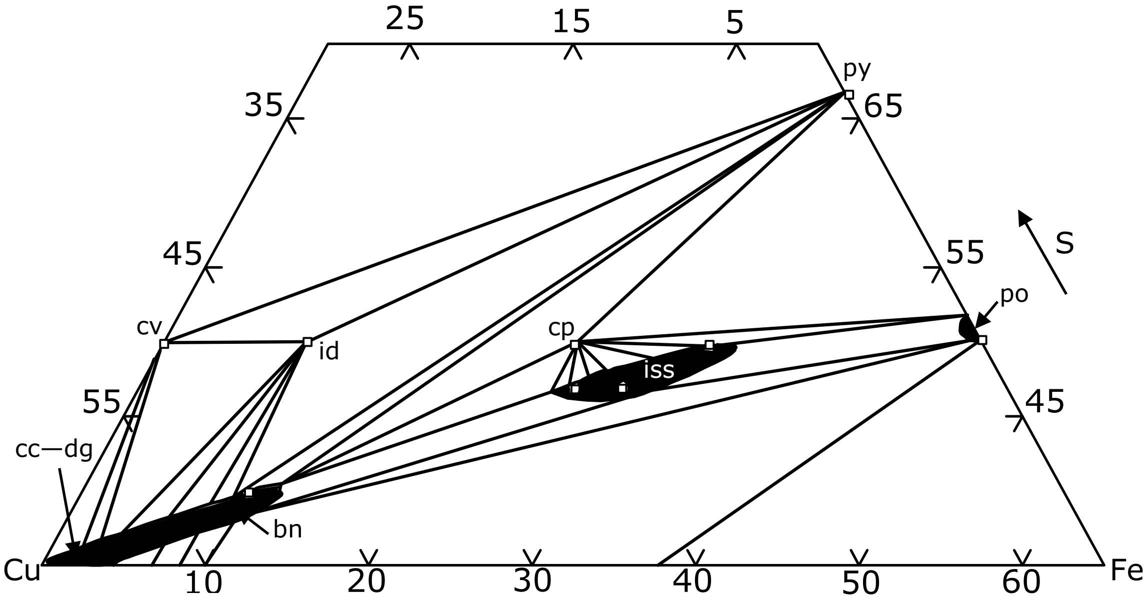

Figure 18: Schematic phase relations in the central portion of the Cu-Fe-S system at 400°C axis scaled in atomic percentage (Craig and Scott, 1974).
cp—chalcopyrite, iss—intermediate solid solution, cv—covelite, cc—chalcocite, bn—bornite, dg—digenite id—idaite, po—pyrrhotite.

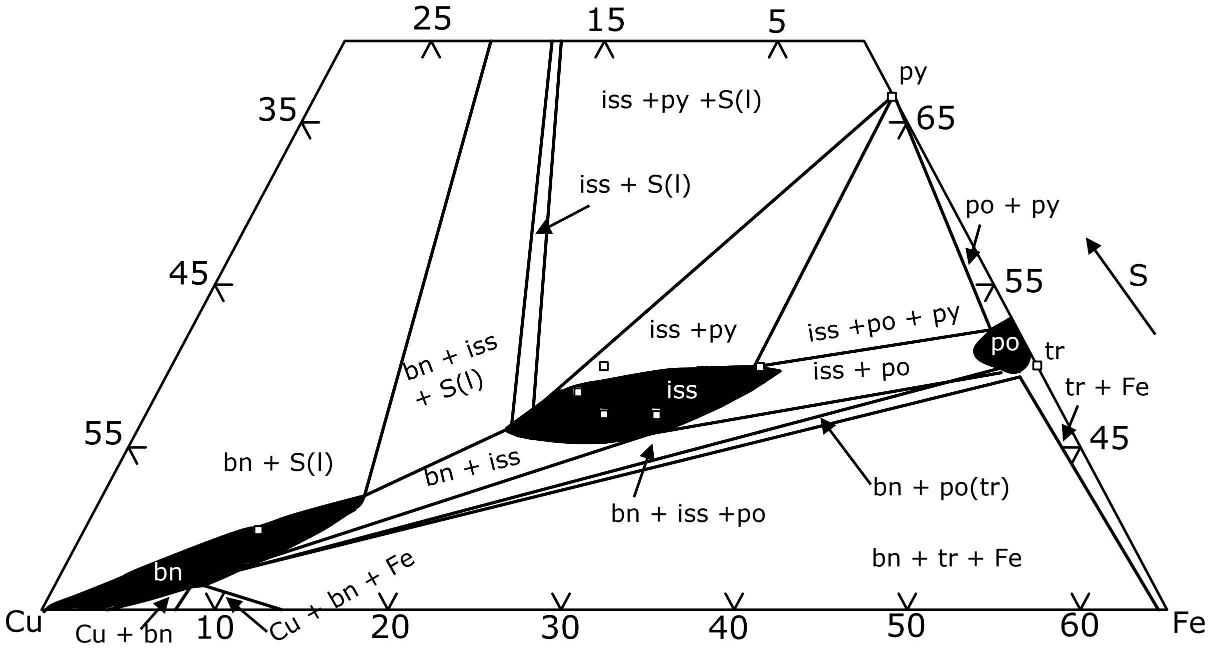

Figure 19: Phase relations in the central portion of the Cu—Fe—S system at 600 °C (After diagrams by Cabri 1973). Scaled in atomic percentage
cp—chalcopyrite, iss—intermediate solid solution, cv—covelite, cc—chalcocite, bn—bornite, dg—digenite id—idaite, po—pyrrhotite, py—pyrite, tr—troilite.

Chapter 4

Chemical kinetics — A review of the literature

Numerous studies have explored the oxidation of iron and base metal sulphides, natural and synthetic. Reactor configurations include muffle and vertical tube furnaces, fluidized beds and thermal analysis. A good portion of these studies used techniques in thermal analysis—techniques such as TG-DTA (thermogravimetry coupled with differential thermal analysis) and TG-DSC (thermogravimetry coupled with differential scanning calorimetry)—to investigate the kinetics (i.e. mechanisms and rates of reaction) of the oxidation of these minerals. The temperatures ranged from room temperature to 1000°C, only the work between 400 and 650°C is reviewed.

4.1 Pyrrhotite

The oxidation of pyrrhotite has been studied by groups that tested single particles of pyrrhotite (Thornhill and Pidgeon 1957, Kennedy and Sturman 1975) and groups that tested concentrates in which $Fe_{1-x}S$ (pyrrhotite) formed during oxidation (Pandher and Utigard 2010, Yu and Utigard (2012).

Pyrrhotite oxidizes to form iron oxide and SO_2 (Thornhill and Pidgeon 1957). This occurs in a shrinking-core manner, in which an unreacted core of pyrrhotite is enveloped by an oxide layer (*ibid.*). Thornhill and Pidgeon (1957) observed that the iron oxide layer that formed between 550° and 725°C was a duplex layer of Fe_3O_4 (magnetite) and Fe_2O_3(hematite).

Kennedy and Sturman (1975) found that the oxidation products of pyrrhotite between 425 and 520 °C are FeS_2, Fe_3O_4 and $FeSO_4$; and that from 575 to 625°C the $FeSO_4$ oxidizes to $Fe_2(SO_4)_3 \cdot Fe_2O_3$. Yu and Utigard (2012) in their study on the oxidation of nickel concentrate found that pyrrhotite disappeared (indicating full oxidation of the pyrrhotite) between 450 and 509°C and observed formation of considerable amounts of Fe_2O_3 (hematite).
There seems to be consensus in the literature that the reaction product of pyrrhotite oxidation is iron oxide. However the nature of the observed iron oxide layer differs between studies (e.g Thornhill and Pidgeon 1957 compared with Yu and Utigard 2012).

.

4.2 Pentlandite

The oxidation of pentlandite ($[Ni,Fe]_9S_8$) has been studied by a number of groups (Yu and Utigard 2012; Tenabe *et al*. 1986, cited in Xia *et al*. 2012; Zheng and Chen 1983; Misra and Fleet 1974; Dunn and Kelly 1980; Pander and Utigard 2010). Their background lies in the pure (mineralogical) and applied (chemical engineering) sciences. The samples of pentlandite used were both synthetic and the mineral in concentrates.

Several mechanisms have been postulated or inferred for the oxidation reaction. The most recent and comprehensive studies are by Xia *et al*. 2012 and Yu and Utigard (2012), and their work captures the work done by authors mentioned above. Both studies were conducted with air as atmosphere. Xia *et al* and colleagues (2012) conducted their oxidation tests in the temperature range 530°C to 600°C; Yu and Utigard (2012) conducted their tests from room temperature to 1000°C.

Between 400 and 650°C, the oxidation of pentlandite proceeds by several reactions. The first reaction is the oxidation of a "monosulfide solid solution", $(Ni,Fe)_{1-x}S$, commonly abbreviated to *mss* (Xia *et al*. 2012; Yu and Utigard 2012). This phase occurs above 450°C. (Yu and Utigard [2012] observed the phase at 450°C and Xia *et al*. [2012] between 530 and 600°C.) Reaction occurs at nuclei within pentlandite (Xia *et al*. 2012). A core-shell structure was identified consisting of kernels of *mss* in a matrix of unreacted pentlandite ($[Ni,Fe]_9S_8$), these kernels are surrounded by a fine layer of iron oxides (*ibid.*). During the conversion of pentlandite to the *mss*, iron and sulphur migrate to the surface and are oxidised (*ibid.*). The details of this oxidation reaction will be discussed later. From stoichiometric considerations the sulphide need not give up sulphur in transforming into a monosulfide solid solution.

Yu and Utigard (2012) reported the formation of a solid solution of $(Ni.Fe)_3S_4$ (violarite) in their calcined products. $(Ni,Fe)_3S_4$ (violarite) forms readily from pentlandite with the conversion requiring minimal reorganization of structures as iron is released and the remaining ions redistribute (Misra and Fleet 1974). The following reactions represent the initial stage of pentlandite transformation (Yu and Utigard 2012, who give the equations in unbalanced form):

$$(Ni, Fe)_9S_8 + O_2 \rightarrow (Ni,Fe)_{1-x}S + Ni_{1-x}S + Fe_2O_3 + SO_2 \quad [1]$$

$$(Ni, Fe)_9S_8 + O_2 \rightarrow (Ni,Fe)_3S_4 + Fe_2O_3 \quad [2]$$

$$(Ni,Fe)_3S_4 + O_2 \rightarrow (Ni,Fe)_{1-x}S + SO_2 \quad [3]$$

The second step in the reaction sequence is the transformation of the *mss* into an α-NiS (Xia *et al*. 2012; Yu and Utigard 2012). Between 495 and 733°C the composition of the *mss* has reached that of the nickel sulphide end member of the solid solution (Yu and Utigard 2012). If we accept from Xia *et al*. (2012) that the growth of the *mss* is through nucleation from pentlandite, at step two the entire particle core has fully transformed into the *mss*. So in this step the iron (Fe^{2+}) and sulphur (S^{2-}) migration to the periphery of the particle continues (Xia *et al*. 2012), only now the source of the iron and sulphur is no longer pentlandite but rather the *mss* (Xia *et al*. 2012, Yu and Utigard 2012). Stoichiometric considerations in this step also indicate that the *mss* need not lose sulphur in transforming into α-NiS. Due to continued depletion of iron and sulphur the *mss* becomes nickel rich, unstable and transforms into an α-NiS, the nickel end-member of the solid solution (Xia *et al*. 2012). As in the first reaction iron and sulphur oxidise on the particle surface (Xia *et al*. 2012; Yu and Utigard 2012; Pander and Utigard 2010).

The third reaction is the oxidation of Fe_3O_4 (magnetite) to Fe_2O_3 (hematite) at the particle surface (Xia *et al*. 2012). Before discussing this step, the oxidation of iron in reaction one and two is discussed first. In the oxidation of pentlandite to *mss* and the *mss* to the α-NiS, it is generally agreed upon that iron cations diffuse to the surface of the particle where they are oxidized (Yu and Utigard 2012; Xia *et al*. 2012; Zamalloa *et al*. 1995; Zamalloa and Utigard 1996). Iron then reacts with oxygen at the surface of the particle to form iron oxide.

The nature of this iron oxide is contested. Observations fall into two groups. One group reports finding a duplex layer of Fe_3O_4 (magnetite) and Fe_2O_3 (hematite) (Xia *et al*. 2012; T enabe *et al*. 1986, cited in Xia *et al*. 2012; Zheng and Chen 1983). A second group reports seeing only a Fe_2O_3 (hematite) layer (Yu and Utigard 2012, Dunn and Kelly 1980). Xia *et al*. 2012 reported the duplex layer in their studies between 530 and 600ºC. The observations of hematite as the oxide by Dunn and Kelly 1980 were between 460 and 700ºC. Yu and Utigard 2012 reported hematite as the oxide layer for all temperatures, with the exception being at temperatures above 785ºC (which is outside the scope of this study) where they reported reduction of Fe_2O_3 (hematite) to Fe_3O_4 (magnetite).

The oxidation of pentlandite initially forms a rapidly growing layer of magnetite (Xia *et al*. 2012; Tanabe *et al*. 1987, and cited in Pandher and Utigard 2010). It grows according to the parabolic rate law (Xia *et al*. 2012). That is, reaction three of the oxidation sequence focuses on the growth of Fe_2O_3 (hematite) from Fe_3O_4 (magnetite) to form a duplex oxide (*ibid.*). The outer layer of the duplex layer is Fe_2O_3; the inner layer is Fe_3O_4 (*ibid.*). The outer layer of

Fe_2O_3 (hematite) grows at the expense of the inner layer of Fe_3O_4 (magnetite) (*ibid.*), which also grows according to the parabolic rate law (Xia *et al*. 2012; Tanabe *et al*. 1987, and cited in Pandher and Utigard 2010). The amount of α-NiS remains constant during this step (Xia *et al*. 2012).

The final reaction is the oxidation of α-NiS to NiO (Xia *et al*. 2012), which is "sluggish". In concentrates it is so slow that all other sulphide minerals are fully oxidized while α-NiS is still oxidizing to NiO (*cf* .Thornhill and Pidgeon 1957).

4.3 Chalcopyrite

Numerous authors have studied the oxidation of chalcopyrite over the years (Thornhill and Pidgeon 1957; Meunier *et al*.1957; Levenspiel 1972; Aneesuddin *et al*. 1982; Cirkovic 1999; Cirkovic and Zivkovic 2006; Sokic *et al*. 2008; Cocic *et al*. 2011). The source of chalcopyrite sample varies. Some samples were chalcopyrite particles (Thornhill and Pidgeon 1957; Meunier *et al*.1957); others were various copper concentrates (Aneesuddin *et al*. 1982; Cocic *et al*. 2011 and citing Cirkovic 1999; Cirkovic and Zivkovic 2006; Sokic *et al*. 2008; Cocic *et al*. 2011). Tests were conducted in fluid bed reactors (Cocic *et al*. 2011 and citing Cirkovic 1999; Cirkovic and Zivkovic 2006; Cocic *et al*. 2011); thermobalances (TG-DTA) (Aneesuddin *et al*. 1982; Sokic 2008) and a vertical-tube furnace (Thornhill and Pidgeon 1957).

Several of these studies propose mechanisms for the oxidation of chalcopyrite. Many of these studies reported similar phases in their mechanisms (Aneesuddin *et al*. 1982; Cirkovic 1999, cited in Cocic *et al*. 2011; Cirkovic and Zivkovic 2006). These studies view the movement of the reaction differently. The difference lies in whether the chalcopyrite particle oxidises from the periphery to the core or vice versa. Two mechanisms, one suggested by Thornhill and Pidgeon 1957, and the other by Sokic *et al*. 2008, differ almost entirely from the rest. These two mechanisms will be briefly discussed before shifting the focus to the commonly observed mechanism (ones with similar product phases).

One of the mechanisms postulates that Cu_9S_5 (digenite) forms from chalcopyrite (Thornhill and Pidgeon 1957). Cu_9S_5 (digenite) is a simpler copper sulphide that forms through selective oxidation of Fe and S in chalcopyrite. Iron diffuses outwardly and copper diffuse towards the particle centre thus producing a digenite core. The formed digenite would undergo oxidation until it is transformed to CuO. No other study observed an initial formation of digenite.

The second mechanism was postulated by Sokic *et al*. 2008. They used chalcopyrite concentrate (this particular concentrate had the mineral pyrite [FeS_2] in it) mined at Rudnik mine (Serbia) and conducted their studies in a TG-DTA. Their suggested mechanism consists of four stages:

Stage one is the oxidation of surface layers of chalcopyrite between 330 and 357°C. The temperature at which this oxidation occurs depends on the sample heating rate. Only a small portion of elemental sulphur is oxidized in this step. There is no noticeable change in mass as indicated by the TG curves.

The second stage occurs between 404 and 440°C and involves the oxidation of the chalcopyrite inner layers and the oxidation of pyrite present in the sample. The products of oxidation during this step are Cu_2S (chalcocite), $Fe_{1-x}S$ (pyrrhotite) and SO_2 (sulphur dioxide). As no metal oxide forms, it can be concluded that this step amounts merely to the thermal dissociations of chalcopyrite and pyrite present in the sample. That is,

$$2CuFeS_2 + O_2\,(g) \rightarrow Cu_2S + 2FeS + SO_2\,(g) \qquad [4]$$

$$2FeS_2 + 2O_2\,(g) \rightarrow 2FeS + 2SO_2\,(g)$$

Stage three is the formation of metal sulphates. These include formation of iron sulphate, copper sulphate and copper oxy-sulphate;

$$FeS + 2O_2\,(g) \rightarrow FeSO_4 \qquad [5]$$

$$Cu_2S + SO_2\,(g) + 3O_2\,(g) \rightarrow 2CuSO_4 \qquad [6]$$

$$Cu_2S + 5/2O_2\,(g) \rightarrow CuO \cdot CuSO_4 \qquad [7]$$

The final stage is the dissociation of the metal sulphates. $FeSO_4$ dissociates between 554 and 613°C; $CuSO_4$ and $CuO \cdot CuSO_4$ start dissociating at 750°C. The products are Fe_2O_3, CuO, SO_2 and SO_3. That is,

$$2FeSO_4 \rightarrow Fe_2O_3 + SO_2\,(g) + SO_3\,(g) \qquad [8]$$

$$CuO.CuSO_4 \rightarrow 2CuO + SO_3\,(g) \qquad [9]$$

The proportions of SO_2 to SO_3 will be a function of temperature.

The reaction mechanism proposed by Sokic *et al*. 2008 can be summarised as follows: during oxidation chalcopyrite and pryrite undergo oxidation between 404 – 440°C to form chalcocite and pyrrhotite. Cu_2S (chalcocite) is then oxidized to copper sulphate ($CuSO_4$) and copper oxy-sulphate ($CuO \cdot CuSO_4$). The final oxidation products at 750 °C were Fe_2O_3 and CuO. Reaction fronts establish at the surfaces of the particles and move inwards through the core.

The focus now shifts to mechanisms with similar reaction products. There are two schools of thought (on the reaction mechanisms): those who argue that oxidation start at the surface of the particle and move inwards and those who argue that the opposite is the case.

Levenspiel (1972) describes the shrinking-core model. Oxidation occurs first on the outer surface of a particle, the reaction zone then gradually moves towards the centre. The unreacted core of material gradually decreases as the reaction progresses towards the centre of the particle. The total particle size remains constant.

An alternative mechanism postulate that the transformation of chalcopyrite in a fluidized bed does not occur through zoning: a particle does not oxidize from its surface towards its centre, but rather from centre outwards (Cocic *et al*. 2011). The conclusion seems to be that in the copper roasting process in a fluidized bed reactor, FeS_2 (pyrite) and part of the chalcopyrite are transformed into more stable copper and iron sulphides Cu_5FeS_4 (bornite) and FeS (pyrrhotite) (Cirkovic 1999, cited in Cocic *et al*. 2011; Cirkovic and Zivkovic 2006). Part of the chalcopyrite remained unchanged because it remained too short a time in the roaster, because temperatures were not high enough, or because some other prerequisite condition was not met during roasting—a condition such as oxygen availability at the surface of the particles or a mass-transfer limitation (Cocic *et al*. 2011). The development of the Cu_5FeS_4 (bornite) phase does not necessarily envelop the particle, but rather develops along privileged directions, crystallographic directions that favour oxidation (*ibid*.).

Cirkovic (1999, cited in Cocic *et al*. 2011) illustrated the oxidation of chalcopyrite in a spherical particle with a theoretical model that assumes a concentric particle structure where the core of the particle structure remains unchanged, but there is an increased rate of transformation from the centre of the particle to the periphery (Figure 20). The size of the remaining unreacted core depends on the concentration of oxygen on the surface, the rate of diffusion of O_2 and SO_2 through the formed reaction products and the residence time of the particle under the roasting conditions (Cirkovic 1999, cited in Cocic *et al*. 2011).

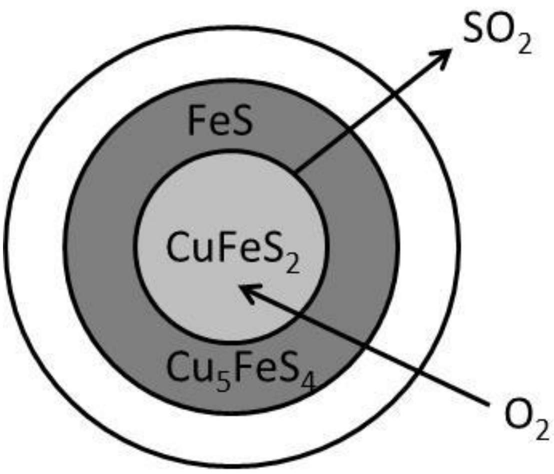

Figure 20: Theoretical mechanism of chalcopyrite oxidation (Cirkovic 1999, cited in Cocic et al. 2011)

Chalcopyrite oxidation in a fluidized-bed reactor in the temperature range 600–720°C can be reduced to the following reactions (Cirkovic and Zivkovic 2006).

$$5\ CuFeS_2 + 2O_2\ (g) \rightarrow Cu_5FeS_4 + 4\ FeS + 2\ SO_2\ (g) \qquad [10]$$

$$5\ CuFeS_2 + 5O_2\ (g) \rightarrow Cu_5FeS_4 + 2\ FeS + 2FeO + 4\ SO_2\ (g) \qquad [11]$$

Cocic *et al*. (2011) describe the spatial formation of product phases in particles. Meaning is obscured by poor English, however. It appears that after a short duration of roasting iron oxide forms on the surface of a particle of chalcopyrite; the core is unreacted chalcopyrite ($CuFeS_2$), and between it and the iron oxide layer is an annulus of *iss*, what the authors refer to as “chalcopyrite [that] is concentrate”. At no point do Cocic *et al*. (2011) describe an *iss*.

After extended roasting, the particle consists of five layers: a surface layer of iron oxide, second and third layers are Cu-enriched Cu_5FeS_4 (bornite) [likely to have compositions in within the bornite solid solution range], a fourth layer less enriched with chalcopyrite [likely to be the *iss*], and a fifth layer of unreacted chalcopyrite (Cocic *et al*, 2011). Complete roasting of a chalcopyrite particle results in a two layered particle, consisting of an oxide surface layer and a Cu-enriched bornite core (Cocic *et al*, 2011; Aneesuddin *et al*. 1983). Cirkovic (1999, cited in Cocic *et al*. 2011) found that an increase in oxidation time resulted in an increase in the magnetic susceptibility of the concentrate. Meunier and colleagues conducted studies on pieces of chalcopyrite; they studied their behaviour under a stream of air at 300–900°C. They observed that at 500°C a layer of Cu_5FeS_4 (bornite) was surrounded by Fe_2O_3 and $CuSO_4$. Reaction rates, and the formation of these products, increase with increasing temperature.

In conclusion the two mechanisms postulated for the oxidation of chalcopyrite include, first, the mechanism presented by Thornhill and Pidgeon (1957), who postulated that chalcopyrite breaks down initially to a simpler sulphide, digenite. The reaction is followed by the oxidation of the digenite. This is unlikely to happen for the following reason: there are between chalcopyrite and digenite other phase fields of higher-order sulphides such as the *iss* and the bornite(ss) (Figure 18 and Figure 19), phases that are more likely to be stabilized before digenite (a lower-order sulphide) is. A second mechanism is postulated by Sokic *et al*. (2008), one in which Cu_5FeS_4 (bornite) forms. This is more in line with phase assemblages in the Cu-Fe-S system that are likely to form during roasting.

4.4 Sulphate formation

In the oxidation of concentrates of base metal and sulphides metal sulphates may form. Cocic *et al*. 2011, Sokic *et al*. 2008, Yu and Utigard 2012, Pandher and Utigard 2010, Aneesuddin *et al*. (1983), Kennedy and Sturman (1975), Prasad *et al*. (1999), Dunn and Kelly,1977, Mackey (1991) all observed metal sulphate formation. In industrial roasters these metal sulphates build up in the roaster and in the off-gas handling system (Pandher and Utigard 2010). There is great value in understanding how these metal sulphates are formed and identifying the conditions that promote their formation. In most if not all industrial roasting operations limiting the formation of these metal sulphates is essential. The problem with metal sulphate formation during roasting is that sulphates essentially limit the amount of sulphur that can be removed during roasting. They can, furthermore, potentially decompose when they reach calcine banks where temperatures are high enough, thereby releasing SO_2 (Pandher and Utigard 2010). Significant progress has been made in understanding how conditions affect metal sulphate formation and how metal sulphates form.

Aneesuddin and colleagues (1983) observed the formation of $CuSO_4$, iron sulphate and Fe_2O_3 when chalcopyrite is heated to 850°C in air. They suggested a three stage mechanism for the sulfation of chalcopyrite to $CuSO_4$ in air: (1) direct oxidation of chalcopyrite to copper sulphate, (2) oxidation of Cu_5FeS_4 (bornite), (3) and reaction between SO_2, Fe_2O_3, SO_3 and CuO. Stage 1 occurs on the chalcopyrite particle surface where oxygen is readily available. Stage 2 occurs after the core (which has limited access to oxygen) has been transformed into Cu_5FeS_4 (bornite). Stage 3 occurs at temperatures above 550°C. In contrast to Aneesuddin and colleagues (1983) , Prasad *et al.* (1999) suggested that sulphation of chalcopyrite is not due to direct sulphation of chalcopyrite, but rather of copper sulphide, Cu_2S (chalcocite) or CuS (covellite). They suggested that chalcopyrite would first have to transform to these simpler sulphides of copper before any sulfation occurs.

Pandher and Utigard (2010) proposed a mechanism for sulphate formation following tests conducted in a thermobalance (TG) on nickel concentrates. The mechanism has three stages, which they classified into initial, middle and final stages. In the initial stage O_2 reacts with iron sulphide. It occurs to a limited depth in a particle. Diffusion of O_2 to the reaction zone is the rate-limiting step in this first stage. The pSO_2 at the reaction interface is fairly high as SO_2 evolves during oxidation. The evolved SO_2 then diffuses through the sample bed to the bulk (free board).

In the second stage the extent of the reaction increases with time, to a point where the entire iron sulphide has reacted to form magnetite or hematite. According to Pandher and Utigard (2010), as SO_2 diffuses from the surface of particles into the gas phase where the pO_2 is high, SO_3 forms. This SO_3 reacts with the oxide to form sulphates. They claim that as the depth of the oxide layer increases, SO_2 spends more time in the vicinity of the oxide, which in turn promotes sulphate formation.

The final stage is a sulphate decomposition stage, because the reaction front has reached the bottom of the crucible. There is no longer any sulphides present to sustain sulphate formation, which leads to sulphate decomposition because the P_{SO2} drops to levels that favour sulphate decomposition. Thermal decomposition temperatures in air of $Fe_2(SO_4)_3$, $CuSO_4$, $NiSO_4$ and $CoSO_4$ were reported to be 575, 625, 675 and 720°C respectively (Kolta and Askar 1975).

Hammerschmidt (2008) lists factors that would promote metal sulphate formation. These factors are (1) metal oxide with high affinity for sulphur forms metal sulphates (in platinum concentrates CaO and MgO are the most important ones—that is, sulphur driven off from sulphides could subsequently react with MgO and CaO to form $MgSO_4$ and $CaSO_4$; (2) temperature—that is, metal sulphates are stable at lower temperature and decompose at higher temperatures; (3) excess oxygen; and (4) high retention times.

Pandher and Utigard (2010) also found that high oxygen pressures support sulphate stability, Dunn and Kelly (1979) also observed higher mass gain (TGA) in their oxidation of pentlandite in oxygen compared with oxidation in air. The higher mass gain indicates more sulphate formation in oxygen.

In tests conducted using TG, when air or oxygen is introduced, initially the oxidation of metal sulphides to form oxide and SO_2 is favoured (Pandher and Utigard 2010). As SO_2 is generated the local SO_2 concentration within the bulk of the sample increases and may lead to possible formation of sulphates (Pandher and Utigard 2010).

The higher the temperature, the higher the required SO_2 partial pressure for formation of metal sulphates (Pandher and Utigard 2010). Thus the stability of all metal sulphates therefore decrease with an increase in temperature as observed in Figure 21 and the predominance diagrams.

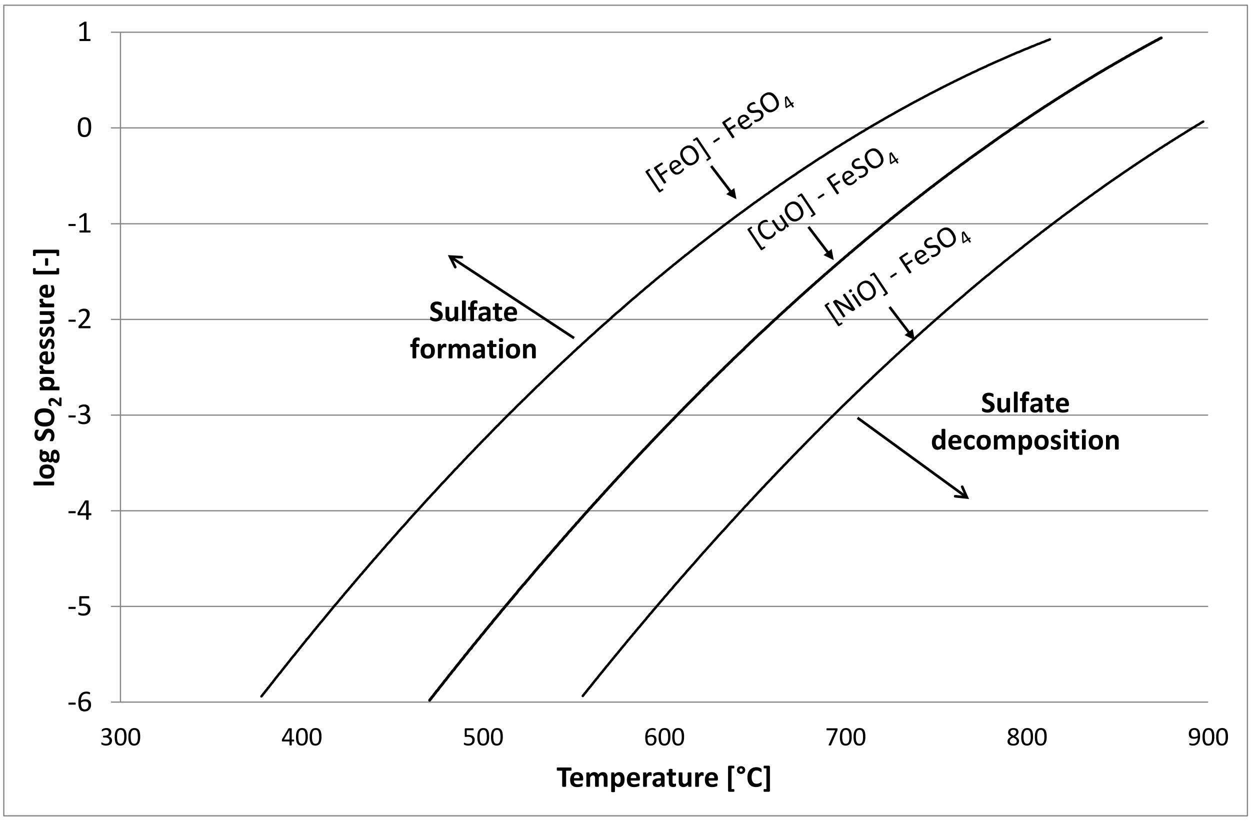

Figure 21: Equilibrium SO_2 pressure at 0.21 atm PO_2 for metal oxide-metal sulphate as a function of temperature (Pander and Uitgard 2010).

The formation of metal sulphates in TG as observed by many authors is also dependent on experimental conditions. For example the degree of sulfation is highly dependent on the sample size. Very little sulphate formation was observed in small samples (3 mg) (Mackey,1991), while in larger samples (250 mg) (Dunn and Kelly,1977) significant sulphate formation was observed. Any formed SO_2 in small samples dissipates to the bulk more readily than it does in larger samples. The local pSO_2 remains relatively constant.

One can conclude, therefore, based on Figure 21, predominance diagrams and Mackey (1991) as well as Dunn and Kelly (1979) that conditions where the bulk SO_2 partial pressure is low, iron and base metal sulphides form very little sulphates, if any.

Chapter 5

Experimental procedure

This section describes the type of equipment used to conduct the roasting tests. Main features about the equipment are highlighted, and the advantages offered by the different equipment are discussed. Procedures in conducting the tests are discussed, as well as the conditions under which they are performed. The different analytical techniques employed in analyzing the roasting products are explained.

5.1 Apparatus: reactors and their configurations

Tests were conducted in four pieces of equipment, or reactors (Table 9). Their different geometries and configurations introduced flexibilities that could be used to advantage. A rotating tube furnace being open ended was used for roasting under continuous rather than batch conditions.

Table 9: Summary of test conditions in the different equipment utilised

Properties	TG[1]	HTF[2]	RTF[3]	ARC[4]
Scale	~100mg	~7g	<200g	~50g
Feed mode	Batch	Batch	Continuous	Batch
Sample Bed	Fixed	Fixed	Disturbed	Fixed/Disturbed
Atmosphere (Air, Ar, O_2)	Continuous	Continuous	Continuous (co-current)	Fixed Volume
Pressure (atm)	0.86	0.86	0.86	Variable
Temperature (400–700^{0}C)	Ramp	@ Temp	@ Temp	Ramp
Spatial Bed temperature	Isothermal	Non-isothermal	Non-isothermal	Isothermal
ΔT_i	0	High	High	0

ΔT_i indicates the difference in temperature between the reactor and sample when the sample is introduced

1: Thermogravimetry
2: Horizontal tube furnace
3: Rotating tube furnace
4: Angular reciprocating capsule reactor

Thermal analysis

Thermogravimetry–Differential thermal analysis (TG-DTA) was used to measure mass change (TG) with temperature under controlled atmospheric conditions, while the nature of the reaction taking place (endothermic or exothermic), could simultaneously be determined using DTA (differential thermal analysis). The thermobalance was a Setaram Setsys Evolution.

Horizontal tube furnace (HTF)

A horizontal tube furnace was used to study the effect that fixed beds have on the temperature profile of a bed of certain thickness.

The horizontal tube furnace had an alumina work tube with a 65 mm internal diameter. The furnace hot zone length was 150 mm. Heating elements were $MoSi_2$. A cold finger shuttle (CFS) was used to push samples from the cold zone into the hot zone when the furnace was at temperature (Figure 22). This CFS was simply a water cooled finger with a sample holder attached to it.

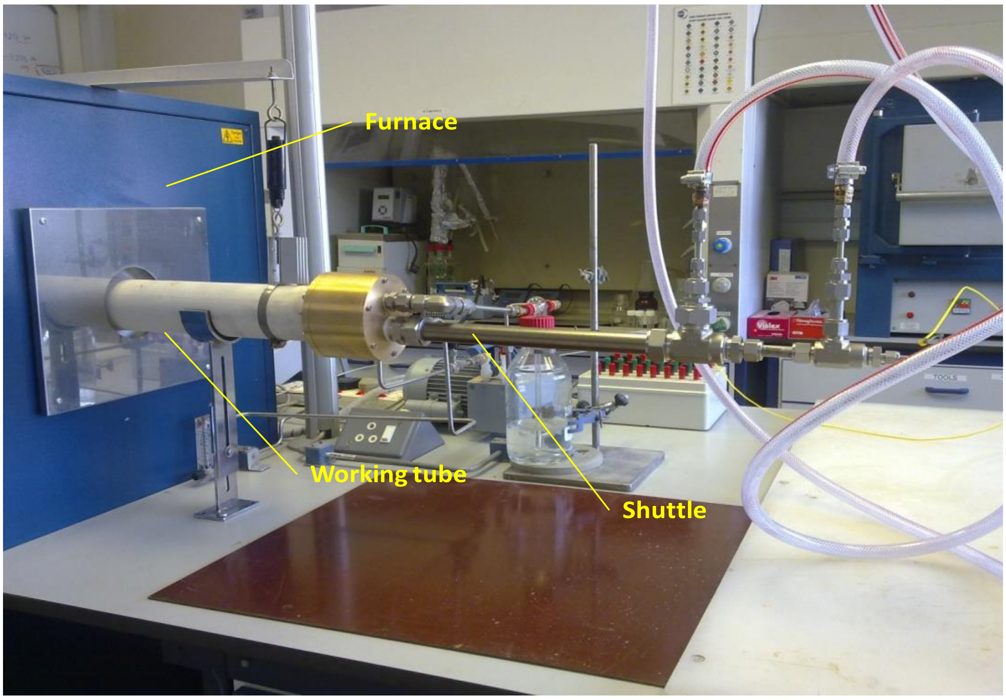

Figure 22: Picture of the horizontal tube furnace.

Rotating tube furnace (RTF)

This is the main equipment used for the roasting tests. The advantage of this furnace is that it provides good mixing of test samples.

The rotating tube furnace has a few key components which are shown in Figure 23. The furnace is externally heated (kanthal heating elements). Three thermocouples regulate the hot zone temperature. Two are positioned at each end of the hot zone. The third thermocouple is positioned at the centre of the hot zone. The furnace utilises a quartz work tube that is 1150mm in length. The tube rotates, and its rotational speed is adjustable. The furnace declination angle can also be adjusted through a crank mechanism. This furnace declination angle together with the tube rotational speed controls the residence time of the material in the tube. The hot zone of the furnace is 550 mm long. The internal diameter of the tube is 100 mm. Material feeds into the tube through a feed hopper. Just below the feed hopper is a variable speed screw feeder which feeds the material into the rotating tube. Lifters are placed inside the tube and they extend from the inlet side of the tube up to approximately 2 cm from the end of the hot zone. They are essential for good material mixing within the tube. The tube and the lifter form a tight fit, with the lifters rotating together with the tube.

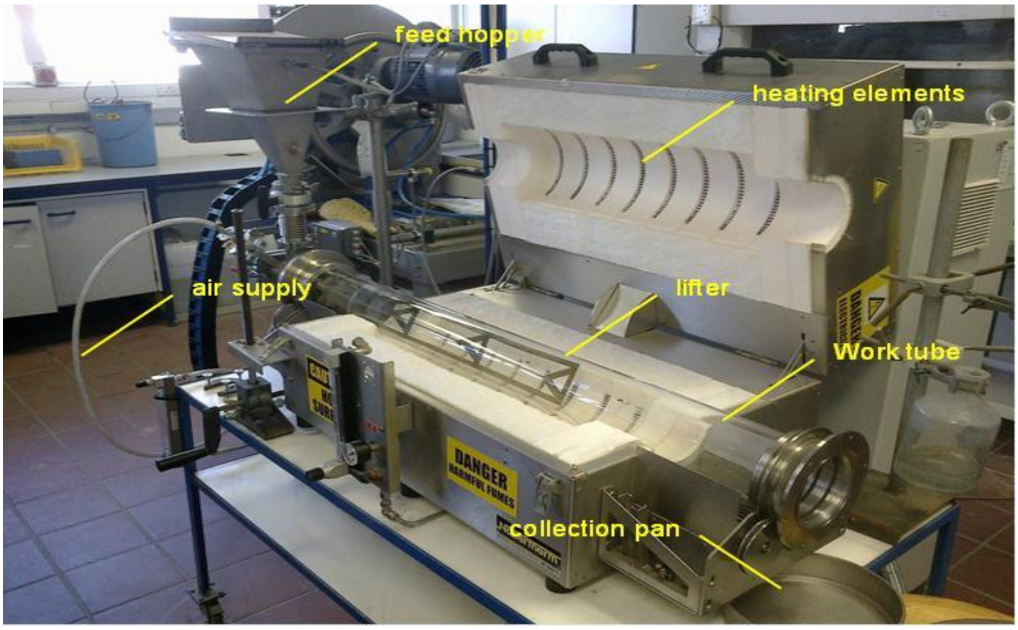

Figure 23: Photograph of the Nabertherm rotating-tube furnace (RTF) at Anglo American research centre laboratories at Crown Mines, South Africa.

Compressed air is supplied through a line with a line pressure of 500 kpa gauge. A flow meter attached to this line measures the air flow rate into the furnace. The flow meter was calibrated using ABB calibration software. A K-type external thermocouple is used to confirm the hot zone temperature profile when the furnace is at temperature.

Angular reciprocating capsule reactor (ARC)

The capsule allowed for tighter control of the amount of oxygen or air that was available for oxidation (batch type reactor). The oxidation progress of the sample for a set number of moles of oxygen could be evaluated. Pressures were measured with pressure transducers.

The capsule comprised the following components: the lifter which was 120 mm in length (the same length as the length of the hot zone), a cylinder with a 44 mm diameter and a 954 cm^3 volume and measuring devices, K-type thermocouple and gauges that measured gas and vacuum pressure (Figure 24).

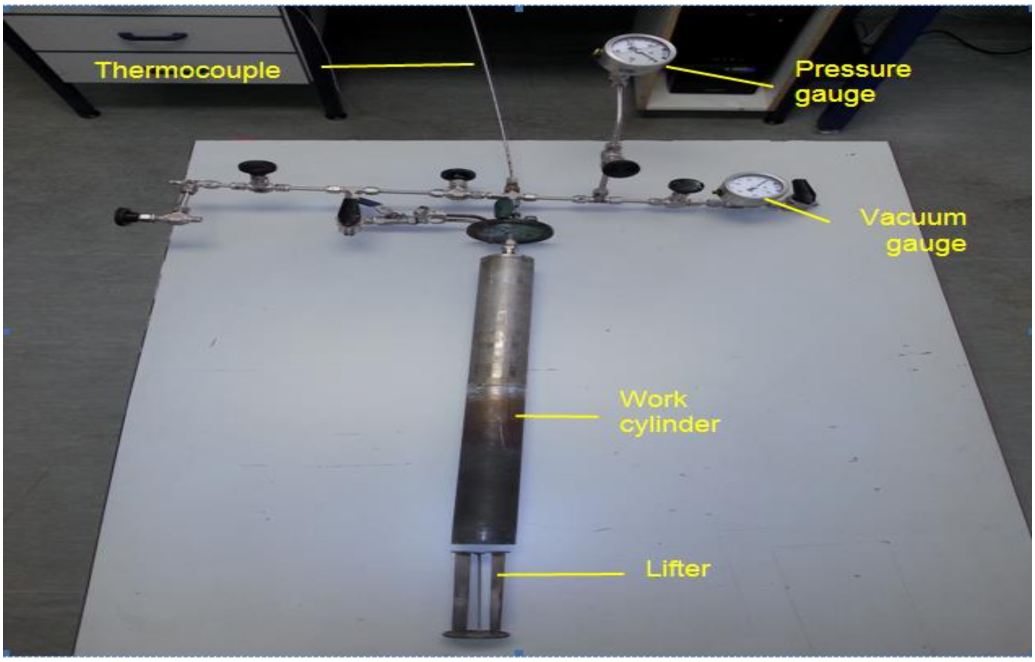

Figure 24: Photograph of the Capsule

The advantage of using this capsule is that the amount of oxygen in the capsule at the beginning of the test is known. One disadvantage of the capsule is that its working zone is only 15 mm and not the entire cylinder, only small amounts samples can be roasted at a time.

Vertical tube furnace

A Nabertherm designed furnace vertical tube furnace was used to conduct smelting tests. It utilised a mullite work tube with an 80mm internal diameter, and had a 150 mm hot zone length. The furnace has a maximum design limit temperature of 1700 °C. Heating elements were $MoSi_2$.

5.2 Variables and conditions realised

For the rate of reaction to be intrinsic to the sulphides there can be no rate-limiting factors external to these sulphides. Certain reactor configurations introduce external constraints. First, fixed beds act as bodies where processes may be limited by heat flux through the bed, a variable affected by the thermal conductivity of the bed. Secondly, the availability of oxygen and the removal of SO_2 may be hindered in beds of finely sized particles. These limitations are illustrated by temperature measurements at different locations within a fixed bed in the horizontal tube furnace (Figure 25).

Temperatures were recorded in a 10 mm thick, stationary (fixed) bed. Three thermocouples were inserted at three positions (top, middle and bottom) in the bed. The furnace controller was set at 400 °C. The top thermocouple reached the set-point temperature before the other two thermocouples. This temperature lag was a consequence of the thermal conductivity of the bed. All three profiles overshot the 400 °C mark to differing degrees: the middle thermocouple recorded the highest temperature (~590 °C); the bottom thermocouples reached only 460 °C, but maintained this temperature, for the entire period (~30 minutes) before temperatures dropped to the set-point value. These profiles can be explained by (1) the interior of the bed being "buffered" by the top and bottom layers, and (2) the availability of oxygen being lowest at the bottom of the bed (hence, the lowest rise in temperature due to the exothermic reaction). The availability of oxygen within the bottom layer of the bed is sufficient to maintain a temperature exceeding the set-point temperature.

In moving fixed beds—that is, beds where particles do not move much relative to each other, as occurs in a rotating-tube furnace without lifters—a similar lag in temperature was observed (Figure 26). This furnace was also set at 400 °C. The hot zone which coincided with length of the chamber fell between the two solid vertical lines in Figure 26. Temperatures were measured in a 4.5 mm and an 8 mm thick moving bed respectively. The 8 mm thick bed covered a longer length (two thirds compared with less than an eighth) of the hot zone to reach temperature. The temperature of the 8 mm thick moving bed did not display an overshoot in temperature, which is an indication of the extent to which the exothermic reaction proceeded.

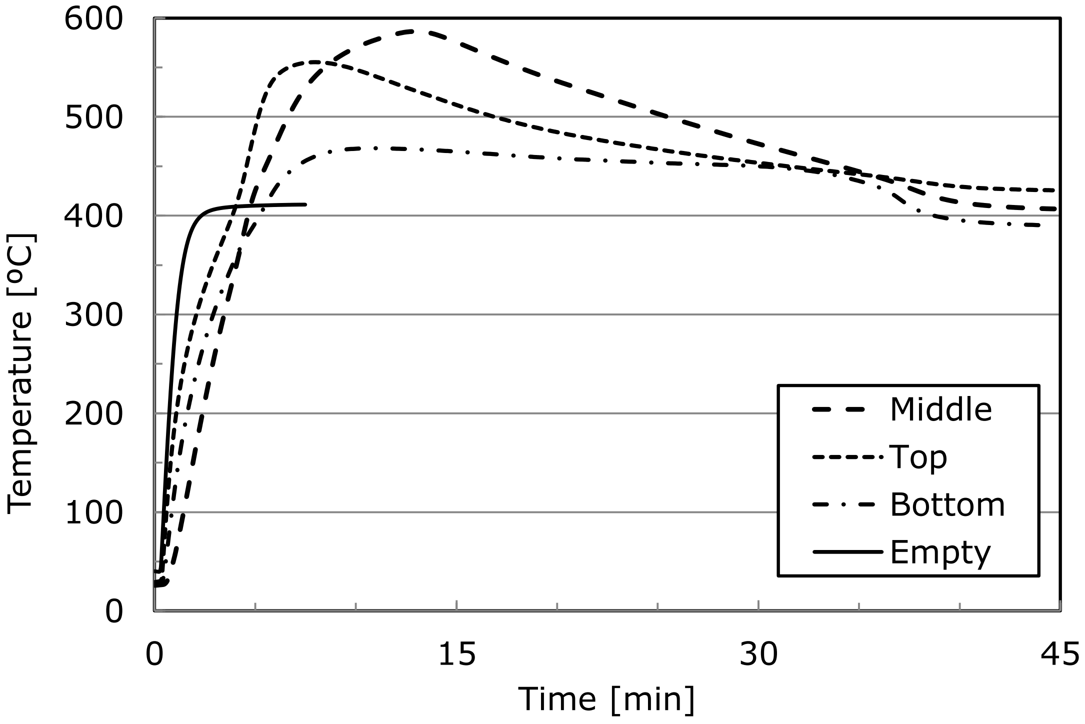

Figure 25: Temperature profiles in a 10 mm thick fixed bed.
Three thermocouples were inserted in the bed, positioned at the top, middle and bottom of the bed.
Plotted is also the profile of a thermocouple placed at the center of an empty molybdenum boat.

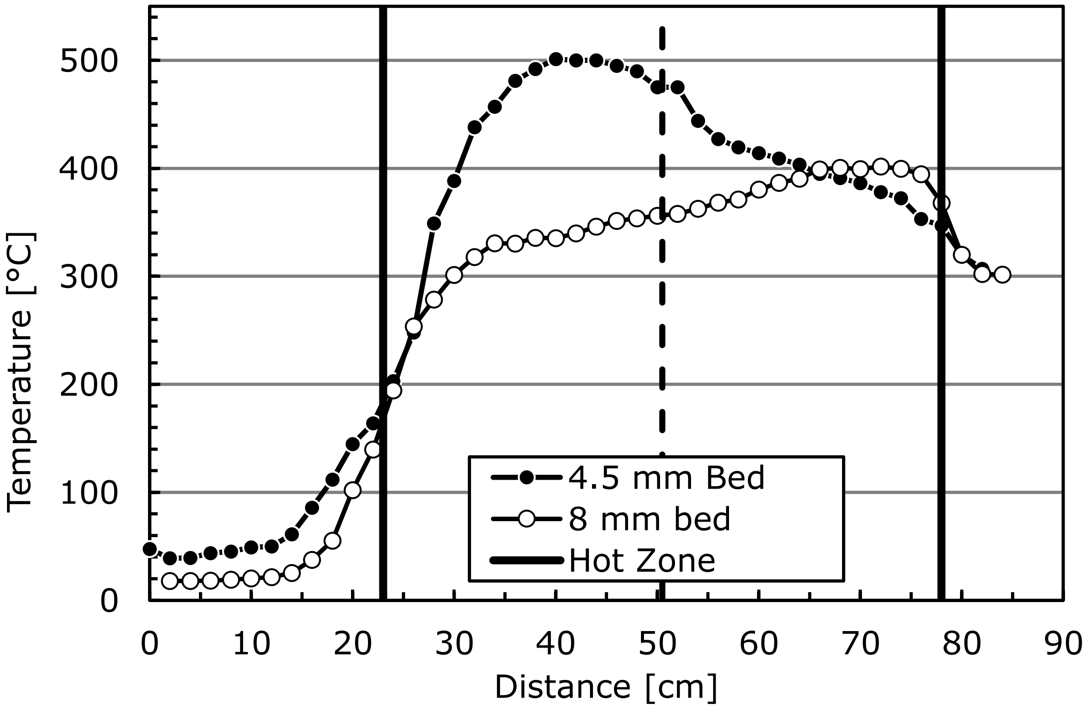

Figure 26: Temperature profile in the rotating tube furnace fitted without lifters.

The conclusion drawn from the two tests (conducted on a fixed bed in the HTF and a moving fixed bed in the RTF) was that in order to limit the rate of oxidation being influenced by external factors, the bed will need to be disturbed. A disturbed bed guaranteed better gas-solid contact, which secured good heat and mass transfer between phases.

5.3 Procedure

Horizontal-tube furnace (HTF)

The primary objective of the horizontal tube furnace tests was to measure variations in temperature through a bed of concentrate. In these tests a molybdenum boat placed at the front end of the CFS was used as sample holder. In the boat a 10mm thick sample of approximately 10g concentrate constituted the sample bed, three thermocouples were placed at three points within the bed; one half embedded at the top of the bed, another in the middle of the bed and a third thermocouple was placed at the bottom of the bed. The three thermocouples were connected to a data acquisition unit (Agilent) that logged temperatures at 1 second intervals.

Samples (boat with concentrate) were pushed into the hot zone when the furnace was at temperature. Three tests were conducted, two at 400°C and one at 700°C.

Rotating-tube furnace (RTF)

The RTF was heated from room temperature to temperature at approximately 6^0C per minute. When all three hot zone thermocouples were at temperature, the nominal temperature of the hot zone was verified with a K-type portable thermocouple.

Samples of 150 g of concentrate were used. They were fed into the furnace through the feed hopper, after which the screw feeder fed the concentrate into the rotating tube. The declination and tube rotation moved the concentrate through the tube to the discharge end. It is therefore the configuration of these two parameters that determined the residence time. Residence time in this sense was defined as the time it took the concentrate to pass through the hot zone. As the concentrate moved along the tube, the lifters together with the rotation of the furnace tube ensured good material mixing within the tube. The lifters disturbed the bed of concentrate as the tube rotated.

Discharged calcine (roasted material) was collected in a pan at the discharge end of the tube. To ensure that only material that was in the hot zone after the accretion layer had formed was sampled; the first 20g that was discharged was discarded. From the calcine that subsequently discharged, a 40g grab sample was taken. It was then sent for analyses—XRD, sulphur analysis (LECO), SEM-EDS (from polished sections) and magnetic signal measurements.

Mass losses during roasting occurred in three ways. First, some concentrate remained under the screw feeder and did not enter the tube. Secondly, as a very thin accretion layer on the tube as the concentrate passed through the hot zone. Accretion build-up was mainly observed from 600 °C and higher. The higher the temperature, the more the concentrate accreted. Thirdly, some of the very fine particles were lost to the off gas handling system as carry over.

Angular reciprocating capsule

In the capsule test samples of 30 to 50 g were used. A certain mass of sample (either 30 or 50g) was inserted into the capsule and evenly spread over the working hot zone. The capsule was then welded gas tight. To remove all the oxygen in the capsule after welding, a 4 bar vacuum was drawn. The vacuum drawing process was repeated four times. Once this process was complete, a specified air or oxygen pressure was created within the capsule. A K-type thermocouple was placed inside the capsule, at the centre of the hot zone. The thermocouple measured the temperature in the hot zone during the test. The capsule was then placed in a split shell furnace. The furnace then heated the capsule to temperature.

In some tests the capsule was manually reciprocated to ensure good bed mixing, while in others the bed was stationary. On completion of the test, the weld was cut open to collect the calcine.

Thermal analysis

Merensky PGM concentrate was analysed using TG-DTA in air and in argon. The test in argon was used as the baseline. In each of the TG-DTA runs approximately 70mg to 106mg of sample was heated with heating rates of 5°C/min (slow heating rate) and 15°C/min (fast heating rate). The gas flow was from above the sample and not from below as is the case in some TG-DTA instruments.

5.4 Analytical techniques

The products of roasting and smelting were examined and analysed by an array of techniques. These included X-ray diffractometry (XRD); scanning electron microscopy (SEM), using energy dispersive spectrometry (EDS); quantitative evaluation of minerals by scanning electron microscopy (QEMSCAN) and quantification of the amount of ferromagnetic material.

Phases were identified by XRD in a PANalytical X'Pert Pro powder diffractometer in θ–θ configuration with an X'Celerator detector and variable divergence and receiving slits. The radiation was Fe filtered Co-Kα (λ = 1.789 Å). Phases were identified by means of X'Pert Highscore plus software. The compositions of individual phases were measured by SEM-EDS in a Mineral Liberation Analyser (MLA). Mineral maps of the samples, by means of EDS, were mapped by QEMSCAN.

The percentage ferromagnetic material was determined with a Satmagan 135 (Rapiscan Systems). This instrument measured the ferromagnetic signal in a sample and correlated it to a level of magnetite (details of how the Satmagan works is in Appendix E).

5.5 Roasting test work

Roasting tests were conducted either in the rotating tube furnace or the capsule. Their respective experimental procedures were discussed earlier in this chapter. In the rotary tube furnace two types of tests were conducted, those classified as low temperature tests (below 500°C) and those classified as high temperature tests (above 500°C). Tests in the rotary tube furnace were all performed in excess air—that is, the oxygen partial pressure was at all times very close to that of (0.21atm) throughout. In the high temperature tests the temperature varied from 500 to 790°C, with residence times between 20 and 28 minutes. The high temperature test conditions are summarised in Table 10. The low temperature test conditions oxidations are in Table B3 Appendix B (insignificant oxidation observed in these tests).

Table 10: Summary of high temperature tests conditions in the rotating tube furnace.

Test ID	Temperature (°C)	Residence time (min)
T1	500	20
T2	550	20
T3	600	20
T4	650	20
T6	700	20
T7	790	28

Capsule tests were all conducted at 500°C; tests were conducted in either air or oxygen. The gas pressure in the capsule ranged between 1 bar and 2 bars gauge and residence time was 1 hour. A summary of the capsule test conditions are presented in Table 11.

Table 11: Summary of capsule test conditions.

Sample	Temperature (^{0}C)	Gas	Bed condition
B2	500	1 bar Air	Fixed
B3	500	2 bar Air	Fixed
B5	500	1 bar O_2	Disturbed*
B6	500	2 bar O_2	Disturbed

Disturbed means that it is not a fixed bed, there is good mixing of gas and solid phases.

5.6 Smelting test work

Smelting tests were conducted in a vertical tube furnace. Three samples were smelted: (1) Unroasted concentrate (also commonly referred to as fresh or green concentrate—this was the concentrate as received from Lonmin), (2) the second sample was concentrate that was roasted at 550 °C, and the third sample was concentrate roasted at 650 °C. Alumina crucibles were used as sample holders, 10g Al_2O_3 and 10g CaO were added to 100g of concentrate and thoroughly mixed. The Al_2O_3 addition improved the compatibility between the slag and alumina crucible, while CaO was added as flux. The crucible with its contents was placed inside a graphite sample holder and inserted into the furnace. To ensure that no oxidation occurred during the smelting process, the furnace was purge with argon (technical grade argon). The purge gas flushed the tube for the duration of the test. The furnace was then heated to temperature (1500 °C) at 9 °C/min. The sample was held at temperature for 30 min. Due to the corrosive nature of some of the slags produced, the sample could not be held at temperature for extended times. The sample was slow cooled in the furnace down to a 1000 °C at 5 °C/min (sample was not removed from the furnace at temperature to prevent the mullite furnace tube from cracking due to thermal shock), after which the furnace was switched off and the sample cooled inside the furnace. The products of smelting were evaluated using SEM-EDS and ICP-OES.

Chapter 6

Results—Reaction mechanisms

Discerning reaction mechanisms is central to any study in chemical kinetics. The mechanisms of oxidation of pyrrhotite, chalcopyrite and pentlandite—specifically the three main sulphides in a sample of Merensky concentrate from Lonmin—are the subject of this chapter. These mechanisms were derived from phase diagrams (mindful that they report phase relations at equilibrium) and from observations made in kinetic studies, both in the literature and in this study.

6.1 Reaction mechanisms

Two principles inform the way we derive mechanisms of oxidation of the different phases that are present in the concentrate. The first is the inherent relationship between phases in the Cu-Fe-S-O and Ni-Fe-S-O systems. These systems can be represented by tetrahedra (Figure 14). A base metal sulphide lies on the *M*-Fe-S facet (where *M* denotes either Cu or Ni). Oxidation drives the composition of the system (as a whole) towards the oxygen apex. As it does so, SO_2 is formed and the compositions of sulphides on the *M*-Fe-S facet move away from the sulphur and iron apices towards the *M* (Cu and Ni) apex. This move establishes a sequence: higher-order sulphides will appear before lower-order ones during oxidation. By this principle, one can expect an *iss* or an *mss* to appear in the products of oxidation before Cu_5FeS_4(ss), the bornite solid solutions, or NiS(ss), a millerite solid solution.

The second principle addresses an inherent variation in samples undergoing oxidation. Despite holding a test at one set of conditions (of temperature, residence time and oxygen partial pressure), the metal sulphides in that sample show a degree of variation in respect of phases and their compositions. This variation within a single sample implies that individual particles of metal sulphides have attained different degrees of oxidation in that sample. Attaching a fixed set of conditons to a degree of oxidation is problematic, therefore. But it is possible to extract information about phases and steps in the sequence of reactions from mineral to final oxidised product. These two principles inform how mechanisms were derived in the oxidation of pyrrhotite, chalcopyrite and pentlandite.

The reactions examined fall into three categories. A change undergone in a reaction can be grouped as (1) structural alone—i.e., a change in crystal structure—(2) structural and stoichiometric, and (3) stoichiometric alone (implied of cause is a concomitant change in crystal dimensions), as when the composition of a solid solution changes steadily.

Reaction mechanism of pyrrhotite transformation

There is evidence (SEM-EDS) indicating that there are instances where pyrrhotite ($Fe_{1-x}S$) dissociates to FeS_2 (pyrite).

$$4FeS + O_2 = Fe_3O_4 + FeS_2 + 2SO_2 \qquad [12]$$

This reaction is consistent with chemical thermodynamics (Chapter 3). The sulphur partial pressure needed to stabilize FeS_2 (pyrite) rises according to the following reaction.

$$2SO_2 = 2O_2 + S_2 \qquad [13]$$

$$K = \frac{p_{O_2}^2 \cdot p_{S_2}}{p_{SO_2}^2} \qquad [14]$$

In other instances pyrrhotite reacted to form iron oxide directly. It is a type-two reaction—that is, it involves both structural and, possibly, stoichiometric changes. The evidence for this reaction lies in ferromagnetic measurements (Figure 27), XRD (Appendix D) and SEM-EDS (Table 12, Figure 28 to Figure 30). The form of iron oxide is unclear—*i.e.*, whether it is Fe_3O_4 (magnetite) or Fe_2O_3 (hematite). Although XRD identified an iron oxide (Appendix D, Figure D3 and Figure D5), the two oxides could not be distinguished, because the reflections shouldered each other and they were not sufficiently leptokurtic.

There was an increase in ferromagnetic content (as measured in a Satmagan 135) with an increase in temperature (350–450 °C) for a fixed duration of roasting (Figure 27). This trend decreased at higher temperatures (above 450 °C). Thermodynamically hematite, and not magnetite, is stable at the temperatures at which roasting was conducted (Muan and Osborn, 1965). Magnetite would be stable at lower pO_2, but these potentials were never realized in the rotating tube furnace. The only possible explanation for the formation of magnetite, therefore, is that reaction kinetics controlled its formation. In other words, magnetite was a preferred intermediate form of iron oxide in the oxidation sequence that drove towards hematite, the thermodynamically stable form of iron oxide under these conditions. It would appear that at higher temperatures one of two things was happening: either the reaction kinetics did not hinder the direct formation of hematite, or magnetite, as before, was formed but was more readily oxidized to hematite. The latter is supported by the observations of Xia *et al* (2013) that a duplex of magnetite and hematite was formed. With increasing temperature, furthermore, although magnetite was formed rapidly, it was oxidized still more rapidly to hematite. Hence the decreasing levels of magnetite observed with increasing temperature above 450 °C.

EMPA (electron probe microanalyzer) could not accurately determine the composition of the iron oxide formed. The oxide was either too porous, non-uniform and in some instances was less than 3 µm thick.

The EDS analyses for the typical iron oxide formed during oxidation are listed in Table 12. The analyses are of the phases identified in Figure 28 to Figure 30.

Table 12: EDS analysis of the phase identified during pyrrhotite oxidation.

Analysis Figure	1 28	1 29	Particle 30
	Weight %		
S	39.3	56.1	0.39
Fe	60.8	43.9	79.52
O	–	–	20.1
	Atomic %		
S	52.9	69.0	0.45
Fe	47.1	31.0	52.89
O	–	–	46.66
Stoichiometry	$Fe_{0.89}S$ (pyrrhotite)	$Fe_{0.45}S$	(1)

(1) the measured composition does not correspond to any of the expected form of iron oxide (magnetite, hematite or maghemite). It may possibly be a two phase oxide.

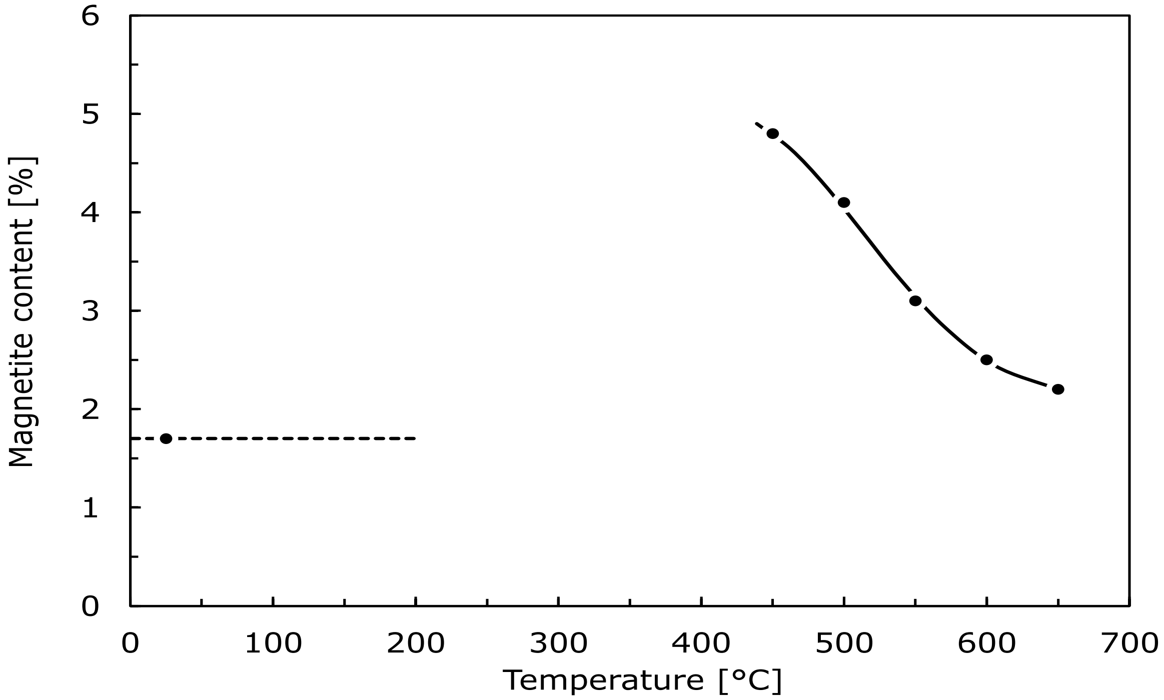

Figure 27: Percentage magnetite in the sample as a function temperature, measured by Satmagan.
(The samples were roasted in the RTF for 20 minutes).

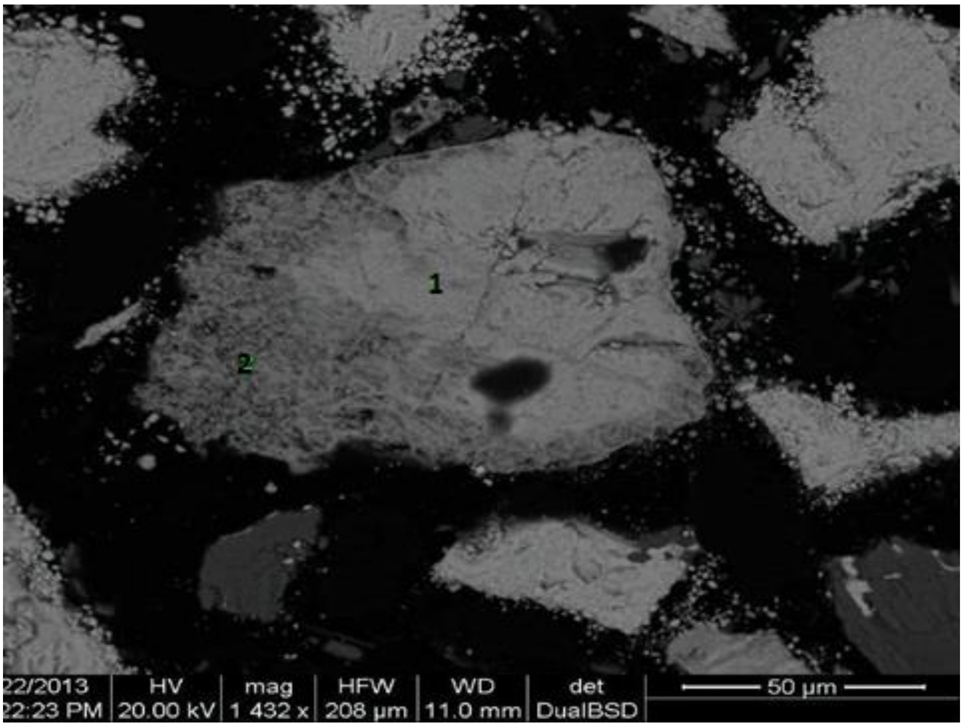

Figure 28: Backscattered-electron (BSE) image of a representative particle of pyrrhotite with iron depleted sulphide core.
(1) $Fe_{0.89}S$; (2) Fe- oxide

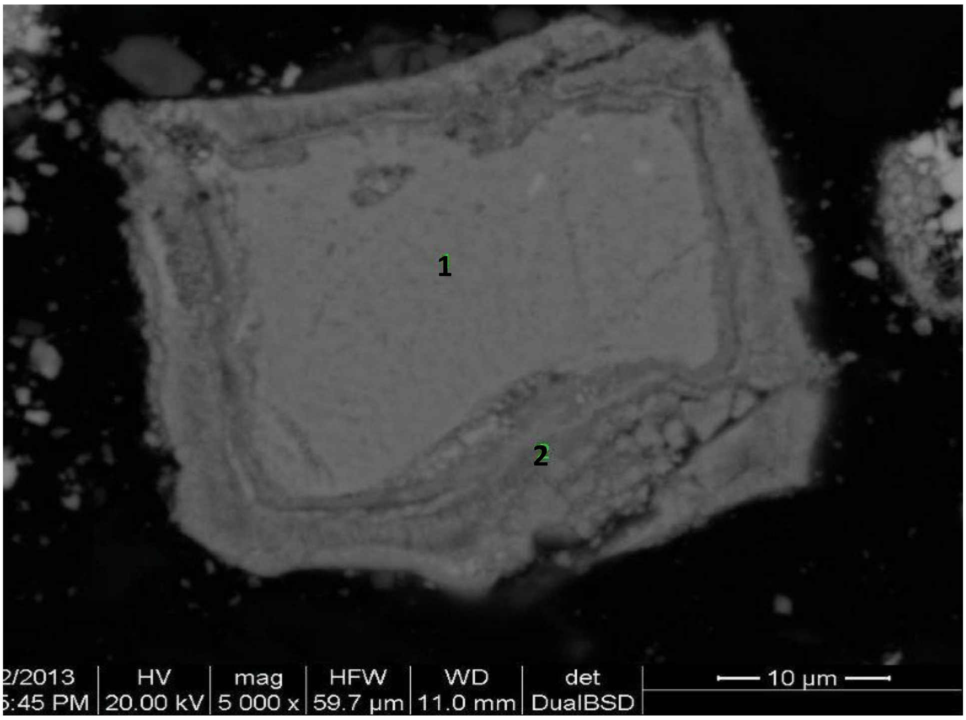

Figure 29: Backscattered-electron (BSE) image of a particle of pyrrhotite transition. (1) $Fe_{0.89}S$; (2) Fe- oxide

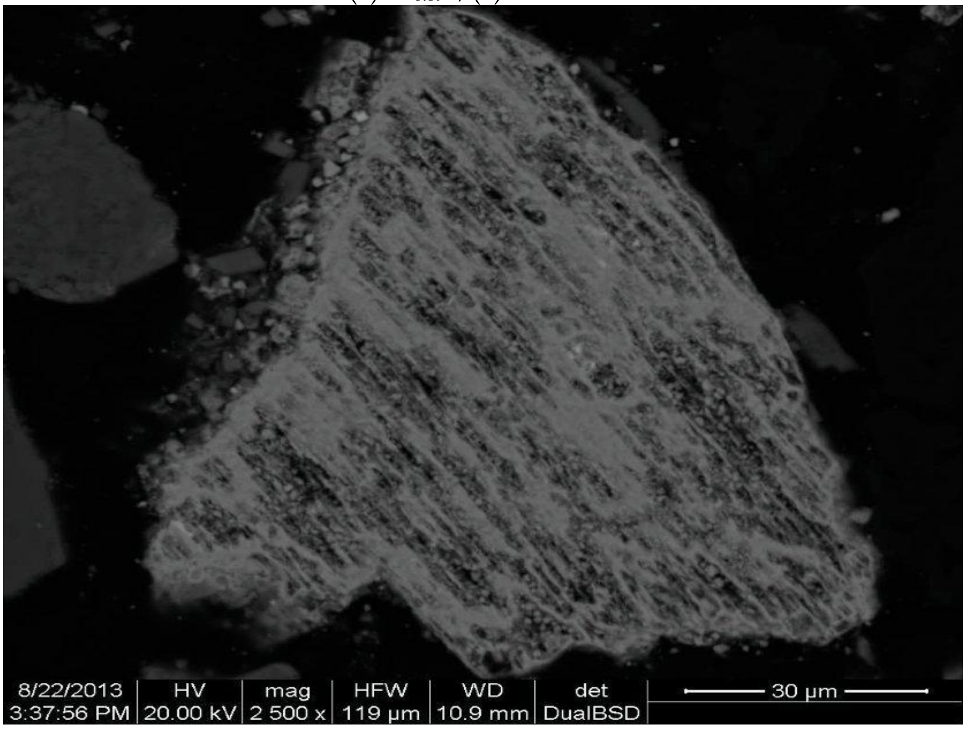

Figure 30: Backscattered electron (BSE) image of a fully oxidised pyrrhotite particle.

Reaction mechanism of pentlandite transformation

At least three reactions characterized the oxidation of pentlandite ($[Fe,Ni]_9S_8$) to lower sulphides. First, pentlandite changed to a monosulfide solid solution (abbreviated *mss* and conforming to the stoichiometry ([Fe,Ni]S). The evidence in support of this change is twofold. First, the compositions of particles subjected to air at elevated temperatures (~400 °C) for short durations fall in the *mss* phase field (Figure 31 and the first six analyses in Table 13; the analyses are drawn from Figure 32 to Figure 35). Secondly, in XRD there was a shift in the reflections of pentlandite (Appendix D). This is a type-two reaction: pentlandite undergoes both structural and stoichiometric changes during this reaction. The transformation was rapid: it was complete within three and half minutes at 400 °C, and the *mss* occurred throughout the particle (Figure 32). The reaction included the formation of iron oxide on the surfaces of particles (point 3 in Figure 32). According to Xia *et al.* (2012) iron (as Fe^{2+}) diffuses through pentlandite to the surface of a particle, where it reacts with oxygen. The stoichiometric formula for pentlandite indicates that the mineral does not need to give up sulphur during this reaction:

$$(Fe_xNi_y)_9S_8 + \tfrac{2}{3}O_2 = 8(Fe_xNi_{\frac{9}{8}y})S + \tfrac{1}{3}Fe_3O_4 \qquad [15]$$

(Reaction [15] can be written expressing the iron oxide as either Fe_3O_4 [magnetite] or Fe_2O_3 [hematite].) Reaction [15] was observed by Xia *et al.* (2012) and Yu and Utigard (2012).

Table 13: EDS Analysis of the sulphide phases identified during pentlandite oxidation.

Analysis	1	2	1	1	2	1	1	1	1
Figure	32	32	33	34	34	35	–	–	–
					Weight %				
S	37.8	36.0	38.1	38.8	37.9	39.4	33.0	32.0	35.1
Fe	30.8	8.6	21.46	12.2	8.0	9.9	4.3	3.4	2.8
Ni	31.4	55.4	40.44	49.0	54.0	50.7	62.2	64.6	62.1
O	–	–	–	–	–	–	0.5	–	–
					Stoichiometry				
Phase	mss	mss	mss	mss	mss	mss	$Ni_{1\pm x}S$	$Ni_{1\pm x}S$	$Ni_{1\pm x}S$
S	1.00	1.00	1.00	1.00	1.00	1.00	1.00	1.00	1.00
Fe	0.47	0.14	0.32	0.18	0.12	0.14	0.07	0.06	0.05
Ni	0.45	0.84	0.58	0.69	0.78	0.70	1.03	1.10	0.97
O							0.03		

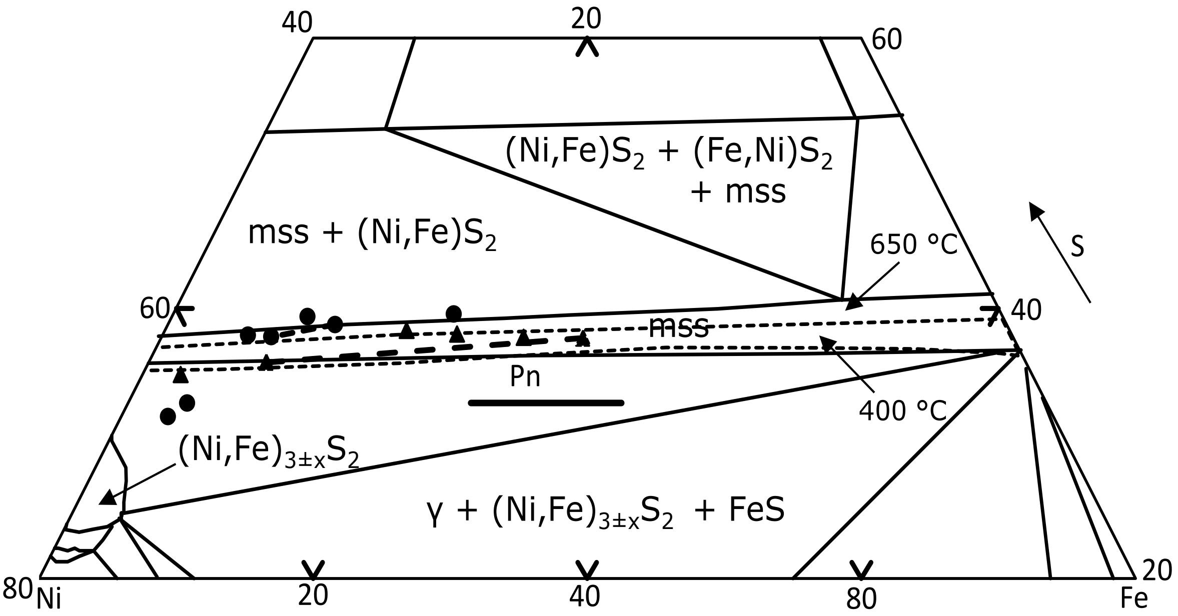

Figure 31: Measured compositions set against phase relations in the Ni-Fe-S system (see chapter 3).

● denotes compositions of particles roasted at 550 °C. ▲ denotes compositions of particles roasted at 650 °C. The dashed line connects the compositions of two phases within a single particle.

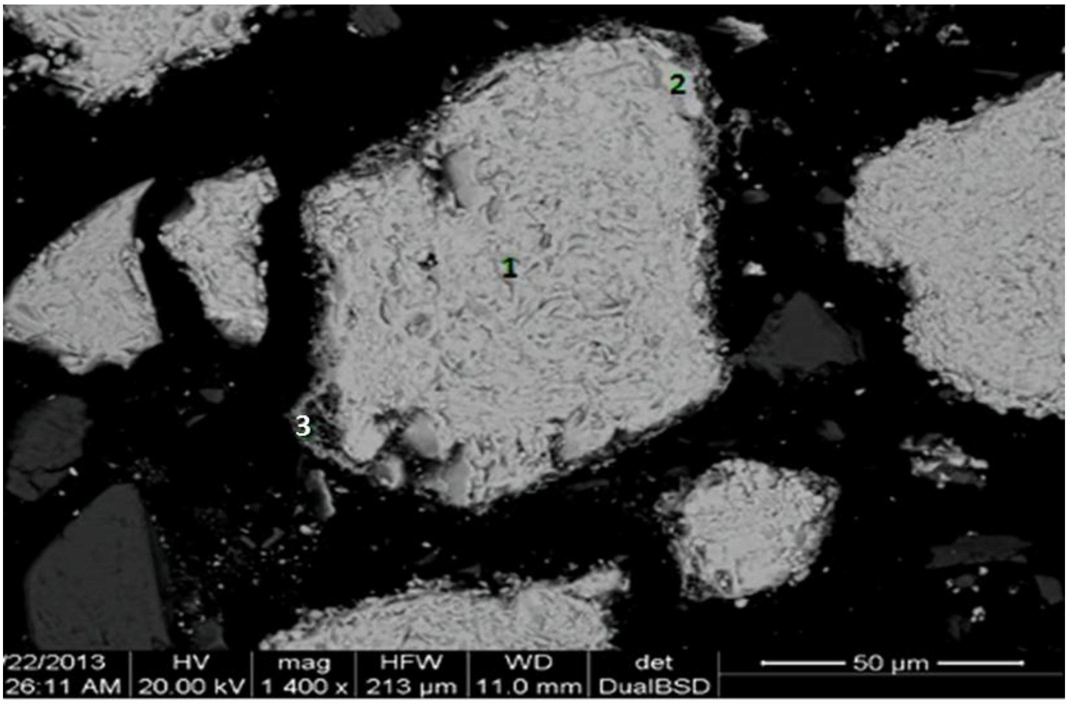

Figure 32: Backscattered-electron (BSE) image of a particle of *mss* and iron oxide after oxidation (formerly pentlandite).
(1) Ni$_{0.45}$Fe$_{0.47}$S; (2) Ni$_{0.84}$Fe$_{0.14}$S; (3) Fe-oxide

These authors also observed the second reaction in the sequence, namely, the compositional change of the *mss* (Xia *et al*. 2012; Yu and Utigard 2012). The reaction is of type three: the phase retains its crystal structure although stoichiometry changes. The span of the *mss* at higher temperatures (400 and 650 °C) reached from NiS (millerite) to $Fe_{1-X}S$ (pyrrhotite); the *mss* can accommodate cation and anion deficiencies (see phase diagrams, Figure 16 and Figure 17). As in reaction 1, during oxidation iron (as Fe^{2+}) diffuses through the *mss* to the surface of a particle, where it reacts with oxygen. In the process the *mss* becomes increasingly depleted in iron (Xia *et al*. 2012). These changes were observed in pentlandite roasted in the laboratory for the current study. After the first reaction had taken place, the composition of the *mss* moved towards the NiS end-member (Table 13; Figure 32 to Figure 35). The evidence for this compositional change is indicated in the SEM-EDS analyses of this phase in particles at different stages of oxidation (Table 13). Differences in composition were evident not only between particles (at different stages of oxidation), but within some particles: the *mss* in one part of these particles was more oxidized than the *mss* in another part (Figure 31, where the two compositions are plotted and linked by dashed lines; Figure 32 and Figure 34 show particles from the same sample; the different sulphide compositions are indicated and reported in Table 13). This intra-particle variation in composition may be a consequence of local differences in concentrations of oxygen or preferred crystal orientations, in which ions in certain orientations diffuse and react more readily than others. The direction in which the composition of the *mss* changes during oxidation has to be *from* the $Fe_{1-x}S$ (pyrrhotite) end-member *towards* the NiS (millerite) end-member: implicit in this oxidation is the removal and oxidation of iron (*cf*. Chapter 3; Xia *et al*. 2012). This reaction involves the removal of iron, but not necessarily that of sulphur:

$$Fe_{x_i}Ni_{9y_i/8}S + {}^{2x}\!/_{3}O_2 = Fe_{x_i-x}Ni_{9y_i/8}S + {}^{x}\!/_{3}Fe_3O_4 \qquad [16]$$

Here x decreases progressively from x_i to 0 (*i.e.*, $x_i \geq x \geq 0$). (Equation 16 is balanced with iron oxide appearing as Fe_3O_4 [magnetite]. The equation can just as readily be balanced for Fe_2O_3 [hematite].)

The third reaction was the loss of sulphur from the highly iron depleted *mss.* As the composition of the *mss* approached the Ni-S join (Figure 31; the compositions are denoted by triangular markers), there was a slight loss in sulphur.

The evidence for the third reaction in the sequence is tentative. Before the *mss* was entirely depleted in iron—that is, before it reached the NiS end-member—it appeared that a heazlewoodite solid solution ($[Ni,Fe]_{3\pm x}S_2$) became stable. The reaction remained tentative on the empirical evidence: (1) the pattern for heazlewoodite (Ni_3S_2) could not be matched, conclusively to the X-ray diffractograms of any of the roasted samples, yet (2) the composition of the base metal sulphide plots in the two-phase field between the *mss* and heazlewoodite(ss) (Figure 31). If the phase diagram correctly predicts the formation of a heazlewoodite(ss), then its absence in the diffractograms implies that it is too finely disseminated in the *mss* to be detected by SEM and present in insufficient quantities or as an amorphous phase and could therefore not be detected by XRD. A phase boundary between *mss* and heazlewoodite(ss) could not be discerned under SEM. Zamalloa (1996), however, did detect this boundary. In contrast to the finding of this study, (and those of Zamalloa [1996]); Xia *et al*. (2012) and Yu *et al.* (2012) found that the depletion of iron in the *mss* took the composition of the *mss* to its end-member, NiS. The reaction was followed by oxidation of NiS to NiO along with the oxidation Fe_3O_4 (magnetite) to Fe_2O_3 (hematite). The roasting of pentlandite in the current study was terminated before any NiO could form. NiO is an undesirable product for the purposes of this study.

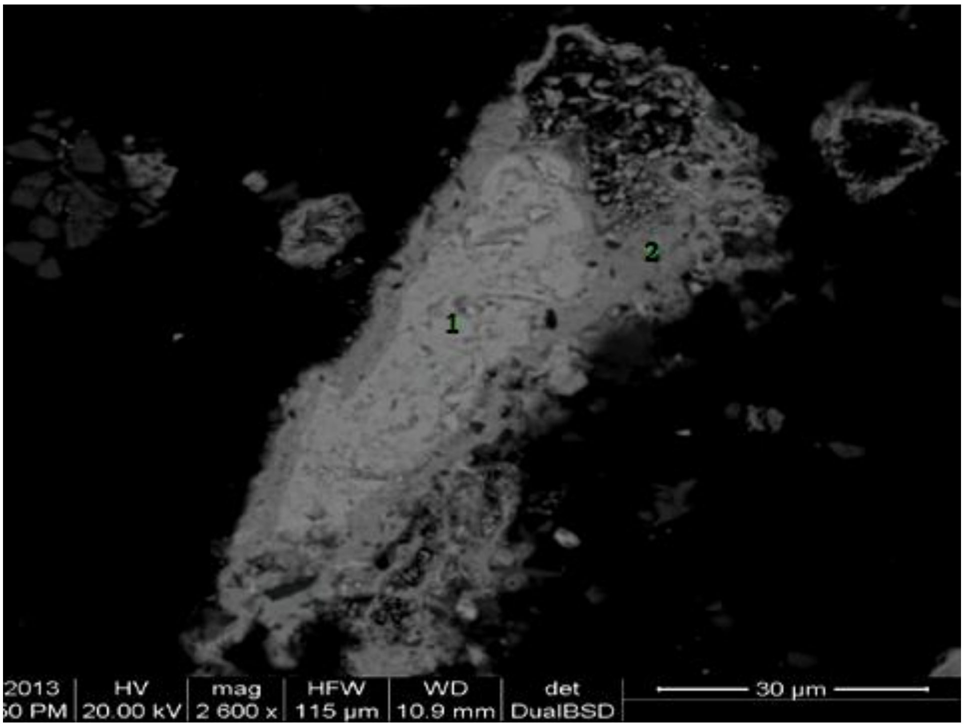

Figure 33: Backscattered-electron (BSE) image of a particle of *mss* and iron oxide after oxidation (formerly pentlandite).
(1) $Ni_{0.58}Fe_{0.32}S$; (2) Fe-oxide

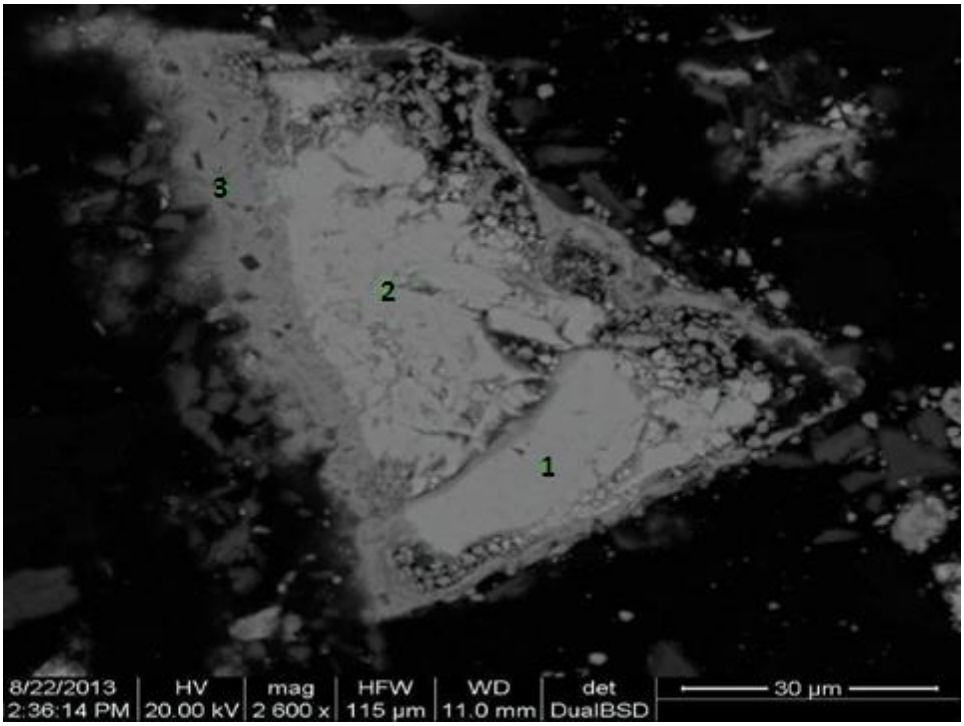

Figure 34: Backscattered-electron (BSE) image of a particle of *mss* and iron oxide after oxidation (formerly pentlandite).
(1) $Ni_{0.69}Fe_{0.18}S$; (2) $Ni_{0.78}Fe_{0.12}S$; (3) Fe-oxide

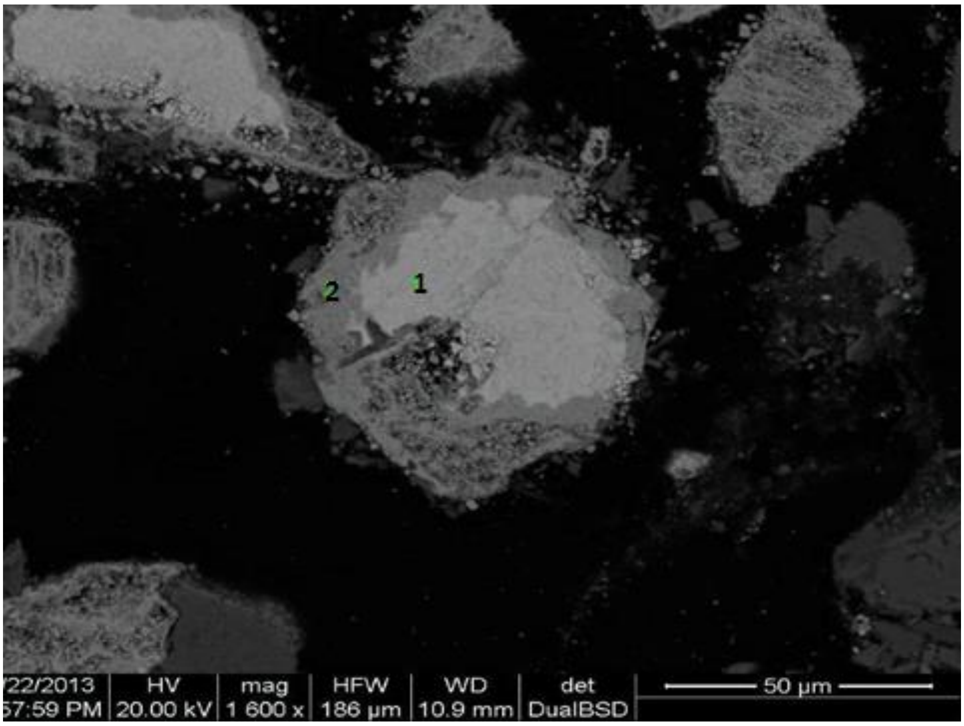

Figure 35: Backscattered-electron (BSE) image of a particle of *mss* and iron oxide after oxidation (formerly pentlandite).
(1) $Ni_{0.70}Fe_{0.14}S$; (2) Fe-oxide

Reaction mechanism of chalcopyrite transformation

The empirical evidence of the current study points to a five reactions mechanism in the oxidation of chalcopyrite ($CuFeS_2$) to lower sulphides of copper, before CuO forms. This five reactions takes cognisance of mechanisms proposed in the literature. The first reaction is the structural change of chalcopyrite to an intermediate solid solution (abbreviated *iss;* also referred to as talnakhite[ss], [Cu,Fe]S). The evidence is twofold. Phase relations in the system Cu-Fe-S at high temperatures (400–600 °C) indicate that $CuFeS_2$ (chalcopyrite) is unstable above 557 °C (Craig and Scott 1974) and the *iss* is stable at elevated to high temperatures (<960 ⁰C, Kullerud *et al*.1986; Figure 36). The empirical evidence of kinetic studies, on the other hand, is less certain. The major reflections in XRD for a talnakhite(ss) coincide with those for chalcopyrite. Of the analyses by SEM-EDS in this study (Table 14) only two of the compositions lie in the vicinity of the *iss* stability field (Figure 36). If an *iss* were to form, then a second reaction might follow, one in which the phase becomes depleted in iron—a compositional change marked by a move towards the left (the iron-and sulphur-depleted end member of the *iss*) in Figure 36.

The third reaction in the oxidation sequence is the formation of bornite(ss) from either chalcopyrite or the *iss*. That is, for chalcopyrite—

$$5CuFeS_2 + 8\frac{2}{3}O_2 = Cu_5FeS_4 + {}^{4}\!/_{3}Fe_3O_4 + 6SO_2 \qquad [17]$$

In this study the structural change introduced an interface between the two phases, with chalcopyrite or the *iss* occupying a shrinking core and the bornite(ss) forming an annulus around it (Figure 37 to Figure 39).

In the fourth reaction, oxidation removes iron and sulphur from the bornite(ss):

$$Cu_5FeS_4 + \frac{2}{3}(2x + 3y)O_2 = Cu_5Fe_{1-x}S_{4-y} + {}^{x}\!/_{3}Fe_3O_4 + ySO_2 \qquad [18]$$

Here x increases from 0 to 1 and y increases from 0 to about 1.5. The iron-depleted end-member of the solid-solution series is either Cu_9S_5 (digenite) or Cu_2S (chalcocite). Further oxidation, as demonstrated in the current study, produced Cu_2O (Figure 44).

The evidence of SEM-EDS analysis points to differences in the relative rates of oxidation. Because particles of chalcopyrite and pentlandite contained phases identified at all stages of oxidation, it can be concluded that most of these reactions occurred simultaneously. Pyrrhotite was fully oxidized before the two BM sulphides. The inference was that the oxidation of pyrrhotite is the fastest. The oxidation of pentlandite was the slowest: whereas SEM-EDS identified oxides of Cu, no oxides of Ni were ever identified.

Table 14: EDS Analysis of the sulfide phases identified during chalcopyrite oxidation.

Analysis	1	2	1	2	1	2	1	1	1	1	1
Figure	37	37	38	38	39	39	40	41	42	43	44
Composition (mass %)											
S	25.7	34.9	36.4	26.6	32.4	26.2	25.2	23.3	22.0	20.5	0.1
Fe	11.6	31.3	31.1	10.9	23.8	11.3	2.6	3.2	2.9	1.5	3.9
Cu	62.8	33.8	32.5	62.5	43.8	62.5	72.2	73.4	75.2	78.1	84.1
O	–	–	–	–	–	–	–	–	–	–	11.9
Stoichiometry											
Phase	bn (ss)	iss	iss	bn (ss)	iss	bn (ss)	bn (ss)	bn (ss)	bn (ss)	bn (ss)	Cu_2O
S	4.00	1.00	1.00	4.12	1.00	4.00	4.00	4.00	4.00	4.00	0.01
Fe	1.04	0.52	0.49	0.97	0.42	0.99	0.24	0.32	0.30	0.16	0.09
Cu	4.94	0.49	0.45	4.88	0.68	4.81	5.77	6.35	6.90	7.70	1.78
O	--	--	--	--	--	--	--	--	--	--	1.00

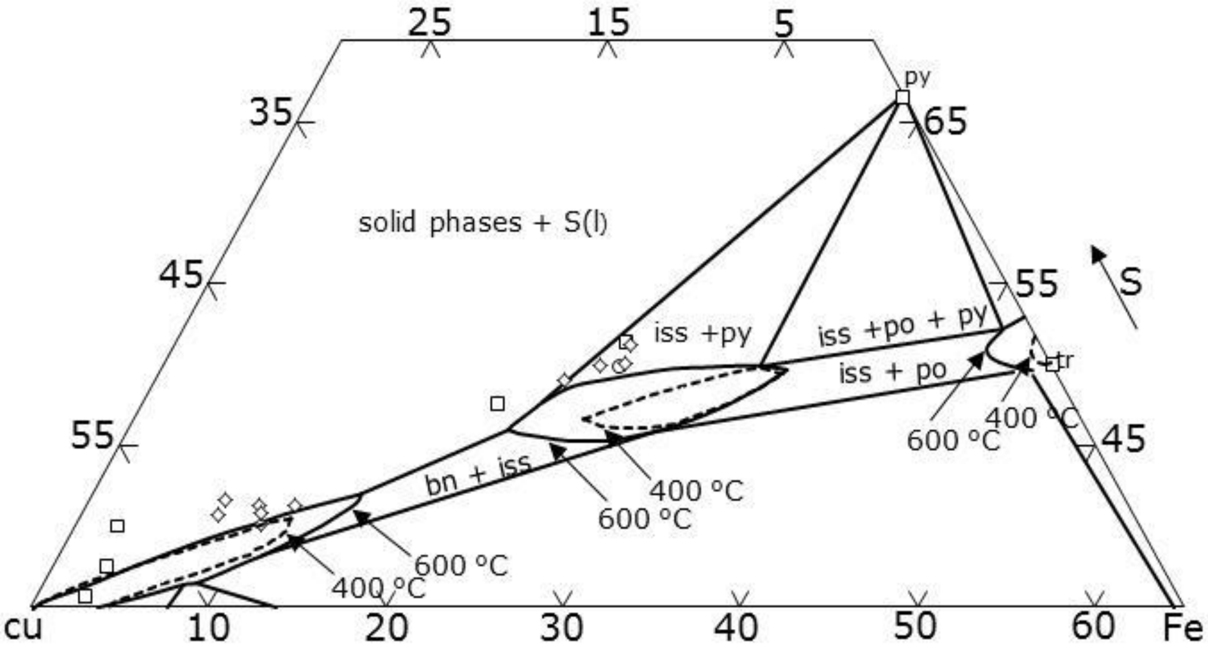

Figure 36: Measured compositions set against phase relations in the system Fe-Cu-S at 400 and 600 °C (see Chapter 3): the compositions of phases measured by SEM-EDS.

O - chalcopyrite; ◊ - compositions of calcines at 550 °C, □ – compositions of calcines at 650 °C. No liquid sulfur was formed in this study.

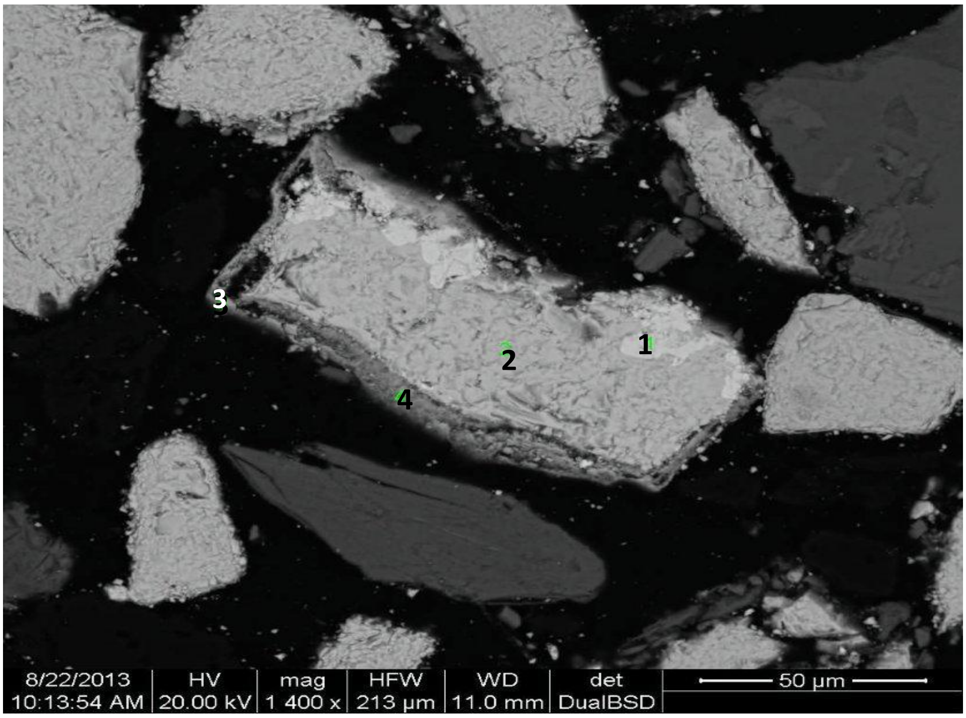

Figure 37: Backscattered-electron (BSE) image of bornite(ss) and Fe-oxide forming around a chalcopyrite core.
(1) $Cu_{4.94}Fe_{1.04}S_4$; (2) $Cu_{0.45}Fe_{0.52}S$; 3 and 4 – Fe-oxides

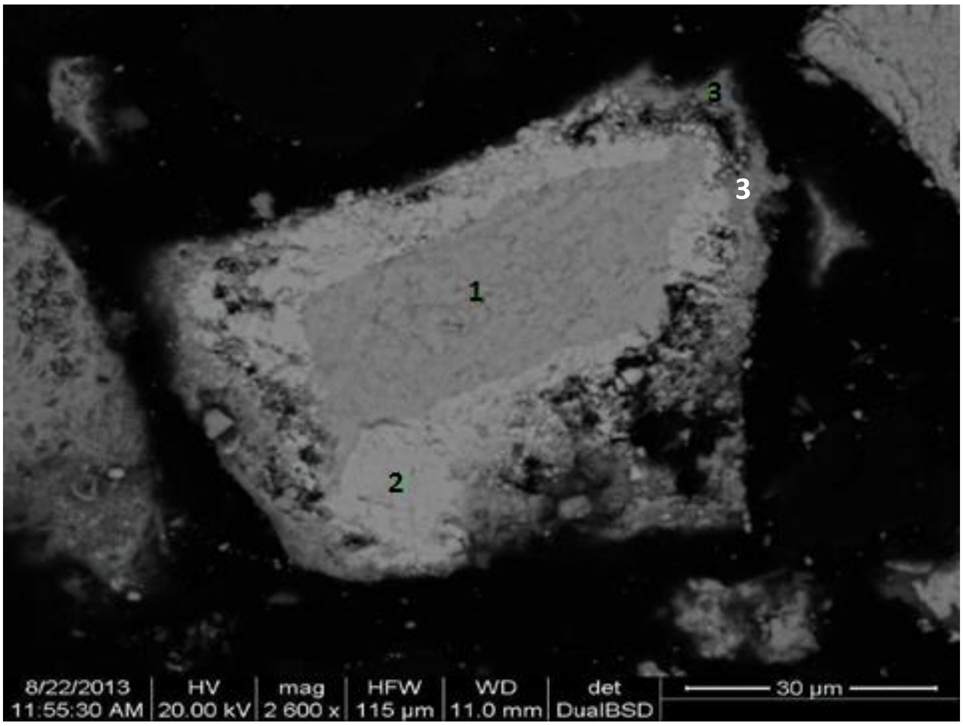

Figure 38: Backscattered-electron (BSE) image of bornite(ss) around a core of chalcopyrite.
(1) $Cu_{0.45}Fe_{0.49}S$; (2) $Cu_{4.88}Fe_{0.97}S_{4.12}$; (3) Fe-oxide

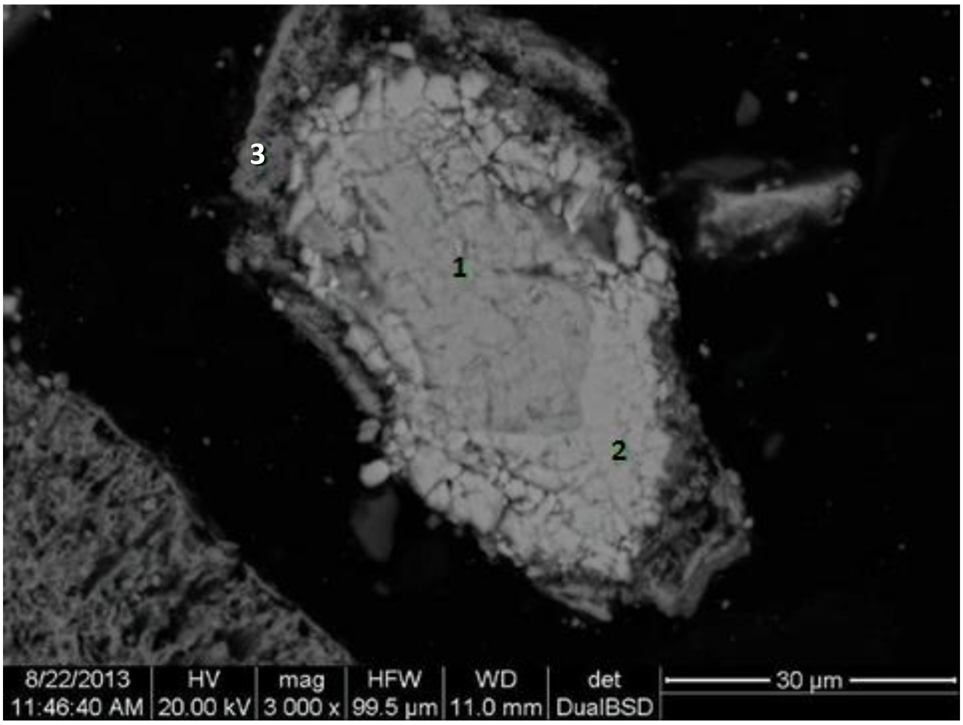

Figure 39: Backscattered-electron (BSE) image of bornite(ss) around a core of chalcopyrite.
(1) $Cu_{0.68}Fe_{0.42}S$; (2) $Cu_{4.81}Fe_{0.99}S_4$; (3) Fe-oxide

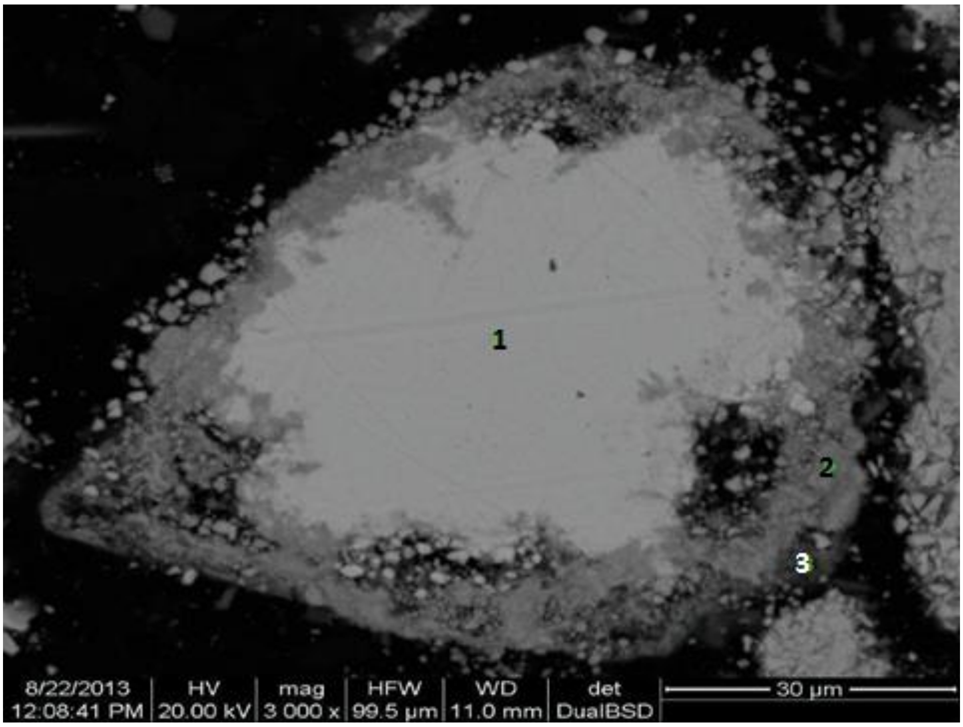

Figure 40: Backscattered-electron (BSE) image of bornite(ss) occupying a core that was formerly chalcopyrite.
(1) $Cu_{5.77}Fe_{0..24}S_4$; (2) Fe oxide; (3) Fe oxide

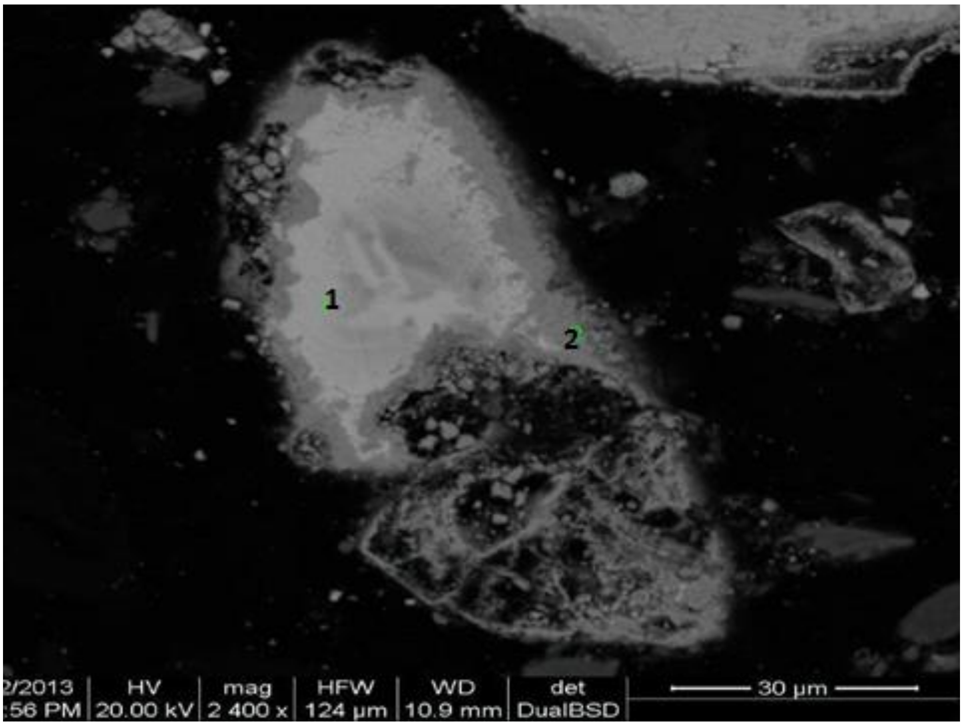

Figure 41: Backscattered-electron (BSE) image of bornite(ss) occupying a core that was formerly chalcopyrite.
(1) $Cu_{5.77}Fe_{0..24}S_4$; (2) Fe-oxide

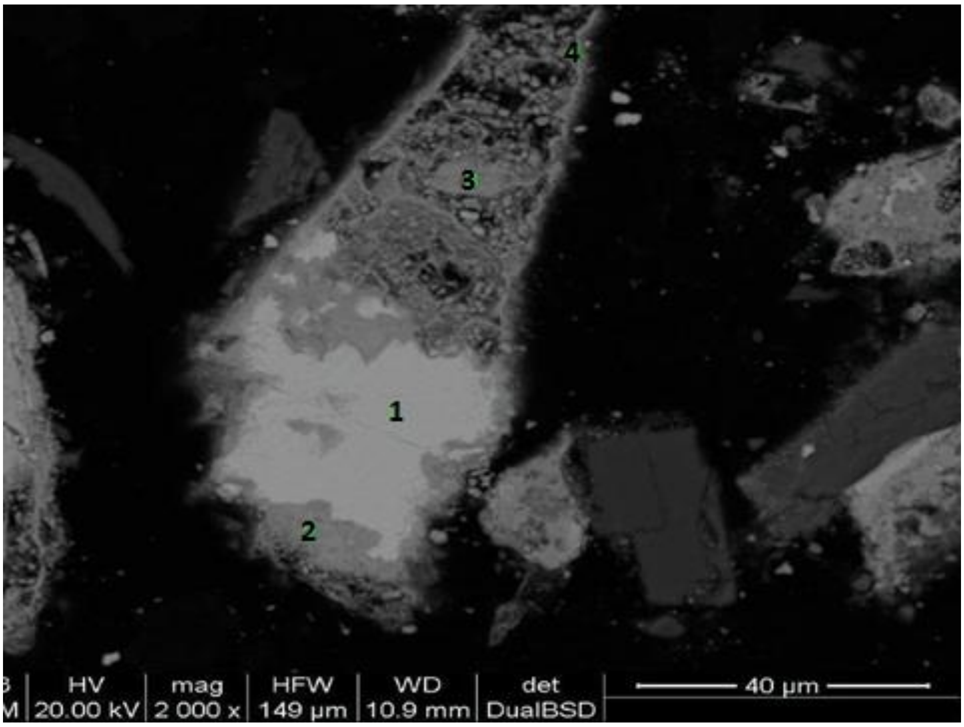

Figure 42: Backscattered-electron (BSE) image of bornite(ss) occupying a core that was formerly chalcopyrite.
(1) $Cu_{6.90}Fe_{0.30}S_4$; 2 , 3 and 4 are iron oxides.

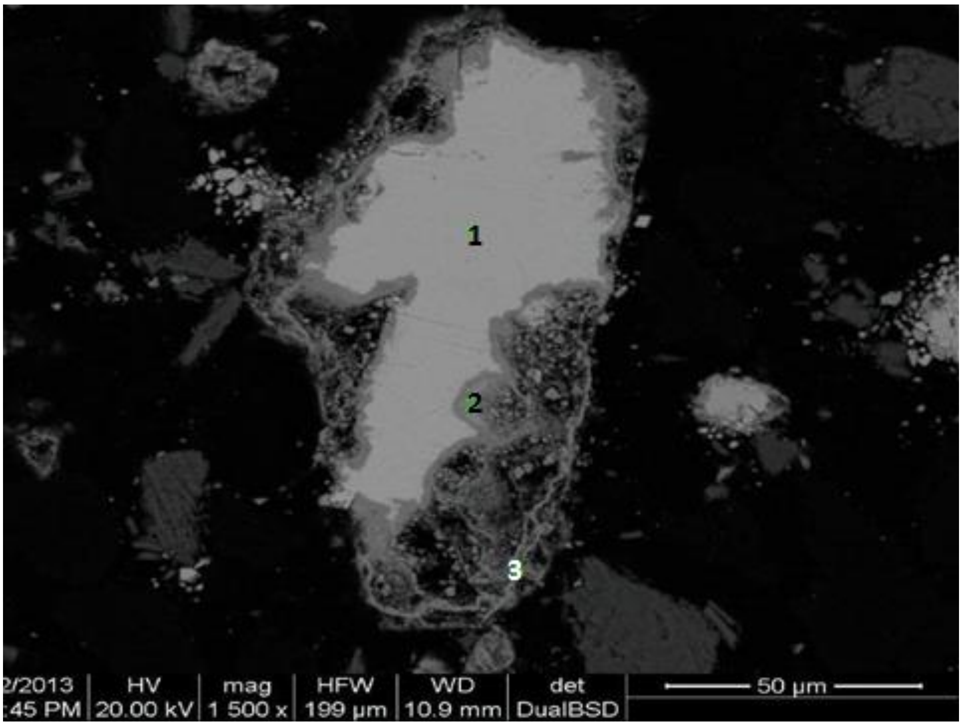

Figure 43: Backscattered-electron (BSE) image of bn(ss) particle with compositions that are highly iron depleted
(1) $Cu_{7.7}Fe_{0.16}S_4$; (2) and (3) Fe oxides

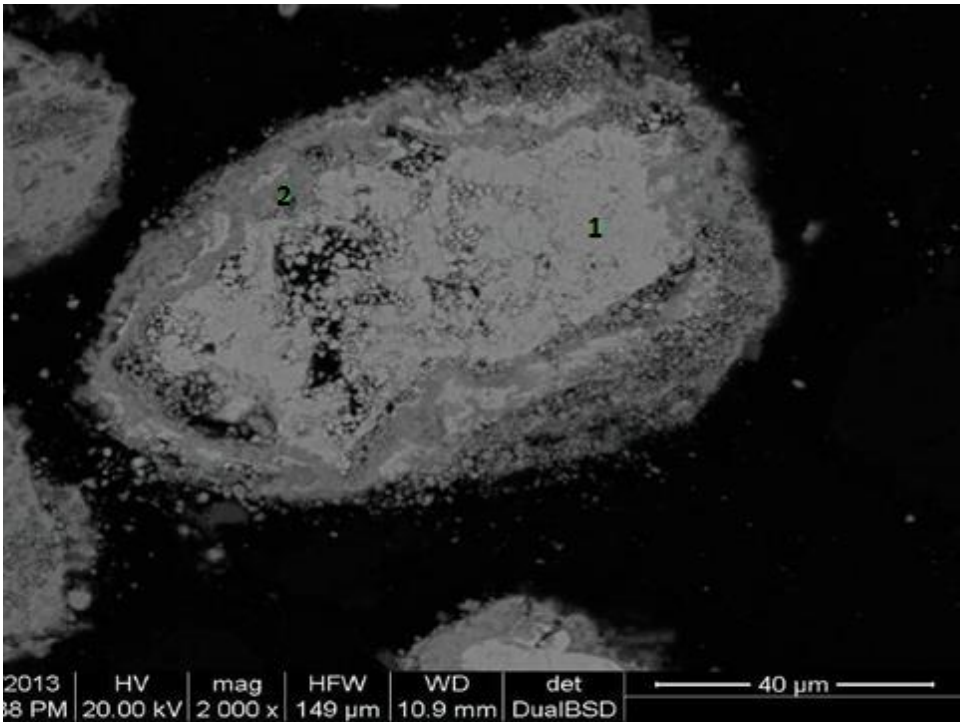

Figure 44: Backscattered-electron (BSE) image of a fully oxidised particle (formerly chalcopyrite).
(1) $Cu_{1.78}O$; (2) Fe-oxide

Chapter 7

Results—Efficacy and extent

The success of roasting is evaluated by two measures. They are (1) the extent removal of sulphur and (2) the extent of oxidation of iron, which would reports to the slag, preferably as Fe_2O_3 (hematite) and not Fe_3O_4 (magnetite). Related to the first measure is the retention of sulphur in the form of sulphates, which is an undesirable outcome. The success of roasting can also be evaluated with reference to smelting, which is the fate of all PGM concentrates, roasted or unroasted. By smelting the product from roasting trials, one can assess the efficacy of roasting. This outcome is measured in (1) matte fall, (2) the deportment of base metals to matte, and (3) the deportment of PGEs to matte. This chapter discusses the outcomes and measures.

7.1 The absence of sulphates

Roasting, as mentioned, serves to drive off sulphur. The formation of sulphates negates this goal by retaining sulphur. To make matters worse oxygen is trapped (chemically bonded in the concentrate). The formation of sulphates undermines roasting in three ways: (1) sulphates reduce the efficacy of roasting, in that energy expended without removing sulphur; (2) the sulphates would decompose in the furnace, which does not mitigate SO_2 emissions in this unit operation; and (3) there is a risk that the oxygen trapped in sulphates may form undesirable oxides (such of nickel and copper).

Studies reported in the literature describe the formation of metal sulphates (Chapter 4). Thermodynamic considerations govern stability of sulphates. Stability is dependent on the prevailing conditions, namely, temperature and pSO_2. Fixed beds, such as those used in thermobalances (thermogravimetry) and bench-scale furnaces that use boats or crucibles, promote high SO_2 partial pressures within the sample bed. These high SO_2 partial pressures stabilise metal sulphates (Chapter 4). Disturbing the bed, on the other hand, releases pockets of SO_2 in the bed. In the current study the work tube in the rotating-tube furnace was flushed with air: compressed air was regulated at the feed end and an extraction vent at the discharge end drew air into the work tube at this end. These controls maintained a high pO_2 and low PSO_2, sulphates are unstable under these conditions, hence, no sulphates were observed in any of the RTF products. On the other hand roasting tests conducted in the thermobalance (Figure 45) and the angular reciprocating capsule (Figure 46) produced metal sulphates. In thermogravimetry this formation was indicated by a gain in mass. The sample started gaining mass from about 350°C. The gain in mass became significant between 400 °C and 620 °C. The rate of metal sulphate formation increased with temperature. At these temperatures under high SO_2 and O_2 partial pressures metal sulphates can be expected. At temperatures greater than 620 °C thermogravimentry recorded a loss in mass. This loss can be attributed to sulphate decomposition, as sulphates became thermodynamically unstable. The thermal decomposition of ferrous sulphate is 575 °C and that of copper sulphate is 625 °C (Kolta and Askar 1975; see also Chapter 4). These temperatures span the maximum in the TG curve. It is worth noting that not all sulphur in as sulphide was sulphated: the TG curve (Figure 45) indicates a mass gain of 14%, whereas if all of the sulphur in the sample (17.4 %) were sulphated the mass gain would be 34.7 %. It is likely that limitations in the mass transfer of oxygen into the bed were overrun by the rate at which the sample was being heated.

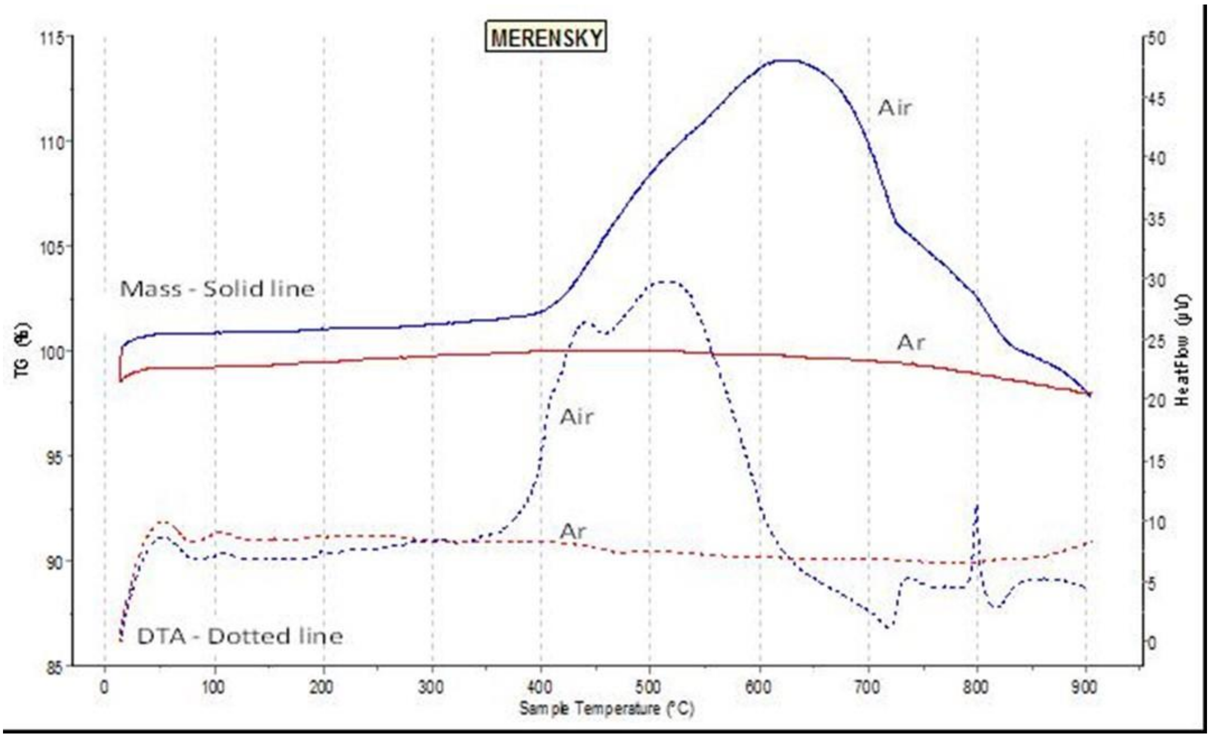

Figure 45: TG-DTA curves for oxidative roasting of Merensky concentrate.
(Sample mass 76 mg; heating rate 5 °C/min; atmosphere air and argon).

Sulphation also occurred during roasting in the angular reciprocating capsule. Here the charge was sealed in the capsule. The volume of the chamber remained constant. Pressure measurements (recorded from pressure gauge) taken during a test recorded an increase in pressure while the sample was being heated to temperature (Figure 46). This increase in pressure can be attributed to gas expansion (surface moisture effects likely to be negligible). After 15 minutes and for the rest of the test run, a steady decrease in pressure was recorded. The final pressure is lower than the starting pressure. The conclusion to be drawn from this observation is that oxygen reacted with sulphides and formed sulphates. In other words, oxygen is taken out of the gas phase and locked as sulphate in the solids.

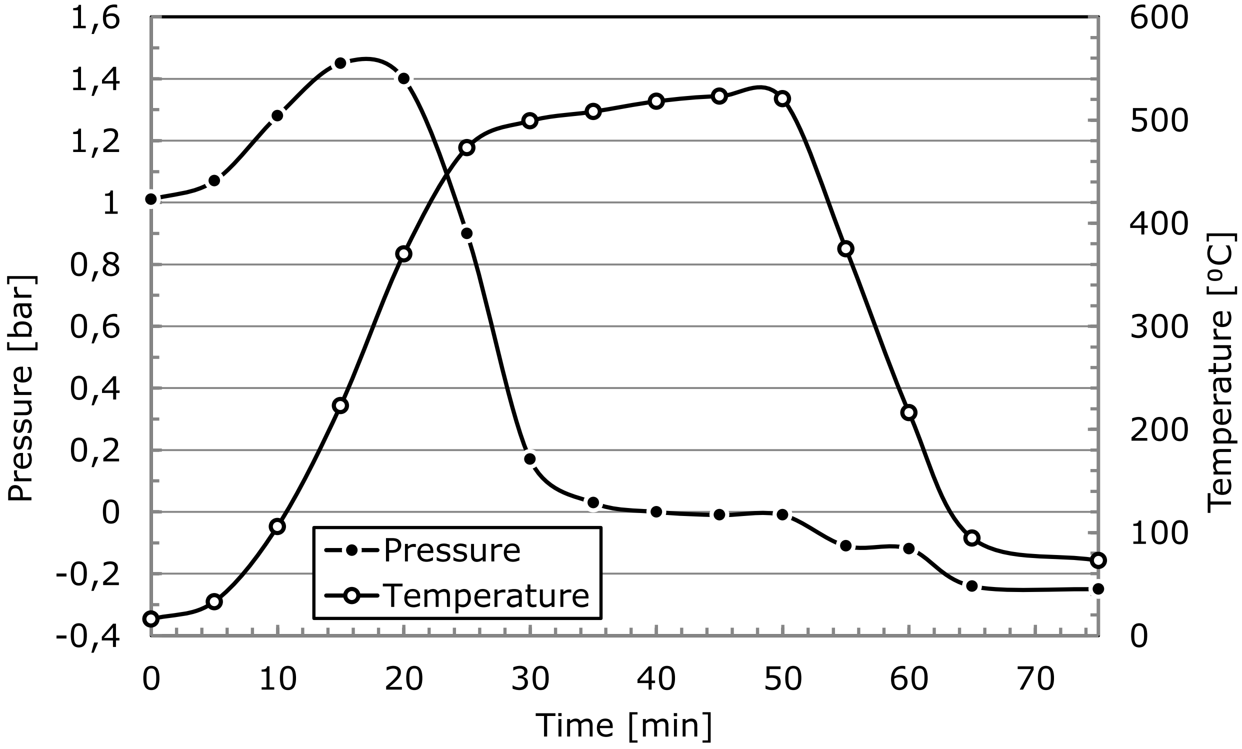

Figure 46: Temperature and pressure profiles during roasting of Merensky concentrate in the angular reciprocating capsule
(Tests conducted in an oxygen atmosphere for 1 hour, oxygen gauge pressure was 2 bar).

7.2 Sulphur removal and ferromagnetic content

Roasting oxidizes iron to one of its oxides, which in this instance could be either Fe_2O_3 or Fe_3O_4. Where possible magnetite formation should be avoided as iron-bearing spinels form a viscous intermediate layer between the matte and slag layers on smelting (Jones, 1999). This viscous layer results in increased levels of matte entrainment in, and PGM losses to, the slag. The build-up of Fe_3O_4, or other spinels, during smelting also reduces furnace capacity (Jones, 1999). Sulphur levels and magnetite contents of the roasted concentrate at different temperatures are given in Figure 47. The unroasted concentrate had a sulphur content of 17.4 %. During roasting some of the sulphur contained in the sulphide minerals reacted with oxygen to form SO_2, which was released into the freeboard. This release lowered the sulphur content in the concentrate (Figure 47). The degree of desulphurization increased with increasing temperature in as much as reactions were faster at higher temperatures and, for the same duration of oxidation (20 minutes), the samples progressed further along the desulphurization path. At 650 °C the sulphur content in the concentrate decreased to just over 5%, a 70 % reduction in sulphur content.

The magnetite content in the roasted concentrate (as measured by Satmagan) increased up to 400 ^{0}C. It increased from 1.7 % to approximately 5 %. Above 400 ^{0}C the percentage magnetite started to decrease; at 550 and 650 °C the magnetite content of the concentrate was 3.1 and 2.2%, respectively (Figure 47). At 550 °C the magnetite content almost doubled (1.7 to 3.1 %). The reasons for this observation are discussed in the reaction mechanism of pyrrhotite (Section 6.1—the discussion on the formation of a preferred intermediate form of iron oxide at the lower temperature).

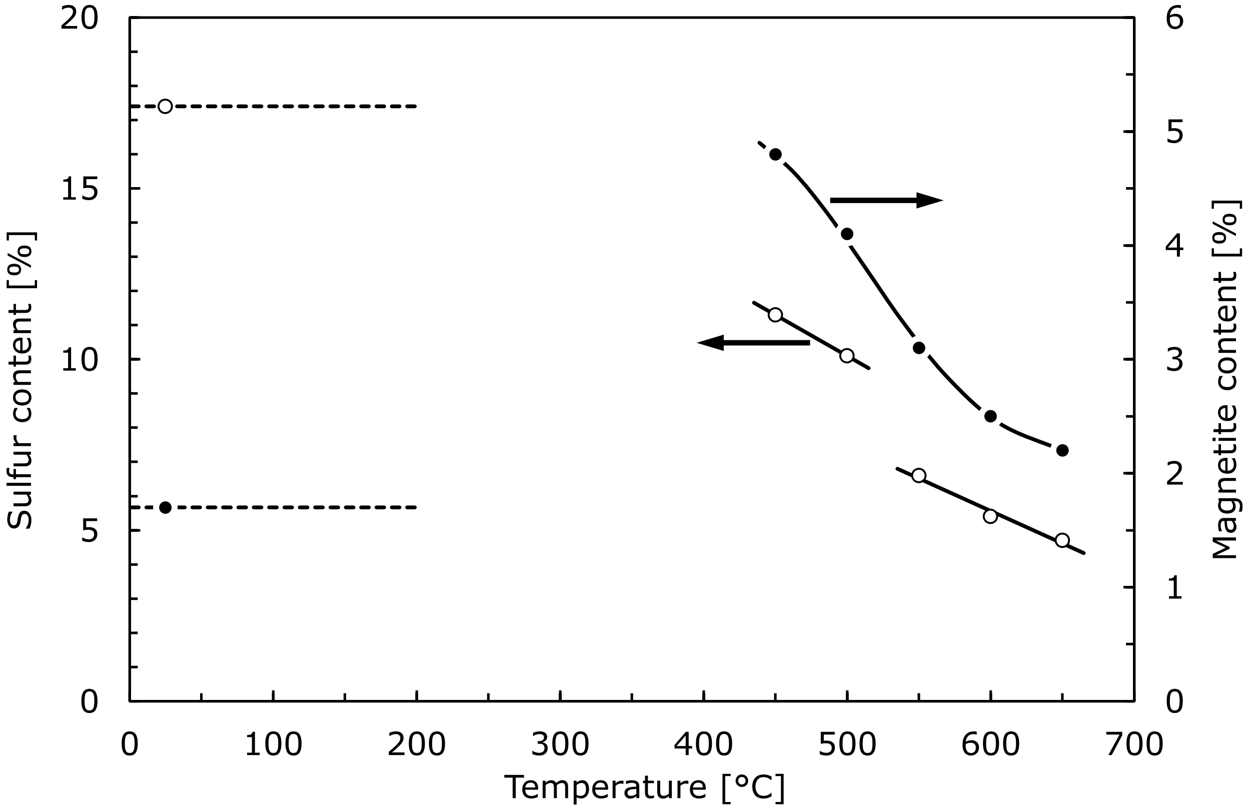

Figure 47: Sulphur and magnetite content in the concentrate as a function of roasting temperature.
(Roasting in air for 20 minutes)

7.3 Smelting

The products of roasting where smelted in order to determine how much matte would form and how much if any nickel and copper were lost to the slag. (The finely inter-mixed matte and slag prevented accurate measurement of PGEs in matte to establish the deportment of these elements to this phase.)

Observations with the naked eye and under a reflected light microscope indicated that matte collected in the smelting of fresh concentrate; matte associated with alloy collected in the smelting of concentrate roasted at 550 °C. Concentrate roasted at 650 °C, however, produced alloy. The phases were confirmed with SEM-EDS. In all three tests matte or alloy collected as fine beads or prills, which under gravity did not fall to the base of the crucible. These prills varied in size, ranging from only a few micrometres to several millimetres in diameter. The largest prill observed (5 mm) was for the concentrate roasted at 550 °C. The prills of matte or alloy remained within slag. Dispersed matte hindered the direct measurement of matte fall. The amount of matte could not be quantified. This variable was estimated therefore by balancing species in concentrate and matte compositions within the framework of a mass balance. The sum of squared differences was minimized. In this way the matte fall for the unroasted concentrate was estimated at 45 % and for the concentrate roasted at 550 °C at 15 %. These values are lower than matte falls calculated from stoichiometry—in other words, all sulfides reporting to matte are 52 % for the unroasted concentrate, 21 % for the concentrate roasted at 550 °C, and 17.6 % for the concentrate roasted at 650 °C.

Slag formation

The slag formed from both roasted concentrates was corrosive: it attacked the alumina crucible. The attack was at its most severe with the slag from concentrate roasted at 650 °C and at its least severe with the unroasted concentrate. The difference in the observed slag-crucible interactions was due to the differences in the compositions of the slags that formed during smelting of the roasted and unroasted concentrate.

Smelting of unroasted concentrate

SEM-EDS analyses of matte and slag phases produced from unroasted concentrate are presented in Table 15 to Table 17. Phases from which these analyses were obtained are shown in Figure 48 to Figure 50. The matte had high levels of iron (> 35 %) and two types of sulphides phases—one phase was iron rich and contained low percentages of nickel (Figure 48, analysis 1), whereas the other phase collected both copper and nickel with a relatively high iron content (Figure 48, analyses 2 and 3). These phases had variable compositions throughout the sample. Chromium, as a spinel ($Fe^{2+}_{0.8}Cr_{2.2}O_4$), was associated with some of the matte prills (Figure 51 , analysis 2)[4]. Also present in some instances was a platinum-containing alloy phase (Figure 49, analysis 1). The Cr-bearing spinel in matte makes the matte unsuitable for furnace recycling (Nell, 2004).

The slag contained very little iron—less than 10 % (Table 16). It also contained entrained matte (Figure 50, analysis 3). These entrained-matte particles would be lost to the slag and would contribute to the base-metal losses. Evidence of a Cr-bearing spinel in the slag phase (Figure 50, analysis 4) was also found.

Table 15: SEM-EDS analysis of matte produced from smelted unroasted concentrate.

Analysis	1	2	3	1
Figure	48	48	48	49
		Weight %		
S	37.6	34.47	31.55	
Fe	58.64	40.03	35.82	21.53
Ni	3.76	20.84	16.38	7.16
Cu		4.66	16.25	
Pt				71.31
Stoichiometry	$Fe_{0.9}Ni_{0.05}S$	$(Fe_{0.6}Ni_{0.3}Cu_{0.06})_9S_8$	(1)	

A phase assemblage of 1 - $Fe_{0.9}Ni_{0.05}S$ (pyrrhotite[ss]), 2 - $(Fe_{0.6}Ni_{0.3}Cu_{0.06})_9S_8$(pentlandite[ss]), and 3 - (1) Two phase assemblage Cu_9S_5 (digenite) in a matrix of pentlandite(ss) is postulated

Table 16: SEM-EDS analysis of slag produced from smelted unroasted concentrate.

Analysis	1	2	3	4
Figure	50	50	50	50
		Weight %		
Mg	30.78	5.62		10.51
Al	2.21	17.82		14.06
Si	16.41	21.7		20.66
Ca	1.53	20.15		17.32
Fe	5.07	6.06	60.16	7.12
O	43.99	28.66		30.33
Ni			6.21	
S			33.63	
Stoichiometry	$fosterite_{ss}$ (1)	(2)	$FeNi_{0.1}S$	(2)

(1) An olivine, $Mg_{1.9}Ca_{0.1}\,Fe_{0.1}Al_{0.1}Si_{0.9}O_4$
(2) An assemblage of two phases, Figure 50 shows two phases

---

[4] To avoid confusion, the numbering of figures is set by the sequence of references of figures in tables, not in text.

Table 17: SEM-EDS analysis of a particle that is a mixture of slag and matte, from smelted unroasted concentrate.

Analysis	1	2	3	4	5
Figure	51	51	51	51	51
			Weight %		
Mg			6.39		
Al			11.37		
Si			19.89		
Ca			21.27		
Fe	55.27	30.16	2.9	20.23	23.35
O		23.44	38.18	25.25	
Cr		46.41		54.52	
Ni	1.97				11.03
S	42.76				
Pt					65.62
Stoichiometry	$Fe_{0.74}Ni_{0.03}S$	Spinel (2)	(1)	Spinel (3)	–

(1) An assemblage of two phases (from image in Figure 51)
(2) This phase is a spinel, $Fe^{2+}_{1.0}Cr_{1.9}Fe^{3+}_{0.1}O_4$
(3) This phase is a spinel, $Fe^{2+}_{0.8}Cr_{2.2}O_4$

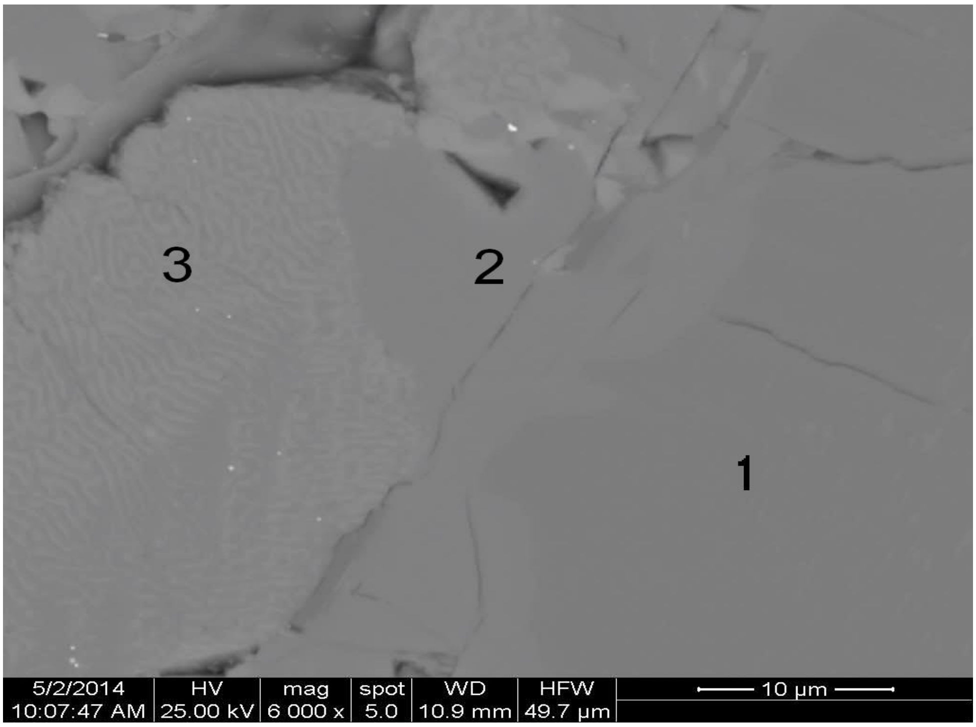

Figure 48: Backscattered electron (BSE) image of matte phases from unroasted concentrate.
(1) $Fe_{0.9}Ni_{0.05}S$ (pyrrhotite[ss]), (2) $[Fe_{0.6}Ni_{0.3}Cu_{0.06}]_9S_8$ (pentlandite[ss]), and (3) Cu_9S_5 (digenite) in a matrix of pentlandite(ss)

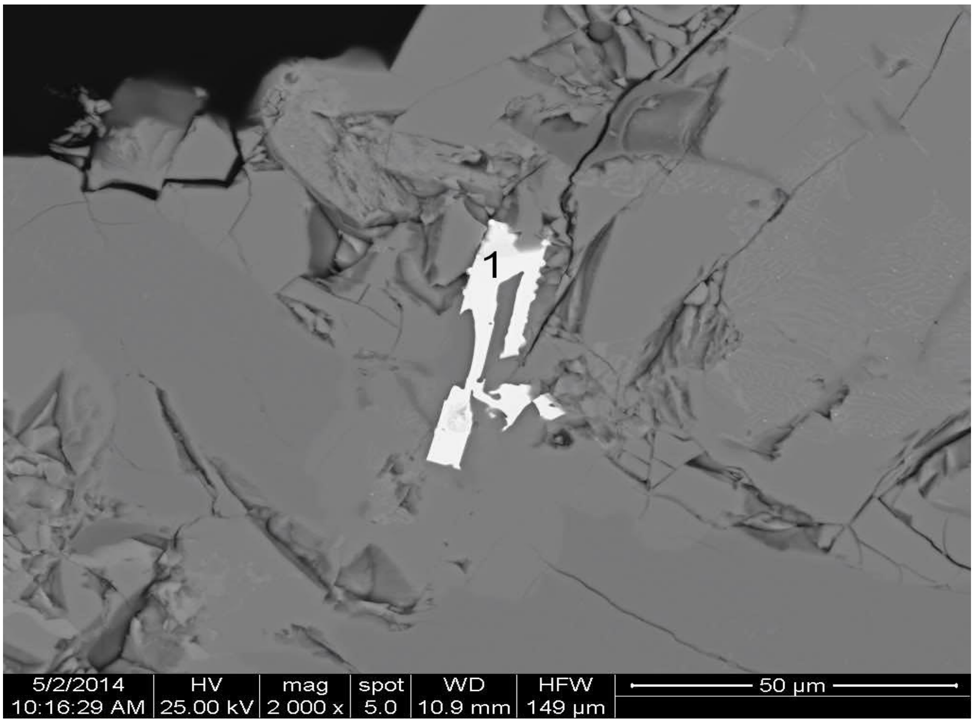

Figure 49: Backscattered electron (BSE) image of matte phase containing platinum bearing Fe-Ni alloy (1) $Ni_{0.3}Fe_{1.1}Pt$)
produced from unroasted concentrate

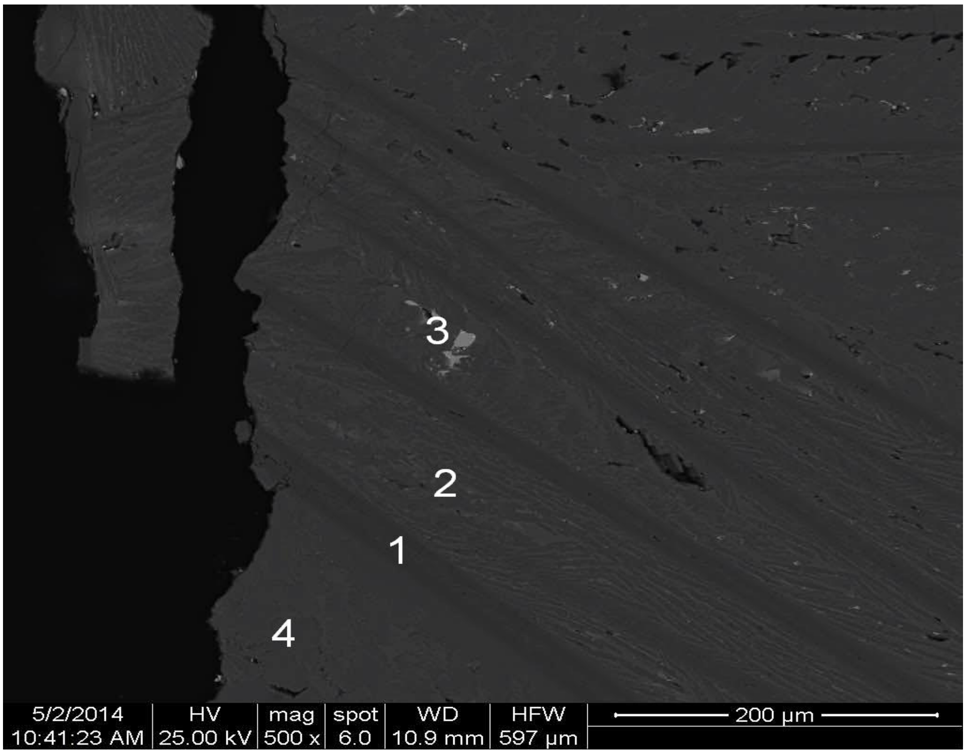

Figure 50: Backscattered electron (BSE) image of slag phases from unroasted concentrate.
(1) an olivine, $Mg_{1.9}Ca_{0.1}Fe_{0.1}Al0_{.1}Si_{0.9}O_4$; (2) assemblage of two phases; (3) $FeNi_{0.1}S$; (4) assemblage of two phases

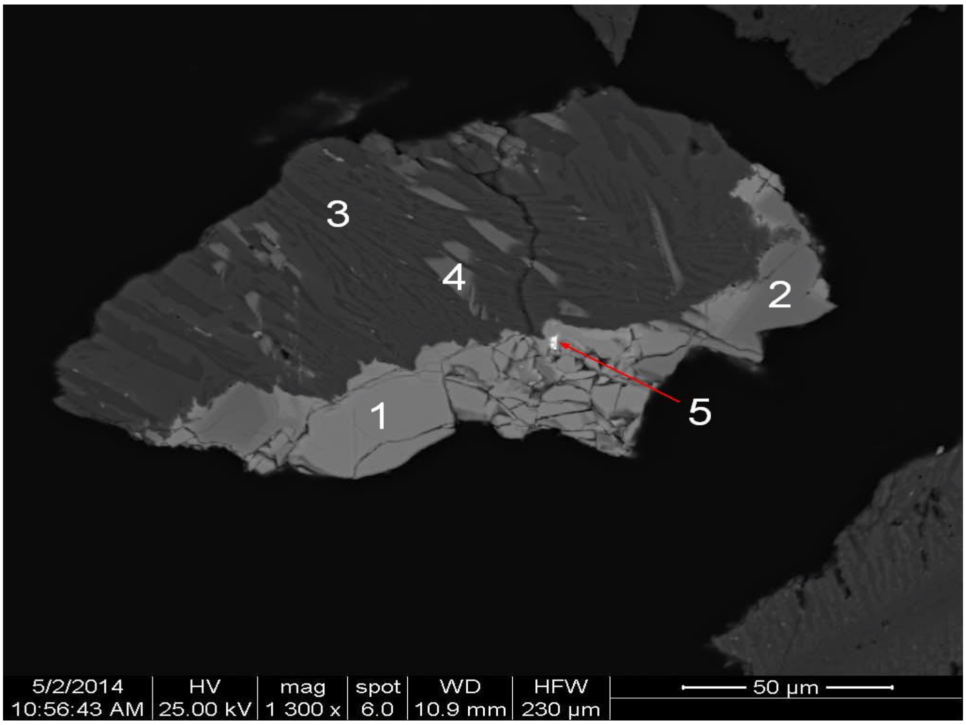

Figure 51: Backscattered electron (BSE) image of mixture of matte and slag from unroasted concentrate.
(1) $Fe_{0.74}Ni_{0.03}S$; (2) a spinel, $Fe^{2+}_{1.0}Cr_{1.9}Fe^{3+}_{0.1}O_4$; (3) assemblage of two phases; (4) a spinel, $Fe^{2+}_{0.8}Cr_{2.2}O_4$; (5) Alloy

Smelting concentrate roasted at 550 °C

Compositions of phases in matte and slag produced from concentrate roasted at 550 °C are listed in Table 18 toTable 21, and photomicrographs of textures are displayed in Figure 52 to Figure 56. Distinct prills of matte were disseminated throughout the smelted product. Their compositions varied: the proportions of sulphide phases varied from one prill to the next. The bulk matte composition also differed from that of matte produced in smelting unroasted concentrate. It did so in two respects. First, the matte contained less iron—less than 3.5 %, compared with greater than 35 % in matte from unroasted concentrate (the evidence is implicit in Table 18 and Table 19). Secondly, the assemblages of phases differ. In matte from roasted concentrate there were two distinct suites of phases. One of them comprised copper sulphides ranging from Cu_9S_5 (digenite) to $Cu_{1.97}S$ (djurleite) to Cu_2S (chalcocite) (*cf.* Figure 54, analysis 2; and Figure 52, analysis 2; Figure 54, analysis 3; Figure 55, dg); the other comprised heazlewoodite. Some of these phases contained a little iron. In some instances the copper sulphides also contained base metal alloys (*e.g.,* Figure 52, the rectangular area labelled "insert"). These alloys contained, variously, platinum and palladium (Figure 53, Table 18).

The slag comprised two phases. There was a fayalite matrix, the dominant phase (Figure 56; Table 20. “slag”; Table 21, analysis 3). The second, discontinuous phase was spinel. It had variable composition (Figure 55, Table 20, “sp”; Figure 56, Table 21, analyses 1 and 2). These spinels contained nickel. These phases accounted for the higher iron content in slag from roasted concentrate than slag from unroasted concentrate. There was no evidence of any dissolved copper in the phases of the slag, or any matte prills in the slag.

Table 18: SEM-EDS analyses of matte and alloy phases produced from concentrate that was roasted at 550 °C.

			Insert	
Analysis	1	2	1	2
Figure	52	52	53	53
		Weight %		
S	20.13	21.3		
Fe	0.83		1.96	2.36
Ni	68.31		62.03	70.68
Cu	10.73	78.7	25.99	26.16
Pt			10.01	
Pd				0.8
Stoichiometry	(1)	Cu_9S_5	–	–

(1) An assemblage of two phases: precipitated Cu sulphide in a matrix of heazlewoodite

Table 19: SEM-EDS analyses of matte and alloy phases produced from concentrate roasted at 550 °C

Analysis	1	2	3
Figure	54	54	54
		Weight %	
S		21.17	21.84
Fe	3.03	2.78	
Ni	36.38		
Cu	60.59	76.06	78.16
Stoichiometry	–	$Cu_{7.3}Fe_{0.3}S_4$	Cu_9S_5

Table 20: SEM-EDS analyses of matte and slag phases associated with a spinel phase, when concentrate roasted at 550 °C was smelted.

Analysis	Matte	Dg	Slag	Sp
Figure	55	55	55	55
		Weight %		
S	22.07	21.3		
Fe	0.64		14.98	60.23
Ni	29.6		1.43	8.72
Cu	47.7	78.7		
Mg			4.22	
Al			5.99	9.86
Si			19.07	
Ca			21.48	
O			32.84	21.19
Stoichiometry	(1)	Cu_9S_5	$Ca_{0.8}Mg_{0.3}Fe_{0.4}Al_{0.3}SiO_4$	$Fe_{0.72}Ni_{0.28}Al_{0.69}Fe_{1.31}O_4$

(1) An assemblage of two phases: disseminated Cu sulphide in a matrix of heazlewoodite

Table 21: SEM-EDS analyses of slag phases produced from concentrate roasted at 550 °C.

Analysis	1	2	3
Figure	56	56	56
		Weight %	
Mg	7.63	3.59	3.54
Al	29.63	17.88	7.38
Si		0.95	18.01
Ca			22.79
Fe	17.76	47.37	14.96
O	35.1	23.32	33.31
Ni	9.88	6.89	
Stoichiometry	$Mg_{0.50}Ni_{0.27}Fe_{0.24}Al_{1.74}Fe_{0.26}O_4$	$Mg_{0.25}Ni_{0.20}Fe_{0.55}Al_{1.12}Fe_{0.88}O_4$	$Ca_{0.85}Mg_{0.22}Fe_{0.40}Al_{0.41}Si_{0.96}O_4$

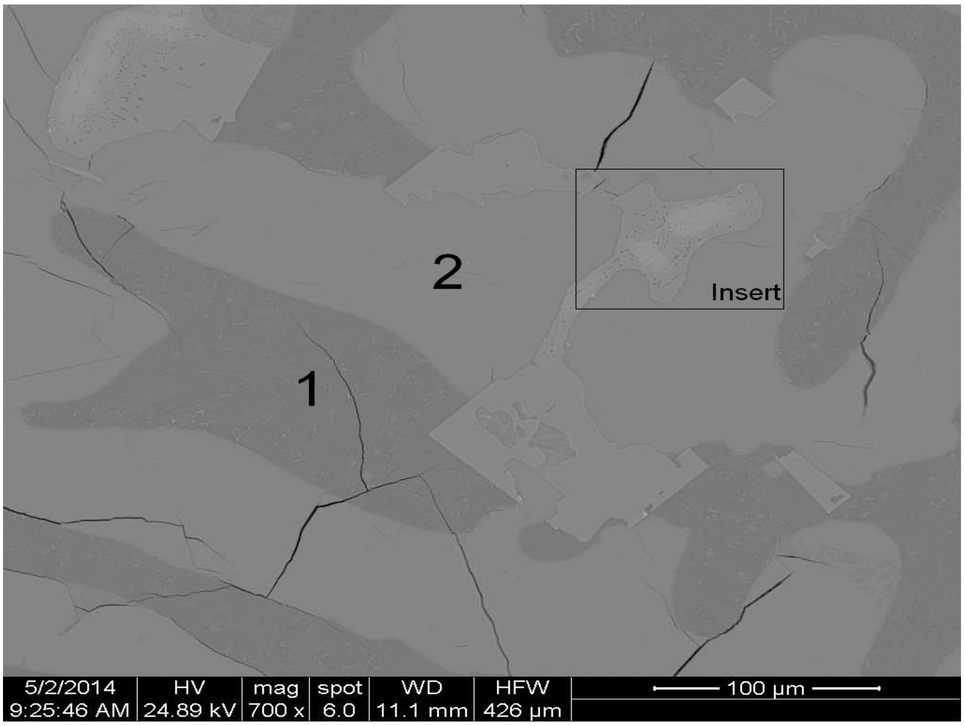

Figure 52: Backscattered electron (BSE) image of matte phases, produced from concentrate roasted at 550 °C.
(1) assemblage of two phases; (2) Cu_9S_5

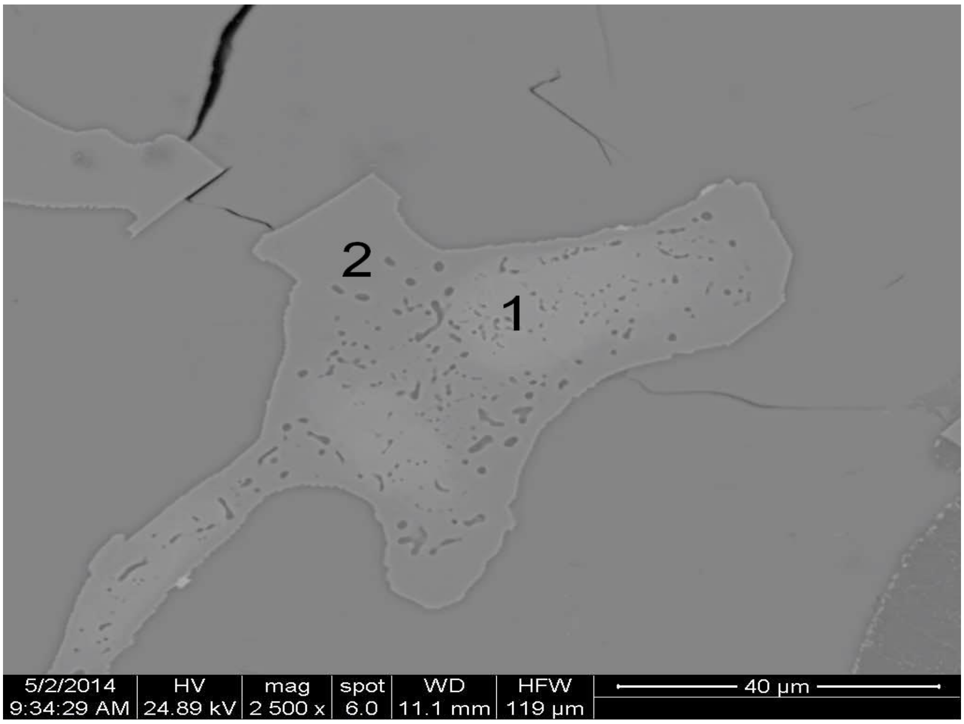

Figure 53: Magnification of the insert area in Figure 52.
(1) Pt containing alloy; (2) base metal alloy

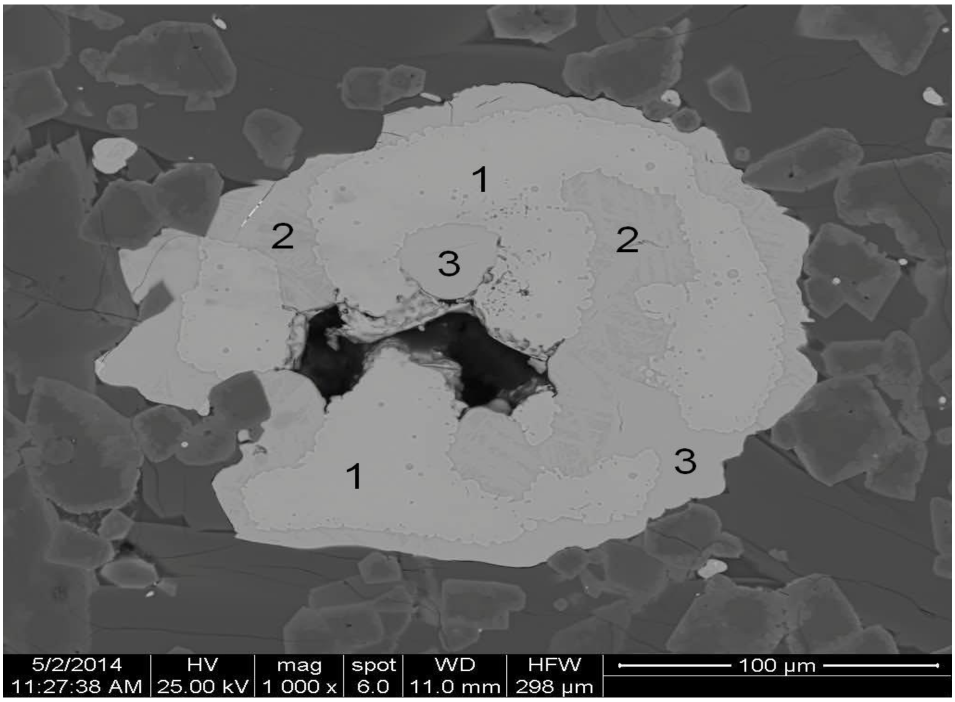

Figure 54: Backscattered electron (BSE) image of matte phases produced from concentrate roasted at 550 °C.
(1) base metal alloy; (2) $Cu_{7.3}Fe_{0.3}S_4$—from the texture it is presumably an assemblage of two phases with different compositions within the bornite(ss) series; (3) Cu_9S_5

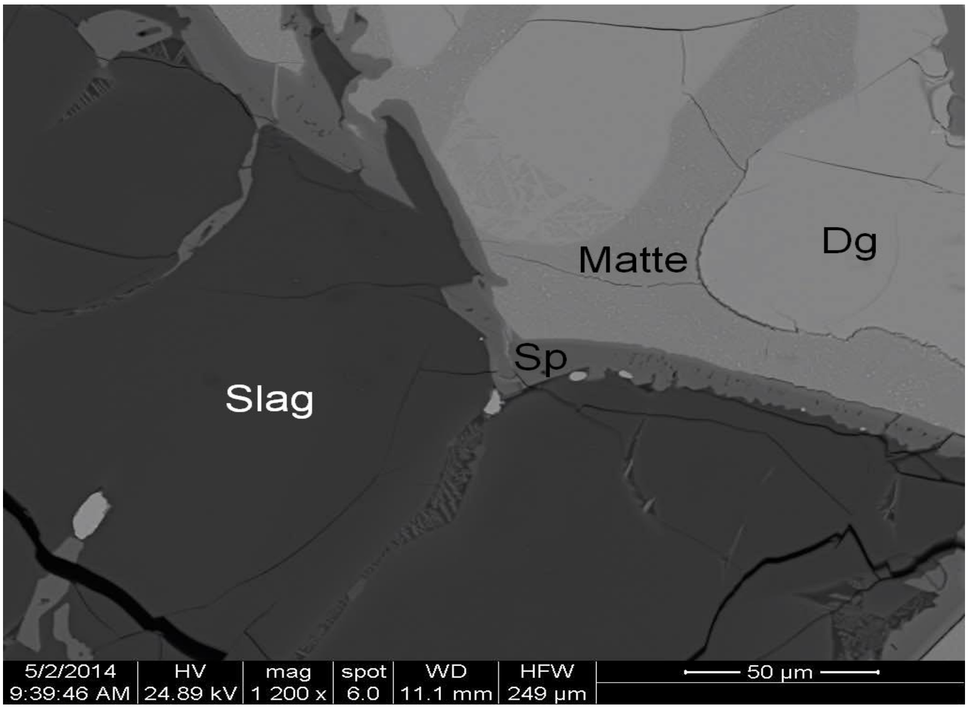

Figure 55: Backscattered electron (BSE) image of matte and slag phases that attached to a spinel phase when concentrate roasted at 550 °C was smelted. Slag– Olivine- $Ca_{0.8}Mg_{0.3}Fe_{0.4}Al_{0.3}SiO_4$; Matte– An assemblage of two phases [presumably digenite and a phase with composition in the bornite(ss)]; Sp– a spinel, $Fe^{2+}_{0.72}Ni_{0.28}Al_{0.69}Fe^{3+}_{1.31}O_4$; Dg– Cu_9S_5

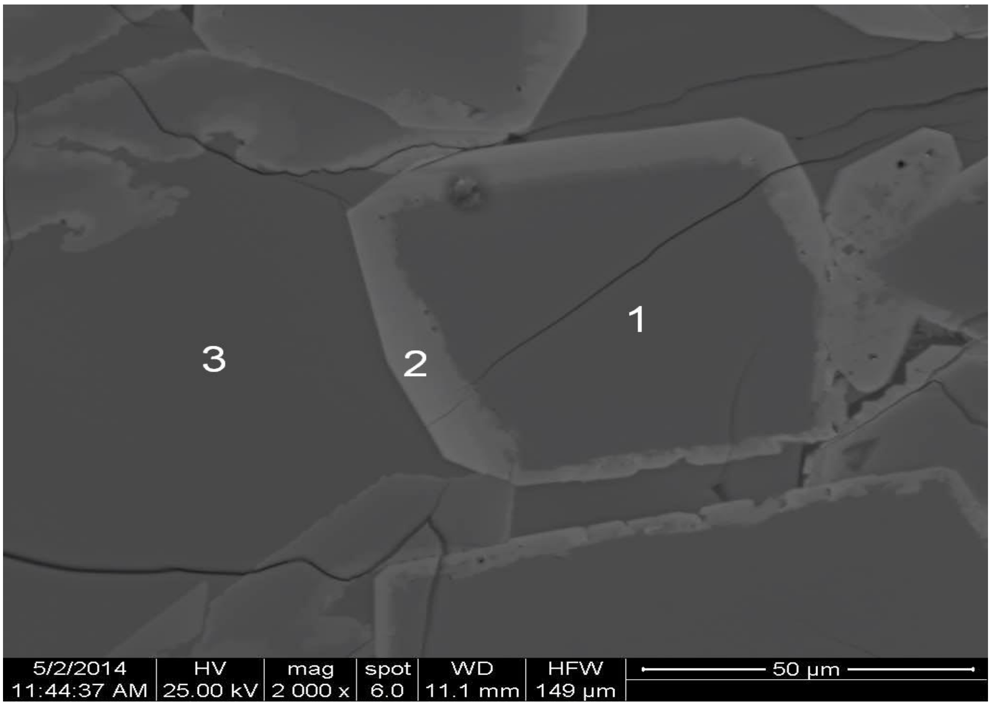

Figure 56: Backscattered electron (BSE) image of slag phases that were produced when concentrate roasted at 550 °C was smelted. (1) spinel, $Mg_{0.5}Ni_{0.27}Fe^{2+}_{0.24}Al_{1.74}Fe^{3+}_{0.26}O_4$; (2) spinel, $Mg_{0.25}Ni_{0.20}Fe^{2+}_{0.55}Al_{1.12}Fe^{3+}_{0.88}O_4$ and (3) olivine, $Ca_{0.85}Mg_{0.22}Fe_{0.40}Al_{0.41}Si_{0.96}O_4$

Smelting concentrate roasted at 650 °C

The products of smelting concentrate roasted at 650 °C were slag and alloy—not matte. The compositions of the phases in these products are listed in Table 22; textures appear in Figure 57 and Figure 58. The alloy particles did not separate from the slag, but remained entrained in it. The alloy was copper with small amounts of nickel and iron (Figure 58, analysis 1). Its composition was uniform throughout the sample. The slag comprised two types of phases, a silicate and a spinel. The composition of the spinel varied (Table 22, analyses 2 to 4), as did that of the silicate (Table 22, analyses 5 and 6). As in slag from concentrate roasted at 550 °C, the iron in the slag was considerably higher than that in slag from unroasted concentrate.

Table 2 lists enstatie ($Mg_2Si_2O_6$) as making up ~30% of the concentrate. The "other" in that same table denotes, principally, iron-bearing silicates. The system Mg-Fe-Si-O, therefore, would be a good approximation.

On the assumption, as a first pass, that the slag composition in the smelting of PGM concentrates can be represented (simplified) by the system Mg-Fe-Si-O. In Muan & Osborn (1964) that system is represented only in part—

- By the system $MgO-FeO-SiO_2$ (Figure F1, Appendix F)
- By the system $MgO-FeO{\bullet}Fe_2O_3-SiO_2$ (Figure F2, Appendix F)

The observation from both systems is that the isotherms of the liquidus surface lie roughly parallel to the $Mg_2Si_2O_6$ (enstatite)-Fe oxide join. That means that as the slag becomes richer in iron—as a consequence of the increasing oxidation and desulfurization of iron during roasting—there should be little change in the liquidus temperature of the slag. If anything, there might be a small drop in liquidus temperature with the addition of Fe_3O_4 (magnetite). As there is no published phase diagram for the system $MgO-Fe_2O_3-SiO_2$, we do not know what effect Fe^{3+}, without Fe^{2+}, has on the liquidus surface. The observed slag compositions are therefore consistent with what is predicated by these phase diagrams.

Table 22: SEM-EDS analyses of alloy and slag phases in smelted sample of concentrate roasted at 650 °C.

Analysis	1	2	3	4	5	6
Figure	58	58	58	58	58	58
			Weight %			
Fe	1.21	34.2	36.75	47.45	14.09	13.4
Ni	2.24	9.62	14.06	9.2	11.31	
Cu	96.56					
Mg		5.3	6.23	3.65	21.41	5
Al		5.31	19.9	14.12		6.37
Si				0.78	14.74	18.6
Ca				0.71	0.77	22.37
Cr		26.23	2.72			
O		19.34	20.36	24.09	37.68	34.25
Stoichiometry	—	$Mg_{0.39}Fe_{0.32}Ni_{0.29}Cr_{0.89}Fe_{0.76}Al_{0.35}O_4$	$Mg_{0.4}Ni_{0.4}Fe_{0.2}Al_{1.1}Fe_{0.8}O_4$	$Mg_{0.3}Ni_{0.3}Fe_{0.5}Al_{0.9}Fe_{1.0}O_4$	$Ca_{0.03}Mg_{1.41}Fe_{0..09}Ni_{0.31}Fe_{0.32}Si_{0.84}O_4$	(1) $Ca_{0.8}Mg_{0.3}Fe_{0.4}Al_{0.4}SiO_4$

(1) Presumably a single glassy phase, quenched before it crystalise

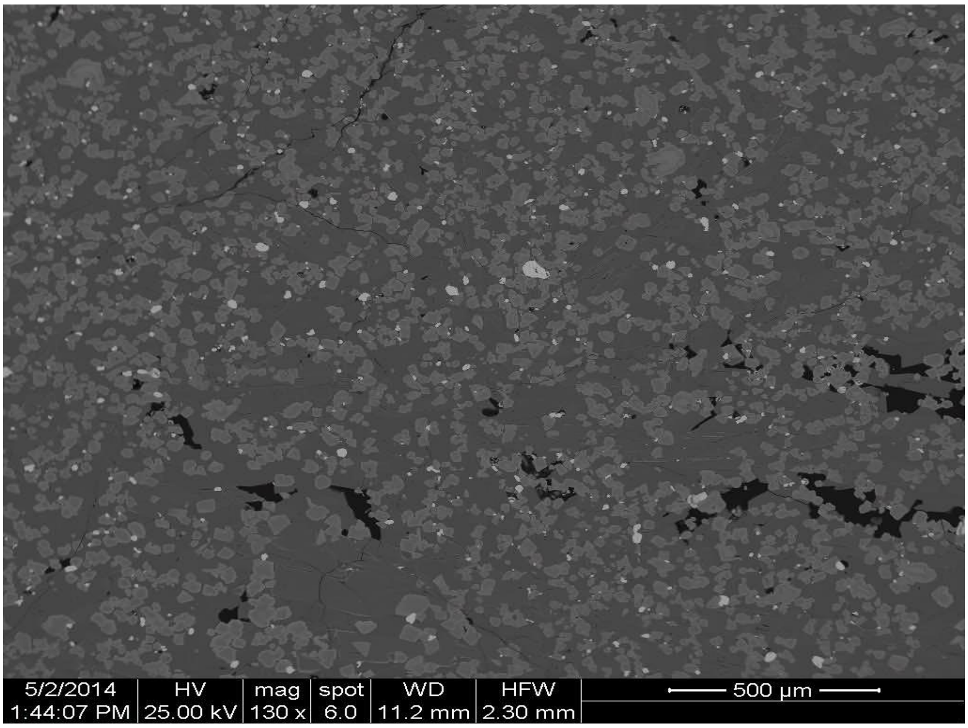

Figure 57: Backscattered electron (BSE) image of the microstructure of the smelted concentrate that was roasted at 650 °C.

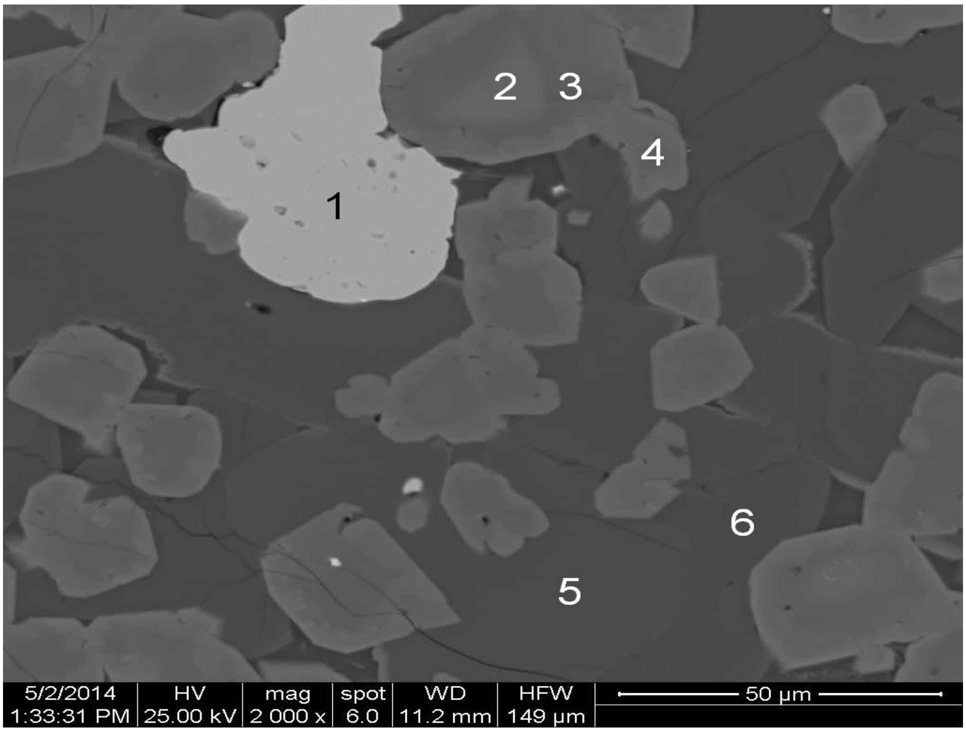

Figure 58: Backscattered electron (BSE) image of alloy and slag phases that formed when concentrate roasted at 650 °C was smelted.
(1) base metal alloy ; (2) a spinel, $Mg_{0.39}\ Fe^{2+}_{0.32}Ni_{0.29}Cr_{0.89}Fe^{3+}_{0.76}Al_{0.35}O_4$; (3) a spinel, $Mg0.4Ni0.4Fe^{2+}0.2Al_{1.1}Fe^{3+}0.8O4$; (4) a spinel, $Mg0.3Ni0.3Fe^{2+}0.5Al0.9Fe^{3+}1.0O4$; (5) a silicate, $Ca_{0.03}Mg_{1.41}Fe^{2+}_{0.09}Ni_{0.31}Fe^{3+}_{0.32}Si_{0.84}O_4$; (6) a silicate, Ca0.8Mg0.3Fe0.4Al0.4SiO4

Conclusions

The partial roasting of a PGM concentrate was investigated in this study. It was possible to roast a Merensky concentrate partially—that is, to oxidize only the iron in the sulphides and to leave nickel and copper in sulphide phases that, during smelting, can produce a matte. In this study roasting was accomplished in a rotating tube furnace (RTF) in air at 550 and 650 °C for about 20 minutes.

Roasting removed sulphur from the sulphides and oxidized iron. At 550 °C sulphur concentrations were lowered by at least 60 %, from 17.4 % to 6.5 %. At 650 °C, sulphur was reduced by 70%—from 17.4 % to 4.9% total sulphur. The formation of magnetite during roasting could not be avoided, but the concentration of magnetite formed decreased with increasing temperature. The magnetite content of calcine roasted at 550 °C was double that produced with unroasted concentrate. Furthermore, as long as the oxygen partial pressure in the kiln remained high (close to that of air), metal sulphates did not form.

All three sulphides (pyrrhotite, chalcopyrite and pentlandite) oxidized simultaneously, but their rates of oxidation differed. Pyrrhotite oxidized the fastest; pentlandite oxidized the slowest.

The following reactions mechanisms for the oxidation of iron sulphide (i.e., pyrrhotite [$Fe_{1-x}S$]) and base metal sulphides chalcopyrite ($CuFeS_2$) and pentlandite ($[Ni,Fe]_9S_8$) were postulated:

- Pyrrhotite reacts to form iron oxide. It appears that oxidation drives towards hematite, but magnetite is formed as an intermediate phase. Thus, at lower temperatures (<500 °C), the oxidation does not proceed much beyond magnetite, whereas at higher temperatures (500–650 °C) the proportion of hematite increases with respect to magnetite.
- The oxidation of chalcopyrite occurs in one of two ways. Neither SEM-EDS nor XRD could confirm which of these two mechanisms occurs. First, chalcopyrite undergoes a structural change to an intermediate solid solution (*iss*), followed by the oxidation of the formed *iss* according to a shrinking core model. An annulus of bornite(ss)

forms around the shrinking core of *iss*. The second possibility is that chalcopyrite simply oxidizes as a shrinking core, forming the bornite(ss) annulus around it. In both instances, once the particle fully transformed into bornite(ss) further oxidation follows the same sequence—that is, the bornite(ss) composition moves towards those that are iron deficient.

- Pentlandite loses iron first and is transformed into a monosulfide solid solution (*mss* phase). The second reaction is a compositional change: the composition of *mss* becomes progressively depleted in iron. In the third reaction the *mss* loses both iron and sulphur and forms heazlewoodite(ss).

The calcines from roasting were smelted to evaluate the effectiveness of roasting in the quality of matte and slag produced.

Smelting tests revealed that concentrates roasted at 550 °C for 20 min in the rotating tube furnace produced a greatly reduced the matte fall as was expected. The concentrations of iron in the matte were below 3.5 %. The sulphur content of matte was just above 20%, which is significantly lower than the >30% sulphur content for unroasted concentrate. Roasting also alters the chemistry of the slag that forms: the slag is more viscous and more corrosive towards alumina (in a crucible). Matte-slag separation was poor, however; a portion of the matte remained entrained in slag. Some phases in the slag contained dissolved nickel.

Concentrate that was roasted at 650 °C did not produce a matte during smelting. An alloy was formed instead, which in current industrial practice is an undesirable outcome for the furnaces, though not necessarily for the converter.

Recommendations

Although the roasting tests demonstrated that a partial roasting of PGM concentrate is possible, the smelting of roasted material may be problematic in that not only does the matte fall drop, but the slag properties change adversely—the slag viscosity rises and the slag becomes more corrosive towards alumina refractories. Although alumina refractories are not used in the primary smelter in contact with the slag, the slag may be corrosive to the refractories in use. To study the possible corrosive nature of slag on furnace refractory, smelting tests should be conducted using crucibles made from the refractory material used in the slag level of the primary smelter. The effects of roasting on smelting are that the slag becomes more viscous and the matte fall may be insufficient to collect all of the matte in a reasonable length of time. Two courses of action can be followed. In the first, tests must be conducted to optimize roasting. In order to find conditions (shorter times or lower temperatures) where the slag would be less viscous and the matte fall greater. The resulting calcines should have more sulphur and less oxidized iron, although magnetite concentrations are higher at lower temperatures. Alternatively, in a second course of action, it should be investigated whether calcines could be blended with unroasted concentrate. Depending on blending ratios, this option could have a negligible effect on the physical properties of the slag. Lastly investigate whether the use of a more slag corrosion resistant crucible–that is, one that allows for longer residence time, would assist in matte prills coalescence. The coalescence may assist in the matte collecting at the bottom of the crucible under gravity, this would allow for a more accurate measure of the matte fall.

References

ALLEN, T. 1990. *Particle Size Measurement*. Fourth edition. London: Chapman and Hall.

ANEESUDDIN, M., CHAR, P.N., HUSSAIN, M.R. and SAXENA, E.R., 1983. Studies on thermal oxidation of chalcopyrite from Chitradurga, Karnataka State, India. *Journal of Thermal Analysis,* 26(2), pp. 205-215.

ARNOLD, R.G., 1971. Evidence for liquid immiscibility in the system FeS-S. *Economic Geology,* 66(8), pp. 1121-1130.

BARTON JR., P.B., 1973. Solid solutions in the system Cu-Fe-S. Part i : the Cu-S and CuFe-S joins. *Economic Geology,* 68(4), pp. 455-465.

BRYNARD, N.J., DE VILLIERS, J.P.R. and VILJOEN, E.A., 1976. A Mineral Investigation of the Merensky Reef at the Western Platinum Mine, near Marikana, South Africa. *Economic Geology,* 71, pp. 1299-1307.

CABRI, J., 1989. Platinum-Group Elements: Mineralogy, Geology, Recovery. *The Canadian Institute of Mining and Metallurgy,* 23, pp. 57-63.

CABRI, L.J., 1973. New data on phase relations in the Cu-Fe-S system. *Economic Geology,* 68(4), pp. 443-454.

CAWTHORN, R.G. and WEBB, S.J., 2001. Connectivity between the western and eastern limbs of the Bushveld Complex. *Tectonophysics,* 330(3–4), pp. 195-209.

ĆIRKOVIĆ, M., 1999. *Theoretical and Experimental Study of the Process of Roasting Copper Sulphide Concentrates in the Reactor with Fluidizatio Layer using Oxygen-enriched Air*, University of Belgrade.

ĆIRKOVIĆ, M., ZIVKOVIĆ, D. and MITOVSKI, M., 2006. Mechanism of copper concentrate oxidation in fluidized bed reactor at temperatures betwen 600–720 °C, *Trends in development of machinery and associated technology* 2006, pp. 385-388.

COCIĆ, M.B., LOGAR, M.M., COCIĆ, S.L., DEVIC, S.S. and MANASIJEVIC, D.M., 2011. Transformation of chalcopyrite in the roasting process of copper concentrate in fluidized bed reactor. *JOM,* 63(5), pp. 55-59.

CRAIG, J.R. and SCOTT, S.D., 1974. Sulfide Phase Equilibria. In: P.H. RIBBE, ed, *Sulfide Mineralogy.* 1 edn.

CRAIG, J.R., NALDRETT, A.J. and KULLERUD, G., 1968. The Fe–Ni–S system: 400°C isothermal diagram. *Carnegie Institute Washington Year book,* 66, pp. 440-441.

DIAZ, C., CONRAD, B.R., MARCUSON, S.W. and BURGEES, K.I., 1994. Deep roasting of nickel concentrate. *CIM bulletin,* 87(981), pp. 72-78 a.

DIAZ, C., CONRAD, B.R., O'NEIL, C.E. and DALVI, A.D., 1994. Inco roast-reduction smelting of nickel concentrate. *CIM bulletin,* 87(981), pp. 62-71 b.

DUNN, J.G., 1997. The oxidation of sulphide minerals. *Thermochimica Acta,* 300(1-2), pp. 127-139.

DUNN, J.G. and JAYAWEERA, S.A.A., 1983. Effect of heating rate on the TG curve during the oxidation of nickel sulphide concentrates. *Thermochimica Acta,* 61(3), pp. 313-317.

DUNN, J.G. and KELLY, C.E., 1980. A TG/MS and DTA study of the oxidation of pentlandite. *Journal of Thermal Analysis,* 18(1), pp. 147-154.

DUNN, J.G. and KELLY, C.E., 1977. A TG/DTA/MS study of the oxidation of nickel sulphide. *Journal of Thermal Analysis,* 12(1), pp. 43-52.

ECCLESON, E. and WHITE, J., 2009. Development of roasting parameters for the ConRoast process with low sulphur feed stocks. SAIMM Platinum Conference, Platinum in Transformation. *SAIMM Platinum Conference, Platinum in Transformation, The South African Institute of Mining and Metallurgy,* pp. 65-69.

FLEET, M.E., 2006. *Phase equilibria at high temperatures.*

HAMMERSCHMIDT, J. 2008. The roasting of PGM-ore concentrates in a circulating fluidized bed. *Third International Platinum Conference, Platinum in Transformation*: pp 161–167. Johannesburg: SAIMM.

HUNDERMARK, R.J., MNCWANGO, S.B., DE VILLIERS, L.P.vS. and NELSON, L.R. 2011. The smelting operations of Anglo American's platinum business: An update. *In* Jones, R.T. and Den Hoed, P. (eds) *Southern African Pyrometallurgy 2011:* pp 295–307. Johannesburg: SAIMM.

JONES, R.T., 2002. Conroast: DC arc smelting of dead-roasted sulphide concentrates, STEPHENS R.L. and SOHN H.Y., eds. In: *Sulfide Smelting 2002*, 17 February 2002 through 21 February 2002 2002, pp. 435-456.

JONES, R.T., 1999. Platinum smelting in South Africa. *South African Journal of Science,* 95(11-12), pp. 525-534.

JONES, R.T. and GELDENHUYS, I.J., 2011. The pros and cons of reductive matte smelting for PGMs. *Minerals Engineering,* 24(6), pp. 495-498.

KENNEDY, T. and STURMAN, B.T., 1975. The oxidation of iron (II) Sulphide. *Journal of Thermal Analysis,* 8, pp. 329-337.

KNOWLTON, T.M., 2002. A review of catalytic fluidized-bed reactors in the chemical and petrochemical industries. A. LUCKOS and P. DEN HOED , eds. In: *IFSA 2002, Industrial Fludidization South Africa* 2002, Johannesburg: SAIMM, pp. 3-31.

KOLTA, G.A. and ASKAR, M.H., 1975. Thermal decomposition of some metal sulphates. *Thermochimica Acta,* 11(1), pp. 65-72.

KULLERUD, G. and YODER, H.S., 1959. Pyrite stability relations in the Fe-S system. *Economic Geology,* 54(4), pp. 533-572.

KULLERUD, G. and YUND, R.A., 1962. The Ni-S system and related minerals. *Journal of Petrology,* **3**(1), pp. 126-175.

LEVENSPIEL, O., 1972. *Chemical reaction engineering.* 2nd edn. New York: Wiley.

LIDDELL, K.S., MCRAE, L.B. and DUNNE, R.C., 1986. Process routes for the beneficiation of noble metals from Merensky and UG2 ores. *Mintek Review,* 4, pp. 33-44.

MACKEY, L.C., 1991. *The Ignition Properties of Pyrite, Pyrrhotite, Pentlandite and Violarite*, Curtin University of Technology.

MERWIN, H.E. and LOMBARD, R.H., 1937. The system, Cu-Fe-S. *Economic Geology,* 32(SUPPL. 2), pp. 203-284.

MISRA, K.C. and FLEET, M.E., 1974. Chemical composition and stabilty of violarite. *Economic Geology,* 69, pp. 391-403.

NELL, J., 2004. Melting of platinum group metal concentrates in South Africa. *Journal of The South African Institute of Mining and Metallurgy,* 104(7), pp. 423-428.

PANDHER, R., THOMAS, S., YU, D., BARATI, M. and UTIGARD, T., 2011. Sulfate formation and decomposition of nickel concentrates. *Metallurgical and Materials Transactions B: Process Metallurgy and Materials Processing Science,* 42(2), pp. 291-299.

PANDHER, R. and UTIGARD, T., 2010. Roasting of nickel concentrates. *Metallurgical and Materials Transactions B: Process Metallurgy and Materials Processing Science,* 41(4), pp. 780-789.

PRASAD, S. and PANDEY, B.D., 1999. Thermoanalytical studies on copper-iron sulphides. *Journal of Thermal Analysis and Calorimetry,* 58(3), pp. 625-637.

ROSEBOOM, E.H., 1966. An Investigation of the system Cu–S and some natural copper sulfide between 25 °C and 700 °C. *Economic Geology,* 61, pp. 641-672.

ROSENQVIST, T., 1978. Phase equilibria in the pyrometallurgy of sulfide ores. *Metallurgical Transactions B,* 9(3), pp. 337-351.

SOKIC, M., ILIC, I., ŽIVKOVIC, D. and VUCKOVIC, N., 2008. Investigation of mechanism and kinetics of chalcopyrite concentrate oxidation process. *Metalurgija,* 47(2), pp. 109-113.

ŠTRBAC, N., ŽIVKOVIC, D., MIHAJLOVIC, I., BOYANOV, B. and ŽIVKOVIC, Ž., 2008. Mechanism and kinetics of the oxidation of synthetic a-NiS. *Journal of the Serbian Chemical Society,* 73(2), pp. 211-219.

TANABE, T., KAWAGUCHI, K., ASAKI, Z. and KONDO, Y., 1987. OXIDATION KINETICS OF DENSE PENTLANDITE. *Transactions of the Japan Institute of Metals,* 28(12), pp. 977-985.

TANABE, T., KAWAGUCHI, K., ASAKI, Z. and KONDO, Y., 1986. OXIDATION KINETICS OF PENTLANDITE. *Nippon Kinzoku Gakkai-si,* 50(8), pp. 720-726. In Japanese

THETHWAYO, B.M., 2010. *Sulphidation of copper coolers in PGM smelters*, University of Pretoria, South Africa. MSc Thesis

THORNHILL, P.G. and PIDGEON, L.M., 1957. Micrographic study of sulfide roasting. *JOM,* 9B, pp. 989-995.

VAUGHAN, D.J. and CRAIG, J.R., 1978. *Mineral chemistry of metal sulfides.* Cambridge: Cambridge University Press.

VAUGHAN, D.J. and CRAIG, J.R., 1978. *Mineral chemistry of metal sulfides.* Cambridge: Cambridge University Press.

XIA, F., PRING, A. and BRUGGER, J., 2012. Understanding the mechanism and kinetics of pentlandite oxidation in extractive pyrometallurgy of nickel. *Minerals Engineering,* 27-28, pp. 11-19.

YU, D. and UTIGARD, T.A., 2012. TG/DTA study on the oxidation of nickel concentrate. *Thermochimica Acta,* 533, pp. 56-65.

YUND, R.A. and KULLERUD, G., 1966. Thermal stability of assemblages in the Cu-Fe-S system. *Journal of Petrology,* 7(3), pp. 454-488.

ZAMALLOA, M. and UTIGARD, T.A., 1996. The behaviour of Ni-Cu concentrate in an industrial fluid bed roaster. *Canadian Metallurgical Quarterly,* 35(5), pp. 435-449.

ZAMALLOA, M., UTIGARD, T.A. and LASTRA, R., 1995. Quantitative mineralogical characterization of roasted Ni-Cu concentrates. *Canadian Metallurgical Quarterly,* 34(4), pp. 293-301.

ZHENG XIAOHONG and CHEN XINMIN, 1983. KINETIC INVESTIGATION ON OXIDATION OF PENTLANDITE. *Yu Se Chin Shu/Nonferrous Metals,* 35(3), pp. 42-47.

ŽIVKOVIC, Ž., ŠTRBAC, N., ŽIVKOVIC, D., VELINOVSKI, V. and MIHAJLOVIC, I., 2005. Kinetic study and mechanism of chalcocite and covellite oxidation process. *Journal of Thermal Analysis and Calorimetry,* 79(3), pp. 715-720.

ŽIVKOVIC, Ž.D., MITEVSKA, N. and SAVOVIC, V., 1996. Kinetics and mechanism of the chalcopyrite - Pyrite concentrate oxidation process. *Thermochimica Acta,* 282-283(SPEC. ISS.), pp. 121-130.

Appendices

Appendix A: Additional test conditions, XRD and mineral-liberation results of fresh concentrate (Merensky concentrate)

.Table A 1 Analysis of Merensky concentrate. Rietveld refinement.:

	XRD
BMS	
Chalcopyrite ($CuFeS_2$)	11.2
Pentlandite ($[Fe,Ni]_9S_8$)	8.1
Pyrrhotite ($Fe_{1-x}S$)	12.4
Gangue	
Enstatite ($Mg_2Si_2O_6$)	33.9
Other	34.4

Table A 2: Base metal liberation in the Merensky concentrate sample.

Mineral	Pyrrhotite	Pentlandite	Chalcopyrite
Locked	5.4	3.6	8.5
MGM (Medium Grade Middling)	2.4	4.7	3.2
HGM (High Grade Middling)	11.5	6.8	7.3
Liberated	80.8	84.8	81.0
Total	100.0	100.0	100.0

Table A 3: Low temperature test conditions (test T9 to T19).
The tests were conducted in the rotating tube furnace in air.

Test ID	Temperature	Residence time	Gas flow rate [NL/min]
T9	400	15	42
T10	450	16	42
T11	400	5	42
T12	450	13.5	42
T13	450	10.5	42
T14	400	9.8	42
T15	400	6.5	42
T16	400	4	42
T17	400	3.5	28
T18	400	3.5	14
T19	350	2	42

Appendix B: Predominance diagrams inserts

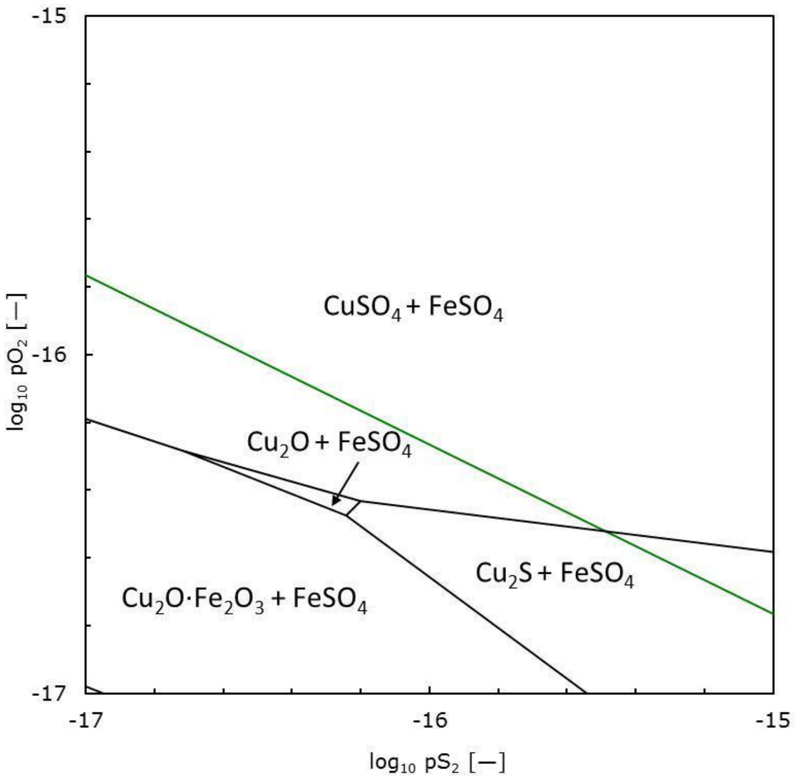

Figure B 1: Predominance diagram for Cu-Fe-S-O system at 400 °C, insert 1.

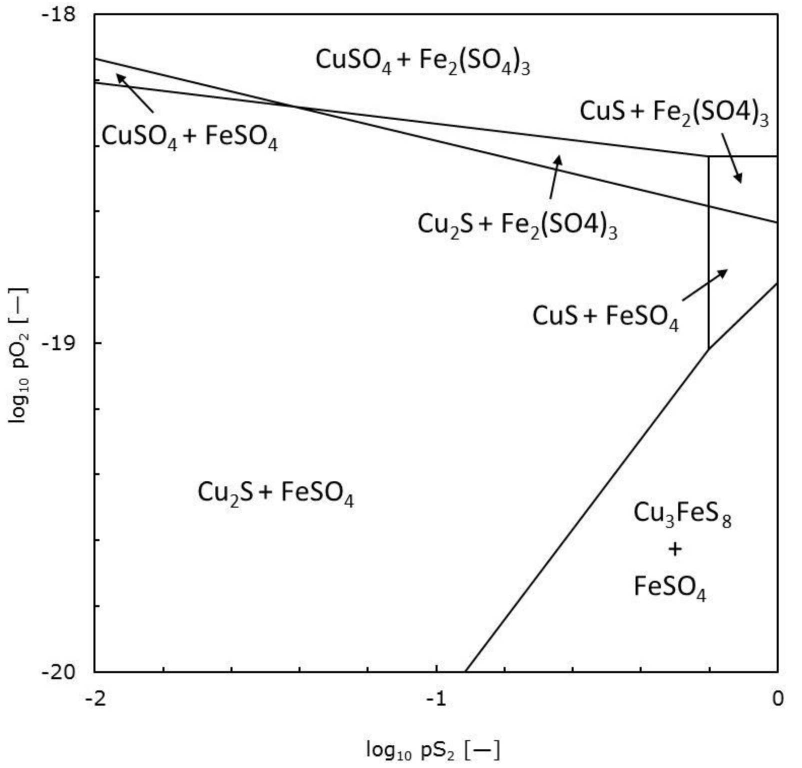

Figure B 2: Predominance diagram for Cu-Fe-S-O system at 400 °C, insert 2.

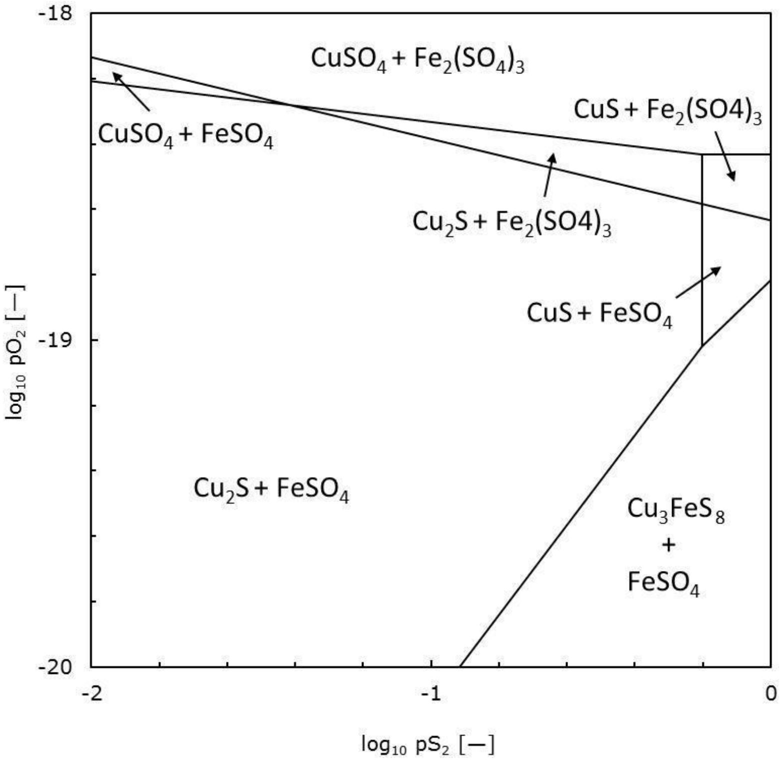

Figure B 3: Predominance diagram for Cu-Fe-S-O system at 400 °C, insert 3.

Appendix C: Binary phase diagrams

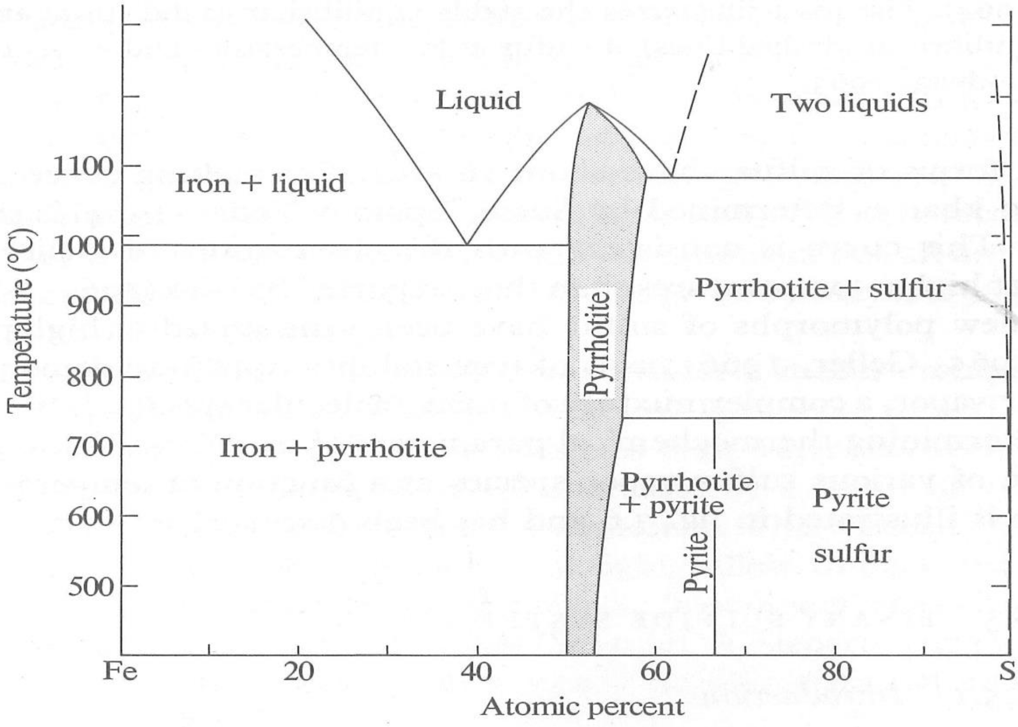

Figure C 1: Phase relations among condensed phases in the Fe–S systems above 400 °C. (after Kullerud & Yoder,1959, and Arnold, 1971)

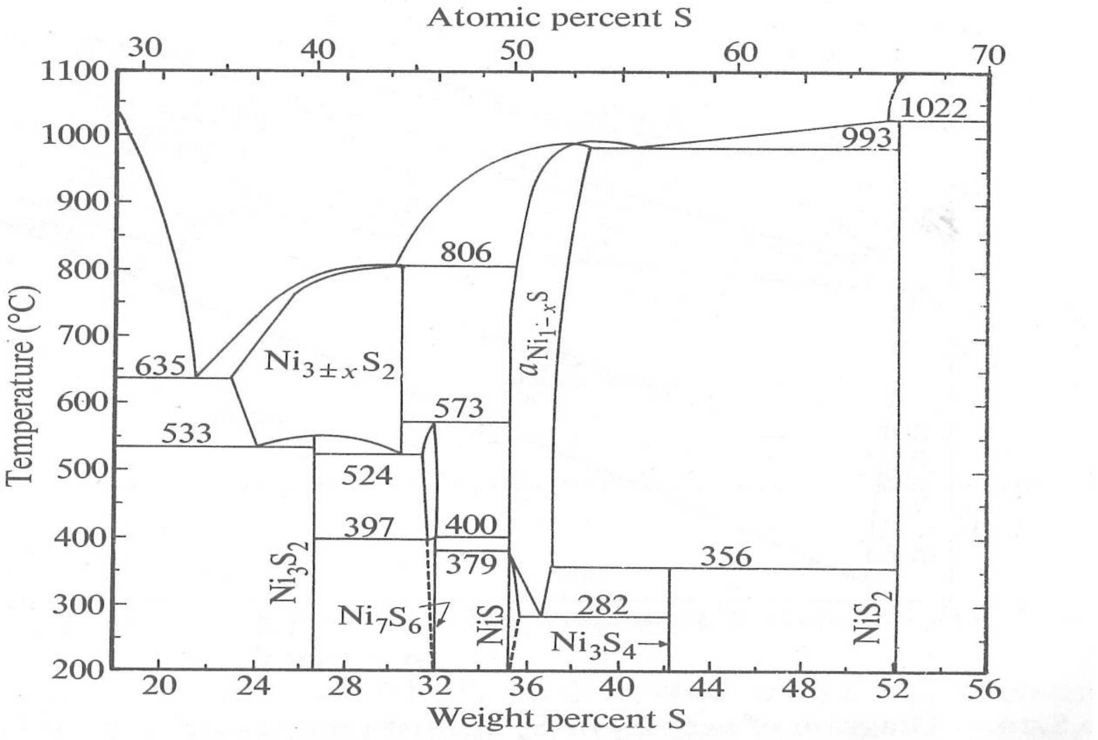

Figure C 2: Phase relations among condensed phases in the nickel–sulphur systems for 18 to 56 weight percent sulphur above 200 °C. (after Kullerud & Yund, 1962)

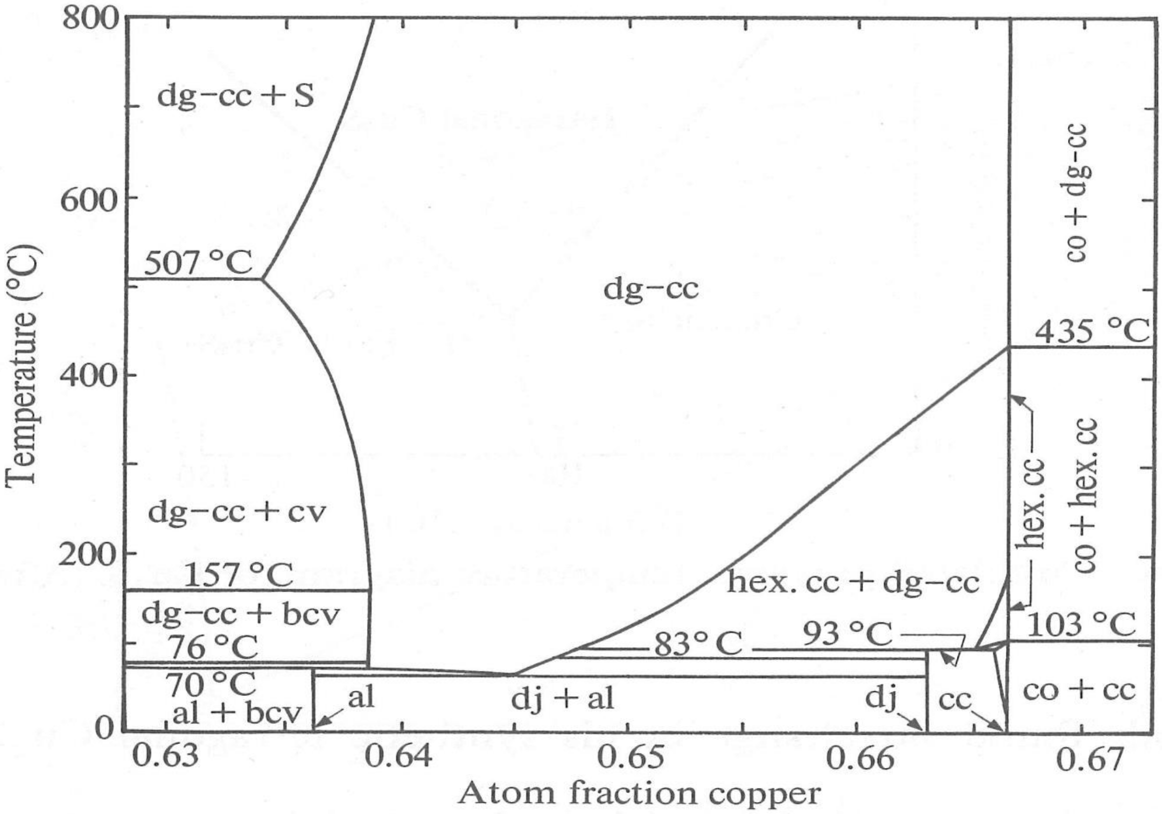

Figure C 3: Phase relations of condensed phases in the central portion of the copper–sulphur system, al, anilite; bcv, blue remaining-covellite; cc, chalcocite; cv, covellite; dg, digenite; dj, djurleite. (after Barton, 1973).

Appendix D: XRD analyses of all the concentrates roasted and unroasted.

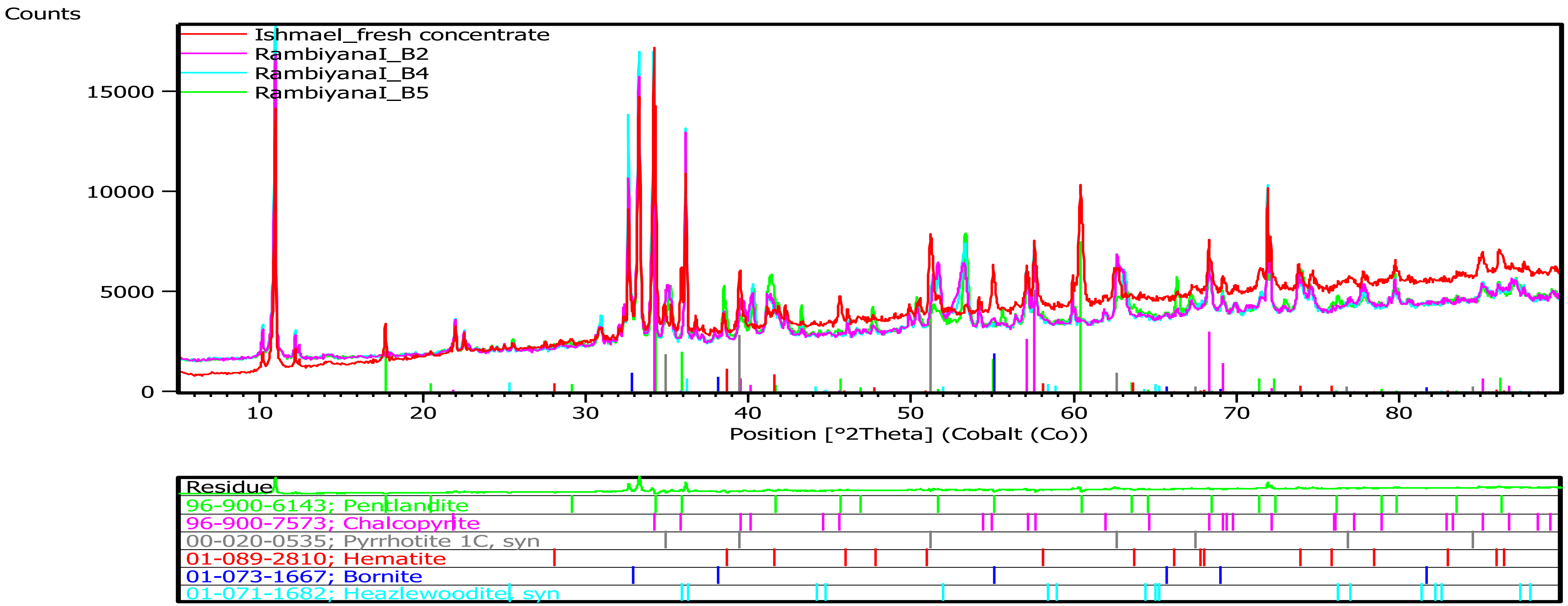

Figure D 1: XRD pattern of calcines for test run B2, B4 and B5
XRD micrographs (all the major peaks for the different phases in the samples shown). Tests were conducted in the capsule at 500 °C for 1hr . The gas conditions are in chapter 5.

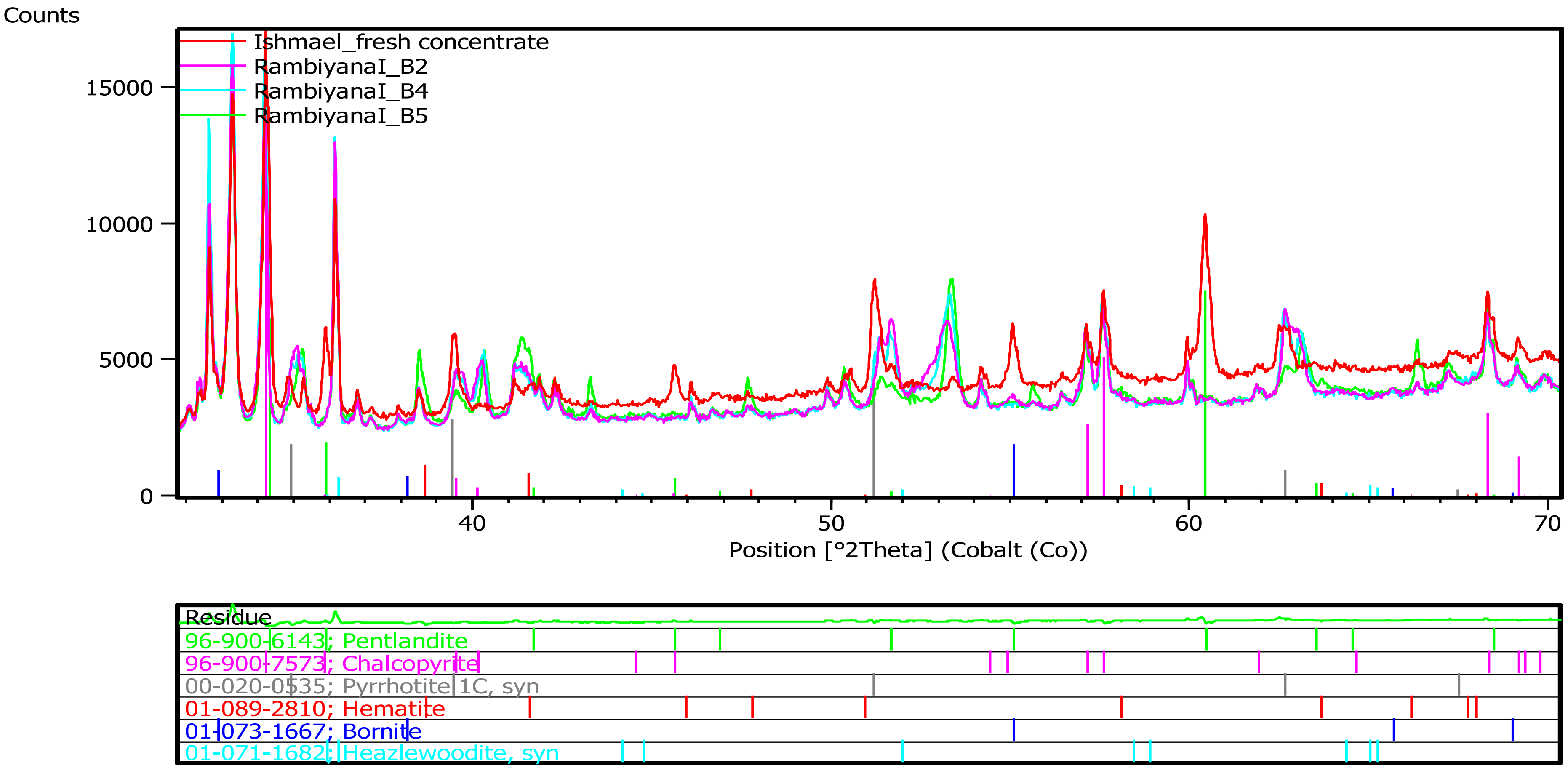

Figure D 2: XRD pattern of calcines for test run B2, B4 and B5
Higher Miller indices peaks are shown. Conducted in the capsule at 500 °C for 1hour.

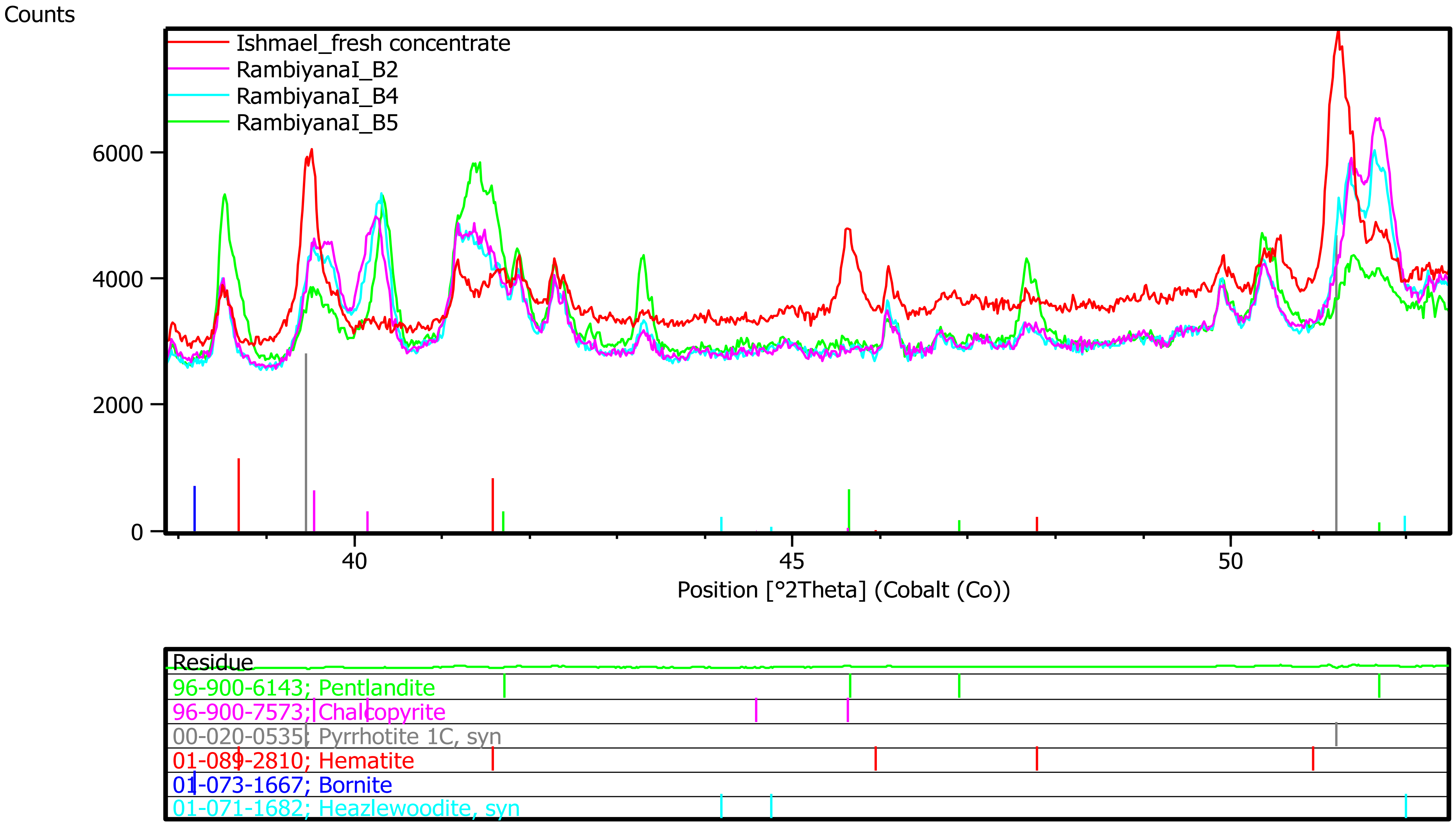

Figure D 3: XRD pattern of calcines for test run B2, B4 and B5
Emphasis on the pyrrhotite peaks. Conducted in the capsule at 500 °C for 1 hour. The gas conditions were given in Table 11.

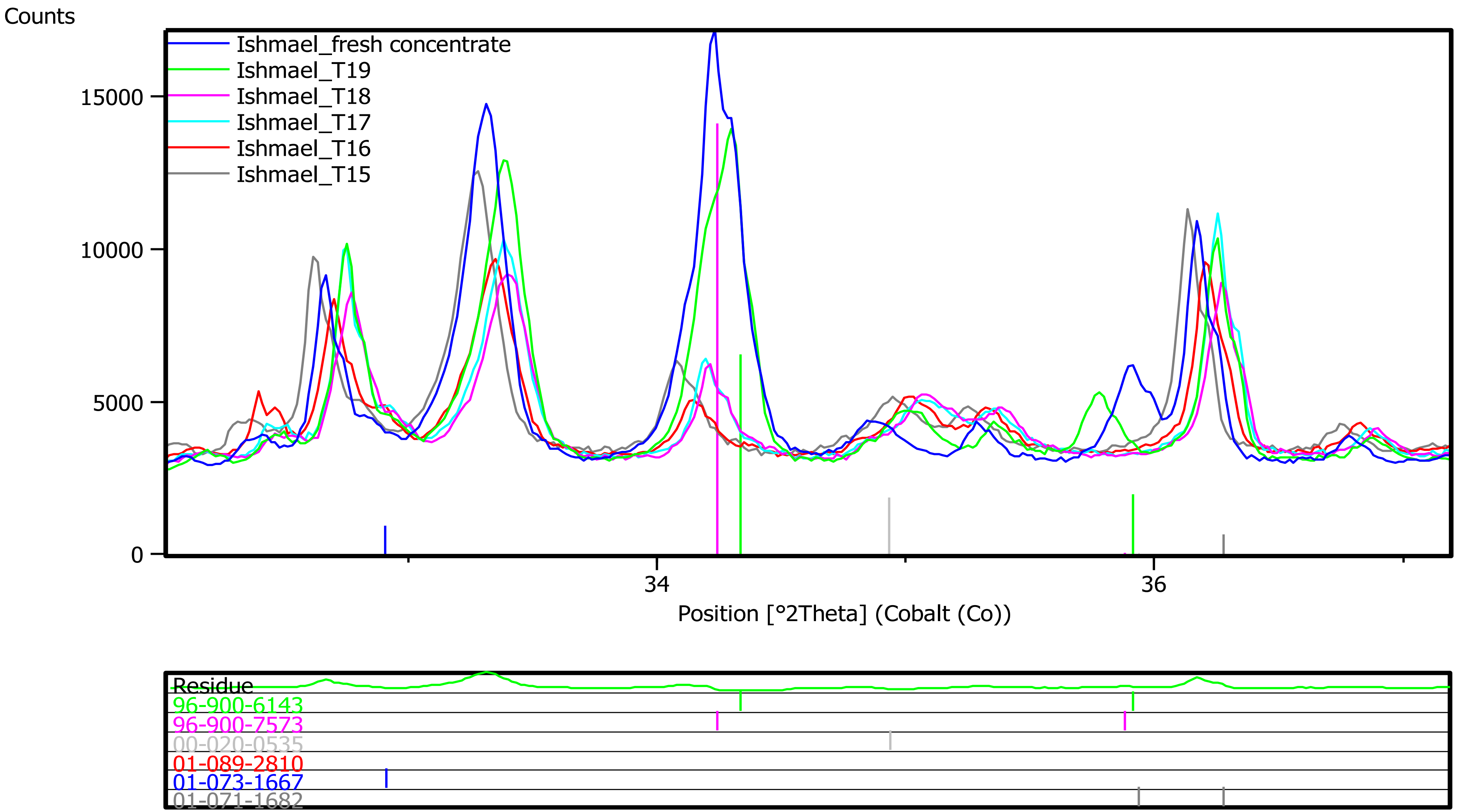

Figure D 4: XRD pattern of concentrate roasted in the RTF
The residue colour coding: lime – pentlandite, magenta – chalcopyrite, light grey – pyrrhotite, darker grey – heazlewoodite, red – hematite, blue – bornite.
Test conditions in Table A 3

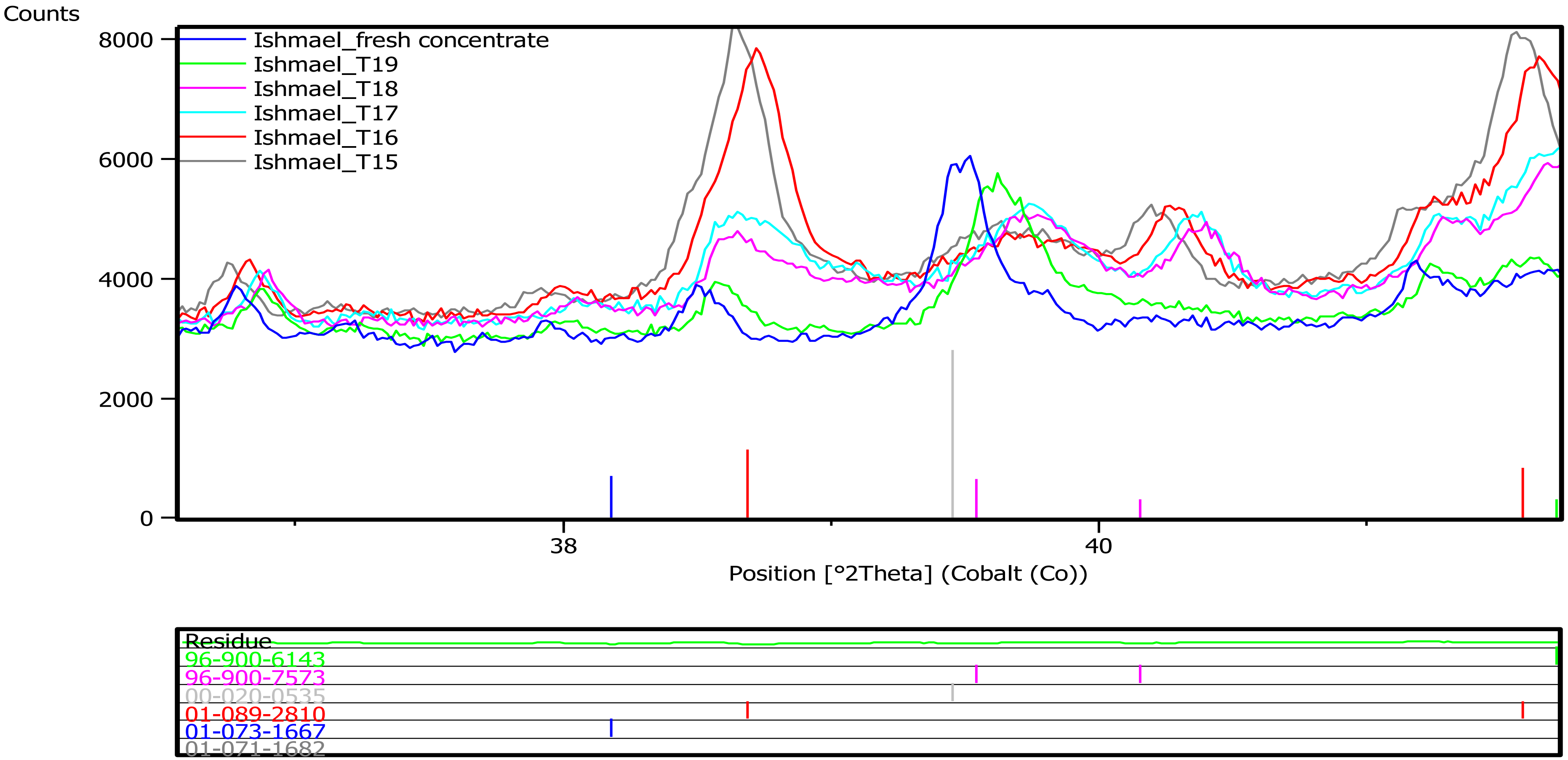

Figure D 5: XRD pattern of concentrate roasted in the RTF

The residue colour coding: lime—pentlandite, magenta—chalcopyrite, light grey—pyrrhotite, darker grey— heazlewoodite, red—hematite, blue—bornite. Test conditions in Table A 3

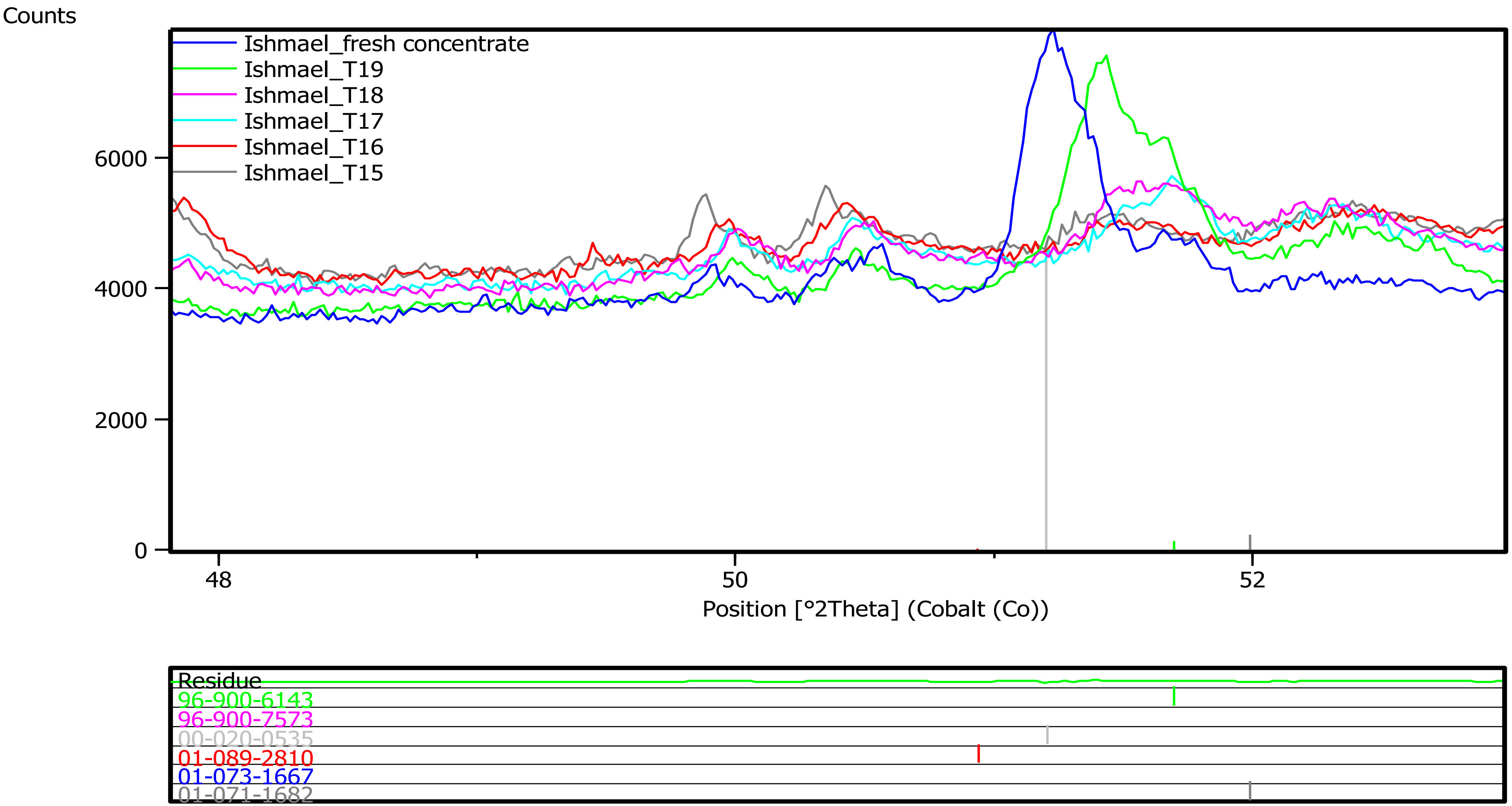

Figure D 6: XRD pattern of concentrate roasted in the RTF
The residue colour coding: lime – pentlandite, magenta – chalcopyrite, light grey – pyrrhotite, darker grey – heazlewoodite, red – hematite, blue – bornite.
Test conditions in Table A 3

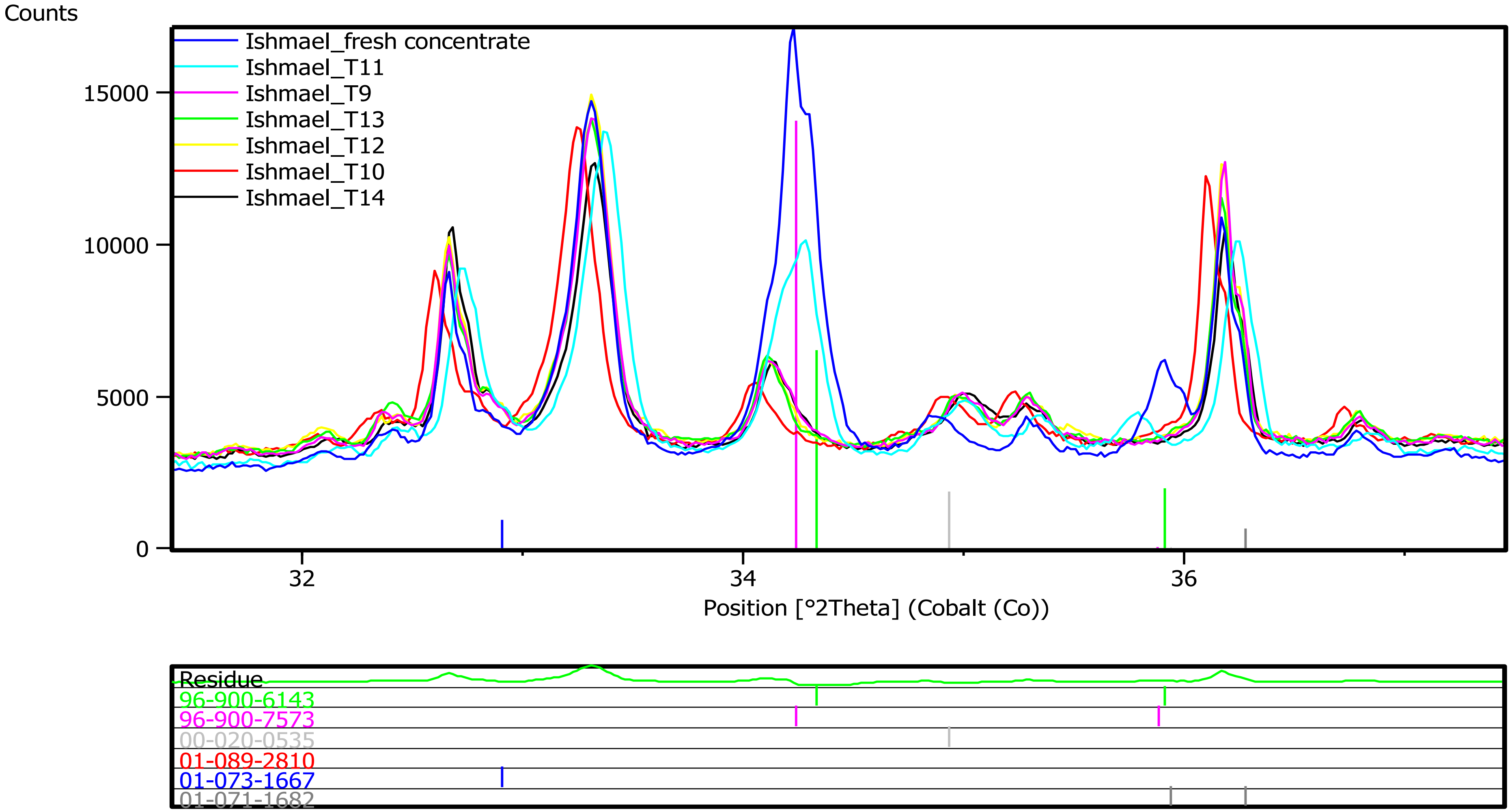

Figure D 7: XRD pattern of concentrate roasted in the RTF
The residue colour coding: lime – pentlandite, magenta – chalcopyrite, light grey – pyrrhotite, darker grey – heazlewoodite, red – hematite, blue – bornite. Test conditions in Table A 3

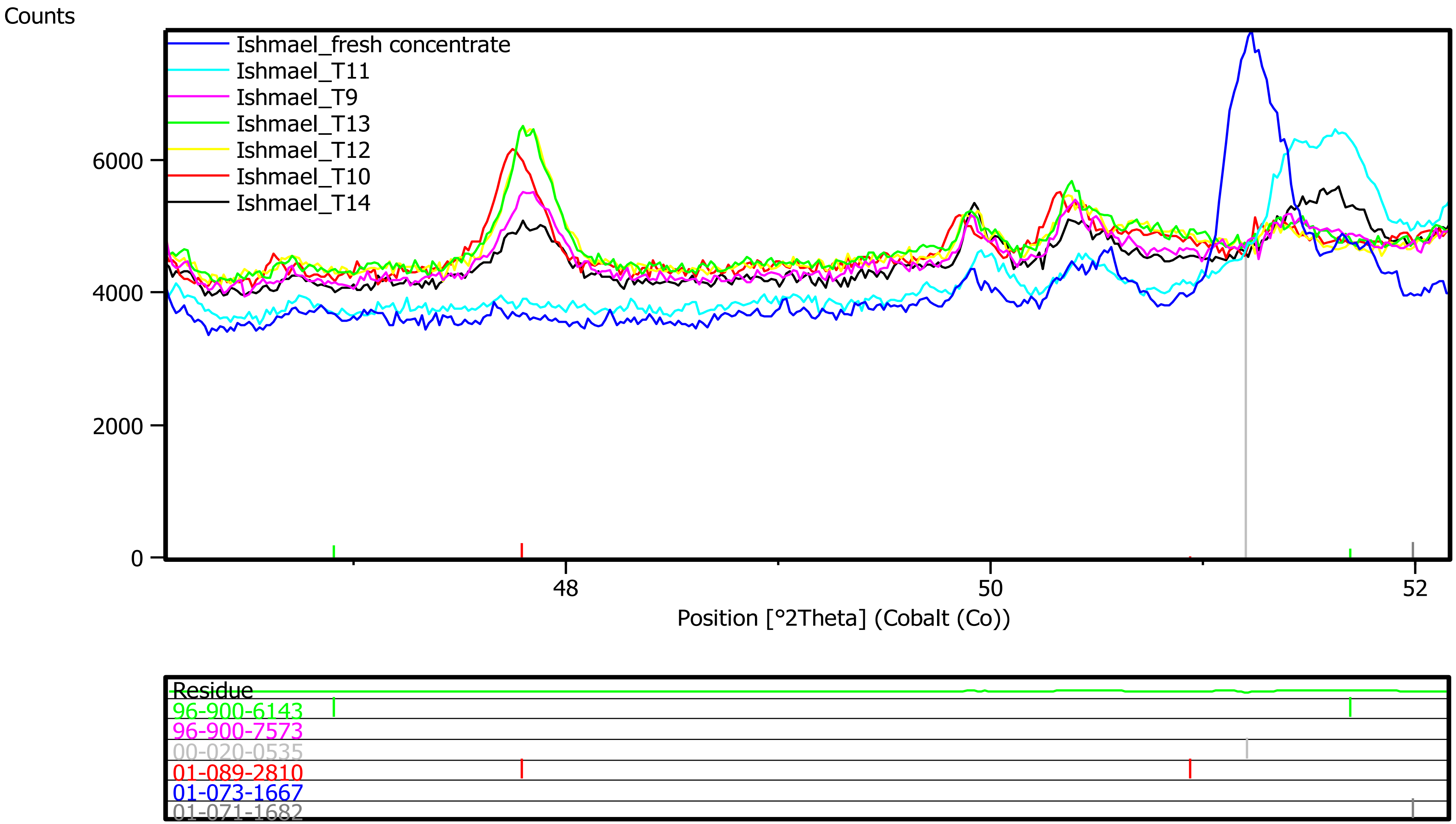

Figure D 8: XRD pattern of concentrate roasted in the RTF
The residue colour coding: lime – pentlandite, magenta – chalcopyrite, light grey – pyrrhotite, darker grey – heazlewoodite, red – hematite, blue – bornite. Test conditions in Table A 3

Appendix E: Magnetic signal

Magnetic signals given off by certain materials can be measured by instruments such as the Bartington MS2 and Satmagan. In samples where the type of magnetism (be it paramagnetic, ferromagnetic or diamagnetic) of certain minerals is known, these instruments can be a powerful tool to quantify the content of these mineral phases in a sample based on their magnetism.

The Satmagan measures the mass fraction of ferromagnetic material in a sample. Minerals and phases that are ferromagnetic include magnetite (Fe_3O_4) and metallic iron (which was not present in the examined samples). The sample can contain only one magnetic component, or have one component with dominant concentration and/or specific magnetic moment. The detection limit is typically 0.1 % on a weight basis (Rapiscan systems stagman 135 operating manual 9100 666-4VE REV 1.04).

The Bartington MS2 sensors operate on the principle of AC induction where power is supplied to the oscillator circuit within the sensor. A low intensity (approximately 80 A/m) alternating magnetic field is generated. Any material brought within the influence of this field will bring about a change in oscillator frequency. The frequency information is returned in pulse form to the MS2 indicator where it is converted into a value of magnetic susceptibility.

The sensors are insensitive to sample conductivity. The sensor subjects the sample to a non-saturating field that has the advantage of measuring initial susceptibility without destroying any sample magnetic remanence. All minerals and phases with a magnetic signal—ferromagnetic, paramagnetic, etc, produce a magnetic signal that will be picked up by the MS2.

Appendix F: Phase diagrams from Muan & Osborn (1964)

These systems are not ternary, the method of projection used in order to obtain this diagram is explained in the text in Muan and Osborn (1964).

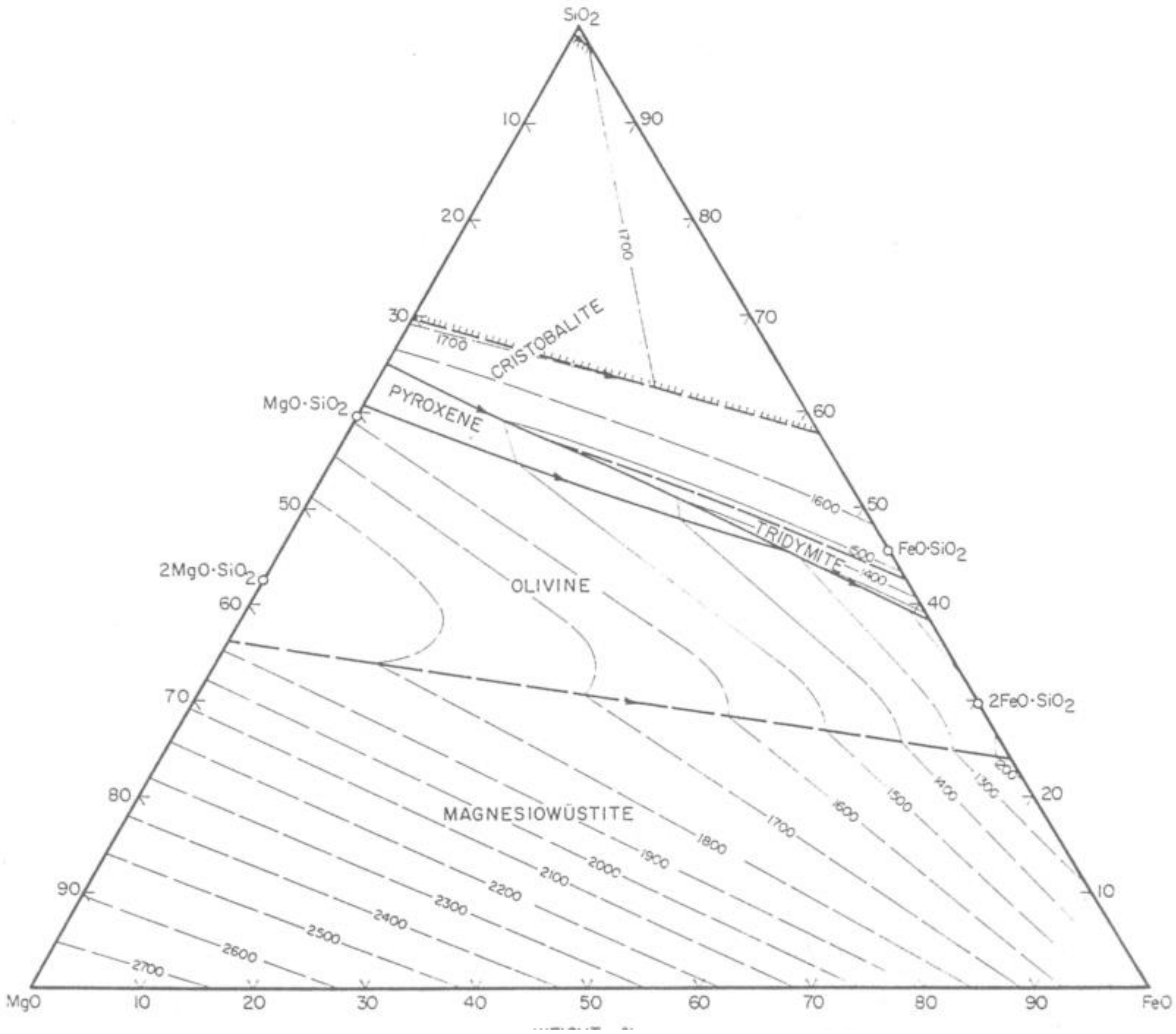

Figure F 1: The phase relations in the system MgO-iron oxide-SiO_2 in contact with metallic iron, after Bowen and Schairer.

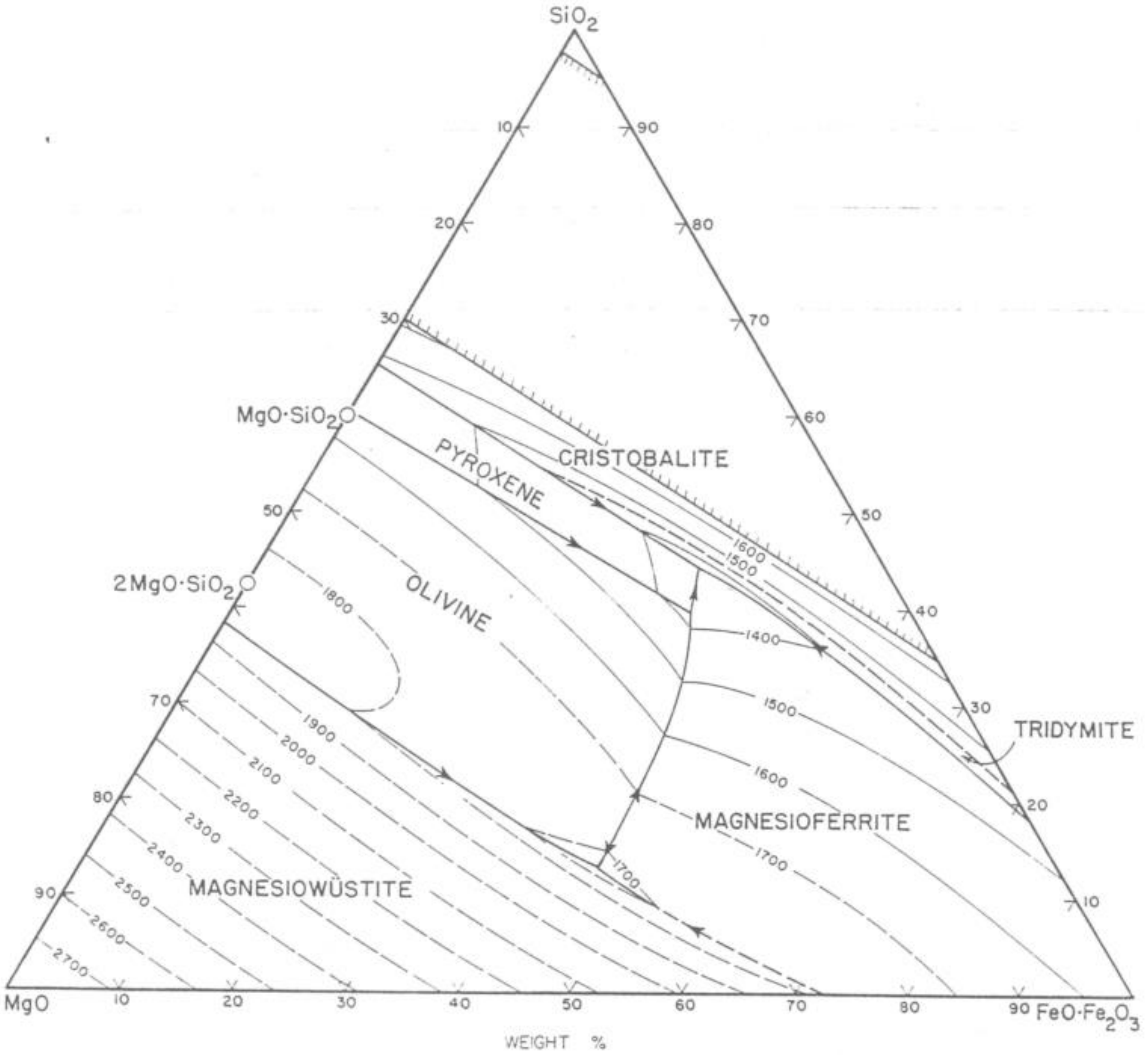

Figure F 2: The phase relations in the system MgO-iron oxide-SiO_2 in air, after Muan and Osborn.